MOLECULAR MODELING APPLIED TO CO_2-SOLUBLE MOLECULES AND CONFINED FLUIDS

by

Yang Wang

M.S. in Chemical Engineering,

East China University of Science and Technology, 2001

Submitted to the Graduate Faculty of
the School of Engineering in partial fulfillment
of the requirements for the degree of
Doctor of Philosophy

University of Pittsburgh
2006

UNIVERSITY OF PITTSBURGH
SCHOOL OF ENGINEERING

This dissertation was presented
by
Yang Wang
It was defended on
November 29, 2006
and approved by
J. Karl Johnson, Ph. D., Professor
Eric J. Beckman, Ph. D., Professor
Robert M. Enick, Ph. D., Professor
Kenneth D. Jordan, Ph. D., Professor
Dissertation Director: J. Karl Johnson, Ph. D., Professor

MOLECULAR MODELING APPLIED TO CO_2-SOLUBLE MOLECULES AND CONFINED FLUIDS

Yang Wang, Ph. D.

University of Pittsburgh, 2006

CO_2 is known to be an environmentally benign solvent. However, its feeble solvent power inhibits its wide use in industrial applications. The ultimate goal of this research is to design and optimize polymers that are highly soluble in CO_2. Molecular modeling methods have been used to analyze the results from experiments and make predictions. We have employed *ab initio* quantum mechanical methods to investigate interactions between CO_2 molecules and polymers. This is done by computing the interactions between CO_2 and polymer moieties and important functional groups. These functional groups include ether oxygens, carbonyl oxygens, and fluorines. We have identified several factors that believed to be responsible for CO_2-philicity. These factors include multiple site bindings, acidic hydrogens, and geometric considerations. We have designed three possible CO_2-soluble molecules based on our calculation results. Our experimental colleagues have synthesized and tested the corresponding polymers to compare with our predictions.

Single wall carbon nanotubes have attracted significant scientific interest as adsorption media since their discovery. Fluids confined in nanotubes have significantly different behavior from bulk fluids. We have performed simulations for alkanes adsorbed on the internal and external sites of carbon nanotubes. The simulation results qualitively match the experimental data from temperature programmed desorption. The diffusion coefficients in bulk and confined phases have been calculated. We have also studied the structure and infrared spectra of water adsorbed in nanotubes over a wide range of temperatures. Our simulation studies have identified the essential physics responsible for a distinctive infrared band observed in recent experiments.

TABLE OF CONTENTS

LIST OF TABLES

LIST OF FIGURES

PREFACE

I am very thankful to my advisor, Dr. J. Karl Johnson, for training, mentoring and providing opportunities to me during the past five years. His guidance, inspiration, encouragement, and wise and thoughtful discourses have laid the foundation for my Ph.D.. I am also grateful for his kind concern and help beyond my study. I learned a lot from both his academic excellence and character nobleness. I would also like to thank Dr. Beckman, Dr. Enick and Dr. Jordan for taking time out of their tight schedules to serve on my committee.

I would like to thank Lei Hong and Xin Fan for their experimental work on polymer phase behavior measurements in CO_2. I would also like to thank Oleg Byl and Petro Kondratyuk for their experimental work on carbon nanotubes. I also appreciate Jinchen Liu and Wai-Leung Yim for their simulation work and useful discussions.

1.0 INTRODUCTION

Molecular modeling can be broadly divied into two categories–quantum mechanical methods and statistical mechanical methods. *Ab initio* quantum mechanical methods do not depend on any empirical parameters. In principle, quantum mechanical methods can be used to compute geometries, electronic structure, vibrational spectra, and intermolecular interaction energies. However, the Schródinger equation cannot be solved exactly for any technically interesting system. Therefore, only approximate solutions can be obtained. High-accuracy quantum mechanical methods are computational expensive and the costs (memory and cpu time) grow very rapidly with increasing system size.

In contrast to quantum methods, statistical mechnics usually rely on empirical potentials to describe the interaction between atoms in a system. As a result, statistical mechanical methods can be used for simulations involving very large systems, containing thousands or even hundreds of milions of atoms. Theoretically, statistical mechanical simulations are able to calculate all the thermodynamic properties of a system. However, the accuracy of the results is limited by the accuracy of the interatomic potentials used in the simulation.

This work is divided into two parts, which mainly focuses on quantum mechanical methods and statistical mechanical methods, respectively. The first part of this work is devoted to molecular modeling of CO_2-polymer interactions. *Ab initio* quantum mechanical methods were used to characterize how CO_2 interacts with various polymer moities. However, quantum mechanics is incapable of describing liquid-gas and liquid-liquid phase transitions observed in CO_2-polymer systems. We therefore designed a new type of statistical mechanical simulation technique for describing fluid-fluid phase transitions. This new method, which we call the semi-grand ensemble, has been tested on a simple system of spherical molecules.

The second part of this work is devoted to molecular modeling of confined fluids in carbon nanotubes. Statistical mechanical methods were employed for this work. A simulation package, written in C++, was developed by the author for this phase of the work. The simulation package is capable of simulating dynamic properties in canonical, microcanonical, semi-grand, and grand canonical ensembles. The package can deal with complex molecules, such as linear and branched alkanes, as well as water.

1.1 CO_2-PHILIC POLYMERS

The application of carbon dioxide as a process solvent continues to elicit significant interest, as CO_2 generally poses fewer hazards than conventional organic solvents[1]. It is also inexpensive and an abundant material. The low critical temperature (31.17 °C) and moderate critical pressure (73.8 bar) are potential advantages for CO_2 since they are relatively easy to reach. At one time it was hoped that CO_2 could simply replace many organic solvents. However, subsequent work has found that CO_2 has rather feeble solvent power for polar and high-molecular weight materials. This means unrealistically high pressures are needed to dissolve compounds of interest.

During the 1990's, a number of "CO_2-philes" were discovered, which can efficiently transport insoluble or poorly soluble materials into CO_2 solvents, making a number of applications technically possible.[2, 3, 4, 5] However, most of these new CO_2 philes were fluoropolymers, which are very expensive. Although they were technically successful, their high cost renders the economics of a process unfavorable unless they can be recycled at greater than 99% efficiency. In addition, the recycle process is difficult and expensive. Furthermore, fluoroalkyl-functional materials persist in the environment. These drawbacks of fluoropolymers have greatly inhibited the commercialization of most new applications for CO_2, hence the full promise of CO_2-based technology has yet to be realized. Therefore, researchers have investigated the design of non-fluorous CO_2 philes. To date, a number of non-fluorous CO_2 philes, such as poly(propylene glycol), poly(vinyl acetate) (PVAc) and some other copolymers, have been found.[6, 7, 8] PVAc is the most CO_2 philic, non-fluorous vinyl polymer known to date. It can dissolve in CO_2 at pressures of ca. 430 bar at concentrations ranging from 1 to 5 wt% with number average molecular weight of 7,700 (89 repeat units).[9] However, the ideal CO_2-philie should exhibit miscibility in CO_2 under mild conditions (temperatures $T < 100\,^{\circ}\mathrm{C}$ and $P < 200$ bar). Hence, better non-fluorous CO_2 philes still need to be developed to render a variety of CO_2 processes both environmentally and economically responsible. Understanding of the solvent character of CO_2 molecules and their interactions with polymer molecules are helpful to design and optimize non-fluorous CO_2 philes, and thus further the commercialization of green processes employing CO_2 as the solvent. However, a complete knowledge of these problems has remained a challenge for researchers for more than two decades. The nature of the interaction of CO_2 with various polymers still needs close examination. A number of experimental and theoretical studies have been carried out to deal with the problem.

The ultimate objective of this research is to design and optimize non-fluorous CO_2-philic polymers. Investigating and understanding the mechanism of the solubility of various molecules in CO_2 will be greatly beneficial to the design and optimization of polymers. We have used *ab initio* quantum mechanical methods to study the interactions between CO_2 and several polymer segments. Some functional groups, such as carbonyl oxygens, ether oxygens, and fluorine atoms (for fluorocarbons), have been found to be favorable for CO_2 interactions through our calculations. We made predictions and designed serveral new polymers by applying the knowledge that we have gained from *ab initio* calculations.

1.2 CONFINED FLUIDS IN CARBON NANOTUBES

Single wall carbon nanotubes (SWNTs) have attracted significant scientific interest as adsorption media since their discovery. They are known to have high binding energy adsorption sites in the interior as well as in the grooves between adjacent nanotubes on the outside surface of SWNT bundles.[10, 11] The high binding energies on nanotubes, as compared to planar graphene sheets, stem from effective van der Waals interactions caused by the proximity of the curved nanotube walls in those adsorption sites.

Confined matter on the nanometer scale differs significantly from bulk matter.[12] The transport properties of adsorbed molecules play an important role in determining the applicability of carbon nanotubes as adsorbents, as they control the rates of molecular uptake and release. The smoothness of the nanotube surfaces give rise to the potential for rapid molecular transport. While nanotube confined simple fluids (sphere molecules) have been extensively studied, the studies on alkanes and water on carbon nanotubes are relatively limited.

We have studied the adsorption of alkanes on carbon nanotubes using statistical mechanical methods. The diffusion coefficients and molecule exchanging rates between nanotube internal and external sites have been measured. We have also computed the infrared spectra for water inside nanotubes. The results agree well with available experimental data.

2.0 MODELING OF CO_2-POLYMER INTERACTIONS

2.1 BACKGROUND

The content of this chapter is largely based on one of our publicatoins, "Effect of Grafted Lewis Base Groups on the Phase Behavior of Model Poly(dimethyl siloxanes) in CO_2".[13] The experimental work was done by Dr. Sevgi Kilic and Stephen Michalik. The author did all of the *ab initio* calculations.

There has been great interest in the application of carbon dioxide as solvent in industrial processes because CO_2 generally poses fewer hazards than conventional organic solvents.[1] CO_2 is also abundant, inexpensive, and has low critical temperature and moderate critical pressure. These are all potential advantages for CO_2 as a "green" solvent. However, the main drawback of CO_2 as a solvent is that it is a rather feeble solvent for polar and high-molecular weight materials.

2.1.1 Early studies on CO_2 as a solvent

Solubility parameter studies using equations of state suggest that CO_2 possesses the solvent power of short n-alkanes.[1] However, this concept has been proved to be wrong since experiments show many materials that are soluble in short alkanes, such as ethane and propane, are quite insoluble in CO_2 and vice versa.[14] This inconsistency revealed a gap between theoretical models and experimental data for CO_2 solubility. The large quadrupole moment has been suggested as being at least partially responsible for its weak solvent character.[15, 16] Johnston and colleagues suggested polarizability/free volume as a better method of evaluating solvent power,[17, 18] and by this method CO_2 is seen to be a very poor solvent when compared to short n-alkanes.

Experiments have also been carried out to investigate the solvent quality of CO_2.[19, 20] Phase behavior studies showed that CO_2 is a reasonably good solvent for aldehydes, ketones, esters, and low alcohols, but higher alcohols ($C > 10$), aromatic alcohols and polar compounds such as amides, ureas, and urethanes exhibit poor solubility in CO_2.[20] Heller et al. reported that the presence of amide, carbonate, ester, and hydroxyl groups in the polymer backbone imparts immiscibility to a polymer with CO_2, while ester and ether groups in the side chain do not have a detrimental effect on miscibility.[21]

2.1.2 Fluorinated polymers

Some fluorinated alkane, acrylate and ether polymers were found to be miscible with CO_2 at much lower pressures than their non-fluorous counterparts.[2, 22, 23] Both spectroscopic and theoretical studies have been used to study the CO_2-philic character of fluorinated polymers. Researchers have tried to determine whether any specific interactions exist between CO_2 and these molecules, and if so, what the nature of these interactions are and how it can be utilized to design new CO_2-philic materials.

Interestingly, both experimental and theoretical studies have resulted in contradictory findings. Yee et al. used FTIR to investigate the interactions between CO_2 and hexafluoroethane (C_2H_6).[24] They found no evidence of specific attractive interactions between the fluorine atoms and CO_2. In addition, CO_2 was found to be even more repulsive to C_2F_6 than C_2H_6. Therefore, they concluded that the highly repulsive nature of fluorocarbon-fluorocarbon interactions made the solute-solute interactions less favorable than solute-solvent interactions, and thus enhanced the CO_2 solubility of the fluorocarbons. On the contrary, using H and F NMR, Dardin et al. found no extraordinary solvent-solute interactions were present between C_6H_{14} and CO_2 whereas they observed a chemical shift in the C_6F_{14} spectra, which they ascribed to C_6F_{14}-CO_2 var der Waals interactions.[25]

As for theoretical studies, Cece et al. reported that there exist specific interactions between CO_2 and the fluorine atoms of C_2F_6, based on their *ab initio* calculations at restricted Hartree-Fock level.[26] However, the results were pointed out to be erroneous by Han et al., since basis set superposition error (BSSE) were not taken into account during calculations.[27] Using similar *ab initio* calculations, but accounting for BSSE corrections, Diep et al. reported no evidence of CO_2-F interactions in perfluorinated compounds that would explain the superior solubility of fluorocarbons versus hydrocarbons. Furthermore, interactions between hydrocarbons and CO_2 were found to be even stronger than those between fluorocarbon analogues and CO_2.[28] Raveendran and Wallen studied the effects of stepwise fluorination on the CO_2 interactions of methane. They found that fluorocarbon-CO_2 and hydrocarbon-CO_2 interactions are energetically comparable, through comparison of the calculated results for methane-CO_2 and perfluoromethane-CO_2 systems. They also pointed out the different nature of CO_2 interacting with fluorocarbons and hydrocarbons. Fluorine atoms in fluorocarbon can act as Lewis bases towards electron deficient carbon atom of CO_2, and the hydrogen atoms, having increased positive charge due to the neighboring fluorine, act as Lewis acids towards the electron rich oxygen atoms of CO_2.[29] They also claimed that there is an optimal density of fluorine atoms leading to maximum CO_2 philicity. Fried and Hu investigated the interactions of CO_2 with three alkanes (CH_4, CH_3CH_3, $CH_3CH_2CH_3$) and fluoroalkanes (CF_4, CF_3CH_3, $CF_3CH_2CH_3$). They concluded that quadrupole-dipole interactions contributed an important part to the total interaction energies.[30]

2.1.3 Non-fluorinated polymer: several important functional groups

Most fluoropolymers are very expensive and are therefore are economically unfavorable. Furthermore, fluorine-containing molecules are environmentally suspect. For example, perfluorooctanoic acid (PFOA) has recently been targeted by the EPA for reduction because PFOA is very persistent in the environment and is a suspected carcinogen.[31] Recent research has focused on the design of non-fluorous CO_2-philes, specifically hydrocarbon-based and oxygenated-hydrocarbon-based polymers, in order to avoid the cost and environmental concerns of fluorous materials.[8, 6, 7]

FT-IR have been used for investigation of CO_2 interacting with specific functional groups. Kazarian et al. reported the existence of specific interactions between the carbon atom of

CO_2 and lone pairs on the oxygen of a carbonyl. They argued that this complex formation is most probably of a Lewis acid-Lewis base nature.[32] This specific interaction has also been studied by other researchers,[33, 34, 35, 13, 36] and been utilized to design new CO_2-philic materials. [6, 7] Using *ab initio* calculations, Nelson and Borkman investigate the splitting of the ν_2 mode of CO_2 while interacting with carbonyl groups in simple molecules.[33] Later, Raveendran and Wallen supplemented that $\mathrm{C{-}H \cdots O}$ hydrogen bonds, significant type of interactions, were identified by closer examination of Nelson and Borkman's results. They also reported the presence of attractive specific interactions between CO_2 and the S=O group in dimethylsulfoxide. The effects of the sulfonyl group on CO_2 solubilities has not yet been probed by experiments.[34]

2.1.4 Theoretical studies

There have been a number of different efforts to model the thermodynamic properties of polymer-CO_2 mixtures. Generally speaking, these modeling techniques fall into three categories: equation of state modeling,[37, 38, 39] statistical mechanical simulations,[40] and *ab initio* calculations.[28, 29, 34, 35] Equation of state methods have not proved to be accurate enough to predict the phase behavior of polymer-CO_2 mixtures.[38] In principle, one could compute virtually all the thermodynamic properties of polymer-CO_2 mixtures through statistical mechanical simulations. However, this requires very accurate molecular interaction models, which are currently not available, especially for the polymer-CO_2 cross-interactions. Another alternative is to bypass the use of potential models and directly use *ab initio* methods to generate the forces required for a simulation, such as is done in Quantum Molecular Dynamics.[41, 42, 43] However, this is impractical for polymer-CO_2 mixtures due to the large system sizes and weak interactions among the molecules. Ab initio methods cannot be directly applied to true polymer systems because of the large number of atoms and the aperiodic nature of the polymer. Therefore, polymer segments or some specific functional groups are used to perform *ab initio* calculations.

2.2 THEORY

The cloud point behavior of polymers in near-critical CO_2 depends on the total thermodynamics of these complex systems. In principle, molecular modeling can be used to compute essentially all the thermodynamic properties of the polymer-CO_2 mixtures through statistical mechanical simulations. In practice, however, accurate thermodynamic properties depend critically on the accuracy of the molecular interaction models that must be used in the statistical mechanical simulations. At present, intermolecular potential models are not accurate enough to allow high precision calculation of thermodynamic properties of polymer-CO_2 mixtures from statistical mechanics. An alternative is to use *ab initio* quantum mechanical methods to compute the zero-temperature interaction energies between CO_2 and functional moieties of the polymers of interest. This approach has the advantage of giving (in principle) highly accurate interaction energies for CO_2 and the functional groups of the polymers. Two obvious disadvantages are that the entire polymer cannot be modeled and that no finite temperature properties are calculable.

2.2.1 The choice for level of theories

The interaction energies of polymer-CO_2 systems are very weak (compared with molecular bonds) and are dominated by electron correlation effects (van der Waals interactions). These weak interactions are difficult to compute from *ab initio* methods. This is because high level methods and large basis sets are needed to capture electron dispersion. Computationally efficient methods, such as density functional theory, or even gradient-corrected density functional methods, are known to be generally inadequate for computing van der Waals interactions.[44, 45, 46, 47, 48, 49, 50, 51] Methods that include triple excitations, e.g., MP4(SDTQ), coupled cluster with perturbational triples, CCSD(T) are required for many applications.[52, 53, 54] The CCSD(T) theory is considered to be highly accurate for computing weak interactions, but because of the high computational demands and unfavorable scaling with the number of basis functions, it cannot be used for most of the systems of interest. The Møller-Plesset (MP) perturbation method including electron correlation has been used for weakly interacting systems, but is known to have convergence problems.[52, 53, 55] MP2 is not generally adequate for computing intermolecular interaction energies, except when a substantial electrostatic interaction is involved.[56, 57] However, recent work indicates that failure of MP2 may in part be due to basis set superposition error (BSSE).[55, 58] To compute accurate energies, one must correct for BSSE. We have applied counterpoise (CP) corrections[59] to all interaction energies to approximately account for BSSE.

We have used MP2 to estimated the interaction energies and geometries of methyl acetate (MA) with a single CO_2 molecule. The interaction energy is defined as

$$E_b = E_{tot} - \sum E_i \tag{2.1}$$

where E_{tot} is the total energy of the dimer (polymer segment/CO_2) and E_i is the relaxed gas-phase energy of each of the constituent molecules in the dimer. Three distinct binding modes have been identified for the MA-CO_2 dimer, shown in Figure 1.

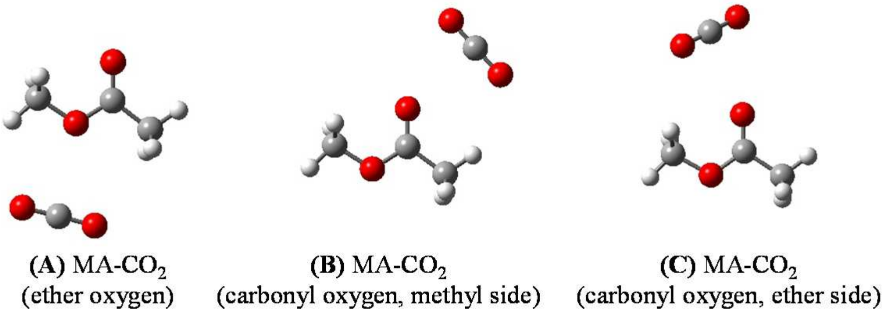

Figure 1: Three distinct binding modes for MA-CO_2 dimer. (A) CO_2 mainly binds with the ether oxygen; (B) CO_2 mainly binds with the carbonyl oxygen, tilting towards the methyl group side; (C) CO_2 mainly binds with the carbonyl oxygen, titling towards the ether group side.

We have tested the convergence of the interaction energy with respect to the level of theory, using binding mode (B) of the MA-CO_2 dimer. The results are shown in Figure 2. We plot both the raw and the counterpoise (CP) corrected[59] interaction energies. The CP correction approximately accounts for BSSE, but it often over estimates the actual correction,

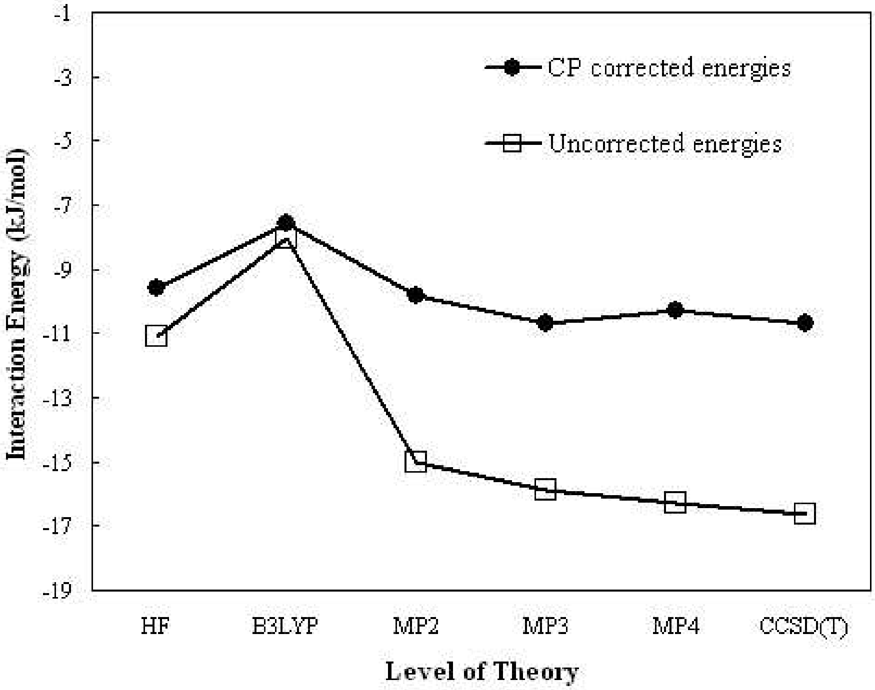

Figure 2: Convergence of the interaction energy of MA-CO_2 with the level of theory. The basis set used is 6-31+G(d). The MP2 energy is within 10% of the CCSD(T) energy for both uncorrected and CP corrected energies. The geometry of the dimer was optimized at MP2/6-31+G(d) with CP corrections.

as we will discuss shortly. The basis set used for these calculations was 6-31+G(d). Use of this rather small basis set made the CCSD(T) calculations tractable, and the geometries of the dimer and monomers were optimized at the MP2/6-31+G(d) level of theory, including CP corrections in the optimization. All of the calculations were performed with the Gaussian 98 package. [60] Our calculations indicate that the MP2 potential energies are within about 0.8-1.7 kJ/mol of the CCSD(T) values. This is in contrast to the B3LYP density functional calculations, which are 2.5 (CP corrected) to 8.4 (uncorrected) kJ/mol less than the CCSD(T) values. Thus, we conclude that MP2 binding energies provide a reasonable approximation to the full CCSD(T) binding energies. In addition, we are interested in relative interaction energies for CO_2 with polymer moieties; relative energies are expected to be more accurate than absolute energies. Therefore, we chose Møller-Plesset second order perturbation theory (MP2) to perform calculations as a compromise between accuracy and efficiency.

2.2.2 The effects of basis sets

In order to check the convergence of the energy with respect to the basis set we extrapolated the interaction energies to the complete basis set (CBS) limit using the expression of Helgaker et al.[61] with augmented correlation-consistent basis sets. We have used the aug-cc-pVDZ and aug-cc-pVTZ basis sets in the expression,

$$E_n = E_\infty + a n^{-3} \tag{2.2}$$

where E_n is the interaction energy calculated from the aug-cc-pVnZ basis set, E_∞ is the CBS limit energy, and a is an adjustable parameter. We found that the averages of the raw and CP corrected energies are very close to the CBS limit values, in agreement with the findings of Feller and Jordan.[62] From Figure 3, we can clearly see that the CBS extrapolation values for the systems of interest can be estimated from the average of the raw and CP corrected energies with the aug-cc-pVDZ basis set. This approximation will give an error in the energies of about 0.4 to 0.8 kJ/mol. Combining the errors due to the basis set and level of theory (MP2 vs. CCSD(T)), we estimate that the interaction energies reported here

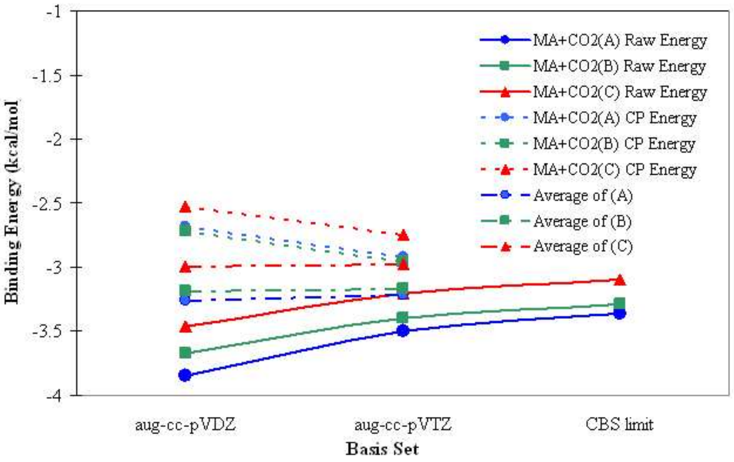

Figure 3: Phase behavious of poly(vinyl acetate) and poly(methyl acrylate) in CO_2

are within about 1.3 to 2.5 kJ/mol of the CCSD(T)/CBS limit. For the MA-CO_2 system the numbers of basis functions are 164, 238, and 506 for the 6-31+G(d), aug-cc-pVDZ, and aug-cc-pVTZ basis sets, respectively. The aug-cc-pVTZ basis set is too large for tractable calculations on systems with a larger number of atoms. Hence, we only report the averages of MP2/aug-cc-pVDZ CP corrected and uncorrected interaction energies systems larger than MA-CO_2.

2.2.3 Calculation procedures

We carried out geometry optimizations at the MP2/6-31+G(d) level of theory and basis set. The 6-31+G(d) basis set was chosen as a compromise between completeness and efficiency. Optimizations were started from several different initial configurations, in which CO_2 molecules were placed around oxygens of the polymer moieties. We performed single point energy calculations on geometries obtained from optimizations using a much larger basis set (aug-cc-pVDZ). CP corrections were applied to all binding energies to approximately account for BSSE. As mentioned before, we only report the average of raw and CP corrected energies as an approximation for energies at the CBS limit. We have computed localized charge distributions for several of the model polymer segments using the natural bonding orbital (NBO) method. Gaussian 98[60], revision A11 and Gaussian 03[63] were used for all of the calculations.

3.0 CO_2 SOLUBILITY OF OXYGENATED-HYDROCARBONS: TWO INTERESTING ISOMERS

3.1 COMPUTATIONAL DETAILS

The material of this chapter is largely based on one of our publications, “Effect of Grafted Lewis Base Groups on the Phase Behavior of Model Poly(dimethyl siloxanes) in CO_2”.[13]. The experimental work was done by Sevgi Kilic and Steve Michalik from Professor Robert M. Enick’s research group in University of Pittsburgh. The author did all the *ab initio* calculations.

Rindfleisch et al.[8], as well as Enick and colleagues,[9] noted that the cloud point pressures of poly(vinyl acetate) and poly(methyl acrylate) in CO_2 differ by hundreds to thousands atmospheres (Figure 4), despite the fact that these polymers are isomers. Topology clearly plays a role in determining the phase boundary of a material mixed with CO_2.

As we have mentioned before, the entire polymers cannot be used directly in the *ab initio* calcualtions due to their large sizes. Therefore, we have chosen model molecules for PVAc and PMA to perform the calculations. The model molecules are isopropyl acetate (IPA) and methyl isobutyrate (MIB) for PVAc and PMA, respectively. The model molecules were selected to mimic the repeat units of each polymer. The structures of the two model molecules are shown in Figure 5.

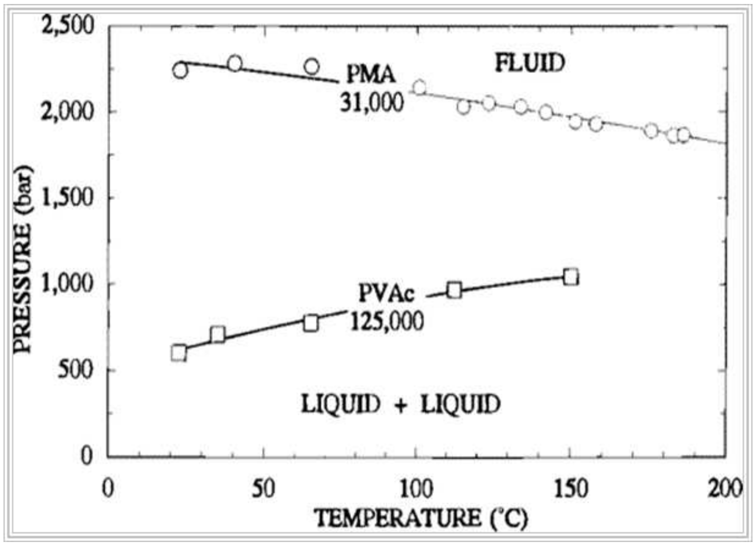

Figure 4: Phase behavior of poly(vinyl acetate) and poly(methyl acrylate) in CO_2

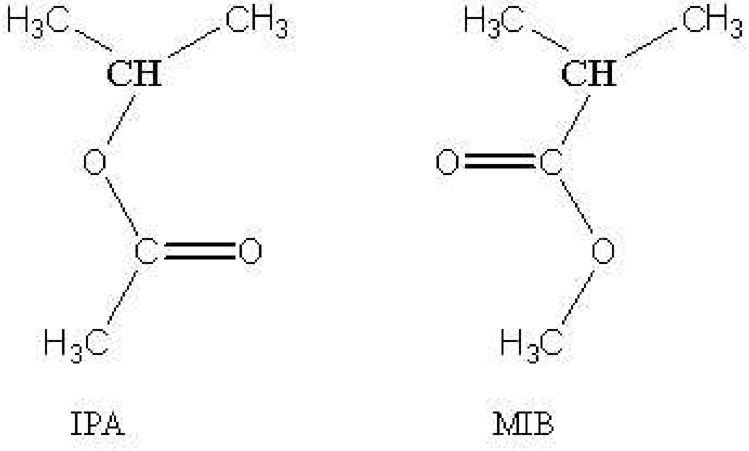

Figure 5: Molecular structures of isopropyl acetate (IPA) and methyl isobutyrate (MIB)

3.2 RESULTS AND DISCUSSIONS

We have identified three binding modes for both the IPA-CO_2 dimer and MIB-CO_2 dimer. The binding modes are similar to what we achieved for MA-CO_2 dimer (Figure 1), which are CO_2 binds with the ether oxygen (A), CO_2 binds with the carbonyl oxygen from the methyl group side (B), and CO_2 binds with the carbonyl oxygen from the ether group side (C) (Figure 6 and Figure 7).

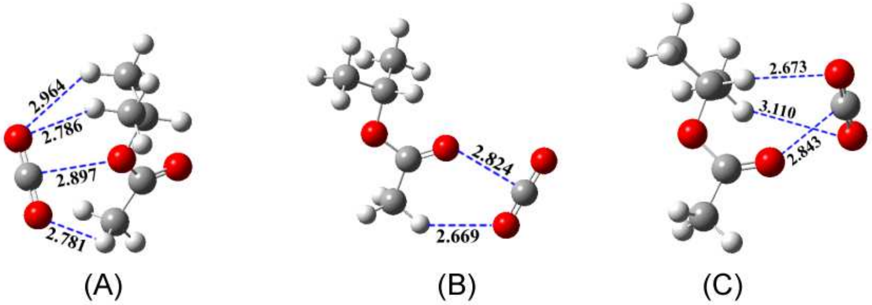

Figure 6: Three binding modes of isopropyl acetate-CO_2 complex. (A) CO_2 binds with ether oxygen; (B) CO_2 binds with carbonyl oxygen from the methyl group side; (C) CO_2 binds with the carbonyl oxygen from the ether group side.

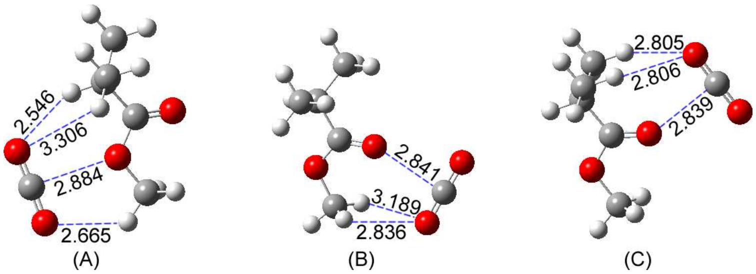

Figure 7: Three binding modes of methyl isobutyrate-CO_2 complex. (A) CO_2 binds with ether oxygen; (B) CO_2 binds with carbonyl oxygen from the methyl group side; (C) CO_2 binds with the carbonyl oxygen from the ether group side.

The interaction energies are listed in Table 1. The data in Table 1 indicate that the differences in energies between the different sites are fairly small. The interaction of MIB-

Table 1: Interaction Energies for CO_2 Binding with IPA and MIB molecules[a]

	Δ E[b] (kJ/mol)	
Binding modes	IPA-CO_2	MIB-CO_2
(A)	-14.7	-15.6
(B)	-14.2	-14.5
(C)	-15.9	-13.6

[a]The (A), (B), and (C) labels denote configurations with CO_2 interacting with ether oxygens, carbonyl oxygens with CO_2 tilted toward the methyl group, and carbonyl oxygens with CO_2 tilted toward the ether oxygen, respectively. All geometries were optimized at the MP2/6-31+G(d) level of theory. [b]Single point energies calculated at MP2/aug-cc-pVDZ

CO_2 (C) is somewhat weaker than others. In addition, the binding of CO_2 to the ether oxygen in IPA (IPA-CO_2 (A)) does appear to be slightly weaker than with the carbonyl oxygen. However, the difference is smaller than the expected accuracy of the calculations. The average interaction energy for the IPA-CO_2 system and MIB-CO_2 system are -14.9 and 14.6 kJ/mol. These two very close interaction energies indicate that the CO_2-philicities of the two molecules are comparable. Experiments have also been done for the two molecules to explore their phase behavior in CO_2. The results are shown in Figure 8. As we can see from Figure 8, the two lines largely overlap, which means that the two compound have nearly the same CO_2-solublity. This is consistent with our calculation findings. Based on calculated interaction energies, we aslo expect that the ether oxygens are just as important as carbonyl oxygens in facilitating CO_2 solubility of these polymers, since the interactions energies for CO_2 binding with ether oxygens and carbonyl oxygens are comparable. We will discuss the ether oxygens in more detailes in later section. From our calculation results, however, we cannot find the origin of the remarkable difference in CO_2 solubility for the two polymers. Statistical simulations are needed to further investigate the polymers.

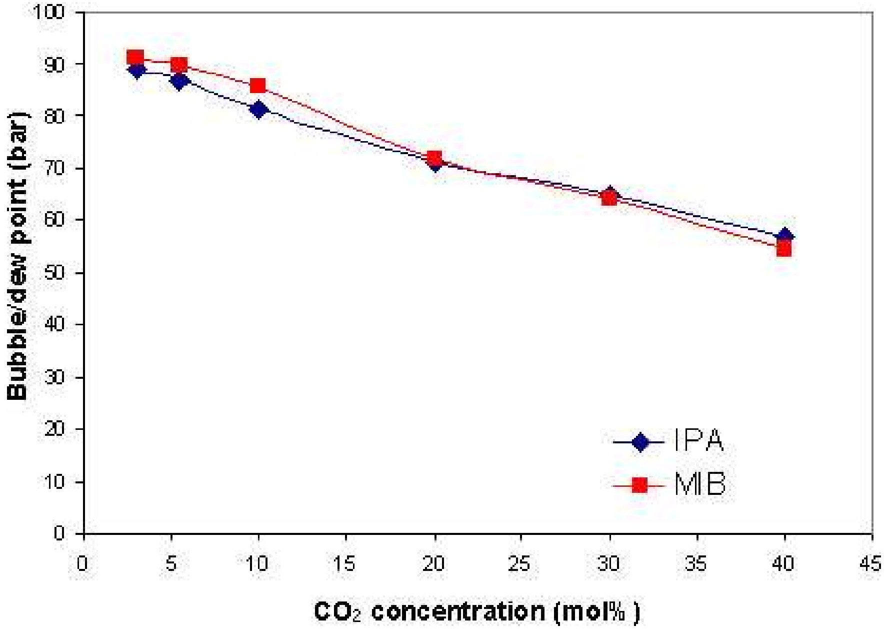

Figure 8: Phase behaviors of isopropyl acetate and methyl isobutyrate in CO_2, T = 323 K

4.0 WHY ARE FLUORINATED POLYMERS CO_2SOLUBE

4.1 INTRODUCTION

The content of this chapter is adopted form one of our publications, "Synthesis and Solubility of Linear Poly(tetrafluoroethylene-co-vinyl acetate) in Dense CO_2: Experimental and Molecular Modeling Results".[64] The experimental work was done by Bilal Baradie, Molly S. Shoichet, Zhihua Shen, and Lei Hong. The author did all of the *ab initio* calculations.

Experiments have shown that the co-polymer of tetrafluoroethylene (TFE) and vinyl acetate (VAc), poly(TFE-co-VAc), is very CO_2-soluble. It is more CO_2 soluble than either of its homopolymers, shown in Figure 9. Note that the homopolymer of TFE is insoluble in CO_2 under experimental conditions.

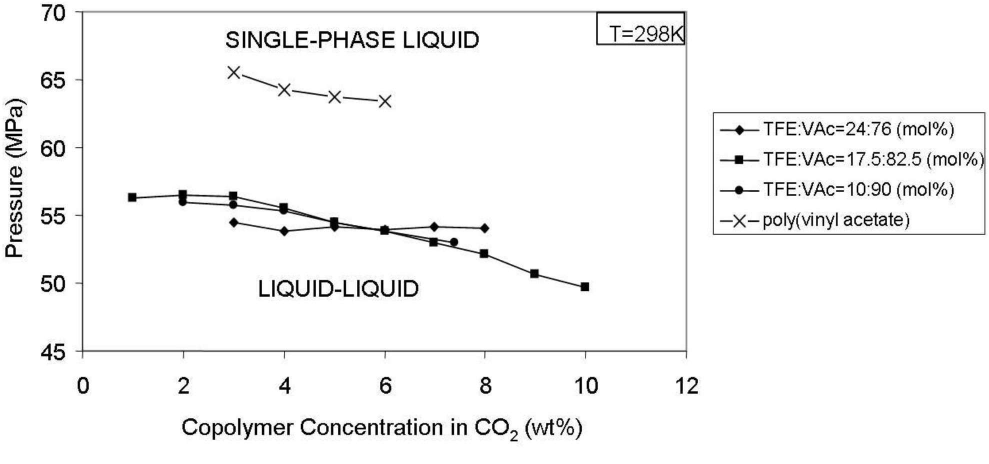

Figure 9: Pressure-composition phase diagram for TFE-VAc copolymer system at 25 °C

The optimal range for the TFE composition in the co-polymer is from 11.6 to 26.5%. Interestingly, high fraction of TFE in the co-polymer reduces its CO_2 solubility. The precise reasons for the enhanced solubility of partially fluorinated polymers over their hydrocarbon analogues are not entirely understood.

We have employed *ab initio* molecular modeling to identify reasons for the enhanced solubility of poly(TFE-co-VAc) relative to the PVAc homopolymer. Figure 10a illustrates that the fluorinated carbons in the copolymer backbone will be adjacent to either a methylene carbon or a methane carbon from which the pendant -$OCOCH_3$ group extends. We take one representative portion of poly(TFE-co-VAc) with a relatively small concentration of TFE shown in Figure 10b and divide it into three small molecules, shown in Figure 10c, that are conducive to molecular modeling calculations. Firstly, we cut the molecule between the two CF_2 functional groups, yielding two fluorous molecules, 3,3,3 tri-fluoro isopropyl acetate (TFIPA), and 4,4,4 tri-fluoro-sec-butyl acetate (TFSBA). The third small molecule is 2,2,3,3-tetrafluorinated butane (FB), which is a model for the backbone of the polymer. The hydrocarbon analogs of these small molecules, shown in Figure 10d, are isopropyl acetate (IPA), sec-butyl acetate (SBA) and n-butane. These molecules are used for direct comparisons with the semi-fluorinated compounds.

We have identified four possible binding configurations for CO_2 interacting with TFIPA and TFSBA. We use the TFIPA molecule as an example to illustrate the possible binding configurations because TFSBA has similar CO_2 binding configurations. The specific binding configurations are illustrated in Figure 11 as: (A) ether oxygen, (B) carbonyl oxygen, tilted towards the methyl group, (C) carbonyl oxygen, tilted towards the ether group, and (D) backbone fluorine atoms. Geometry optimizations were started by placing the CO_2 molecule at various positions around the TFIPA and TFSBA molecules. From five to eight different starting geometries were used for each of the polymer fragments. The hydrocarbon analogues, IPA and SBA, were studied in the same way.

4.2 TFIPA-CO_2 AND IPA-CO_2

Binding configuration (A) has an interaction energy of -15.9 kJ/mol. The optimized geometry for binding configuration (A) is shown in Figure 12. The dashed lines indicate interaction

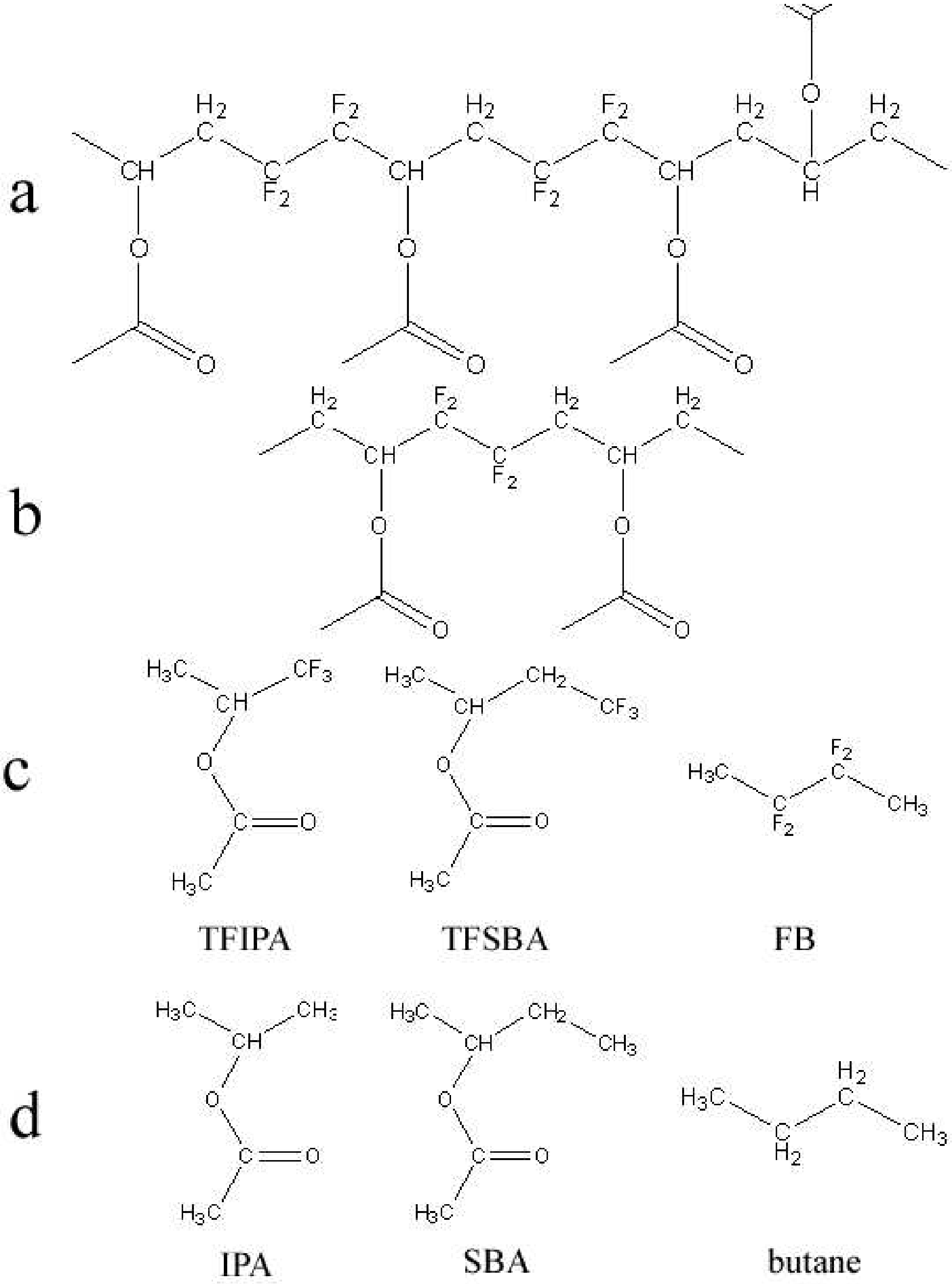

Figure 10: Structure images for TFE-co-VAc and etc. (a) a portion of poly(TFE-co-VAc) that lacks TFE block segments; (b) a representative segment that of this copolymer; (c)the three small molecules used in molecular modeling that capture the features of the copolymer, tri-fluoro isopropyl acetate, tri-fluoro sec-butyl acetate,tetrafluoro-butane; (d) the hydrocarbon analogs of the small fluorous molecules isopropyl acetate, sec-butyl acetate, n-butane.

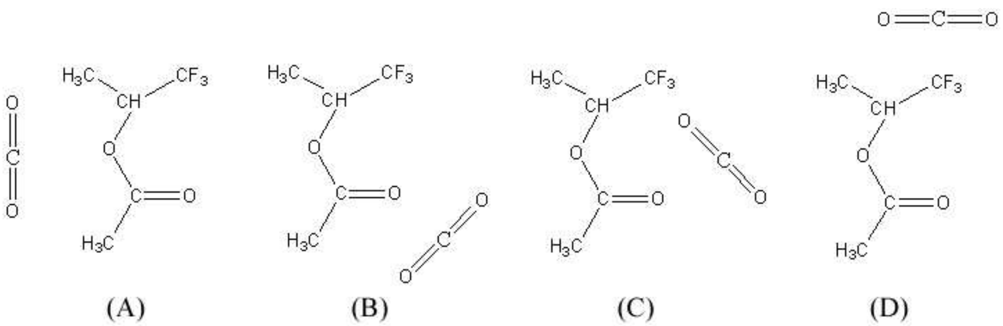

Figure 11: Four distinct binding configurations for TFIPA and a single CO_2 molecule. (A) Binding with the ether oxygen. (B) Binding with the carbonyl oxygen, tilting towards the methyl group. (C) Binding with the carbonyl oxygen, tilting towards the ether group side. (D) Binding with the fluorine atoms in the backbone.

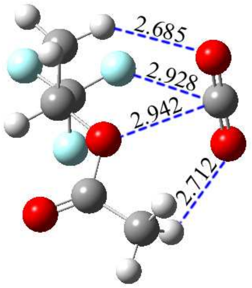

Figure 12: Binding interactions of TFIPA-CO_2 for configuration (A). The distances are in Ångstroms.

points between the two molecules. The atom-atom distances are also shown. The carbon atom of the CO_2 molecule binds both with the fluorine atom and the ether oxygen atom on TFIPA in this configuration. Each oxygen on CO_2 interacts with a hydrogen in what can be termed a weakly hydrogen bonding configuration.[34] We identify configuration (A) as quadradentate binding because the CO_2 molecule has four interaction points with the polymer moiety. In configurations (B) and (C), the CO_2 molecule mainly interacts with the carbonyl oxygen atom of the TFIPA. This gives interaction energies that are quite similar to those between IPA and CO_2. Figure 13 shows the interactions for configuration (D). This is also a quadradentate binding configuration. The CO_2 carbon interacts with two fluorine atoms while one CO_2 oxygen interacts with two hydrogens.

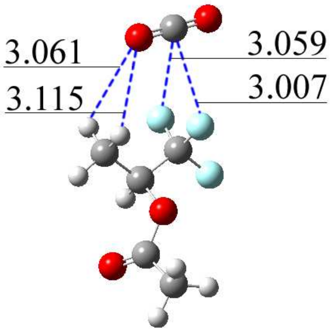

Figure 13: Binding interactions of TFIPA-CO_2 for configuration (D). Distances are in Ångstroms.

The binding energies for the four TFIPA-CO_2 binding configurations are listed in Table 2, along with the interaction energies for CO_2 with the hydrocarbon analogue, IPA. There is a difference of about 1.3 kJ/mol between the binding energies of TFIPA-CO_2 and IPA-CO_2 for configurations (A), (B) and (C). This energy value is within the uncertainty of the *ab initio* calculations. We conclude that the fluorine atoms on the polymer backbone do not substantially affect (positively or negatively) the binding energies of CO_2 with the acetate side chain.

Table 2: Binding energies for TFIPA-CO_2 and IPA-CO_2 at each of the four binding configurations of Figure 11. Geometries optimized at the MP2/6-31+G(d) level of theory with binding energies computed at MP2/aug-cc-pVDZ.

	Binding energies	
Binding modes	TFIPA-CO_2(kJ/mol)	IPA-CO_2(kJ/mol)
(A)	-15.9	-14.7
(B)	-13.0	-14.2
(C)	-15.9	-15.9
(D)	-9.6	No minimum

We have not been able to find a configuration (D) for the IPA-CO_2 system, even though we started from several different initial configurations. In every case, the CO_2 molecule always migrates around the molecule to bind with the carbonyl or ether oxygen of the IPA molecule. This implies that there is no minimum corresponding to binding configuration (D) for the IPA-CO_2 system. However, the (D) geometry of TFIPA-CO_2 system shows a considerable binding energy of -9.6 kJ/mol. This additional binding site for the TFIPA-CO_2 system is probably one of the main reasons for the increase in solubility of the poly(TFE-co-VAc) molecule in CO_2.

4.3 TFSBA-CO_2 AND SBA-CO_2

The TFSBA-CO_2 system was investigated using similar binding configurations to (A), (B), (C) and (D) of the TFIPA-CO_2 system. The SBA-CO_2 system was used for comparison. Table 3 lists the calculated binding energies for these systems.

The calculations for TFIPA-CO_2 and IPA-CO_2 indicate that the binding energies for configurations (B) and (C) should be similar for the fluorinated and non-fluorinated segments. We therefore did not calculate binding energies for configurations (B) and (C) for the SBA-CO_2 system. We use the values of the binding energies for configurations (B) and (C) from

Table 3: Binding energies for TFSBA-CO_2 and SBA-CO_2 at each of the four binding configurations of Figure 11. Geometries optimized at the MP2/6-31+G(d) level of theory with binding energies computed at MP2/aug-cc-pVDZ.

	Binding energies	
Binding modes	TFSBA-CO_2(kJ/mol)	SBA-CO_2(kJ/mol)
(A)	-18.8	-16.3
(B)	-13.8	-14.2[a]
(C)	-15.5	-15.9[a]
(D)	-11.7	No minimum

[a] Estimated from IPA-CO_2 calculations

the IPA-CO_2 system as an estimate for the binding energies for SBA-CO_2 for the same configurations. The binding energy of configuration (A) for TFSBA-CO_2 is -18.8 kJ/mol, which is much larger than the binding energies for any site of any of the other systems. We have examined the NBO charge distributions of TFSBA and other molecules in order to determine the origin of the enhanced binding for configuration (A) of TFSBA-CO_2. The local charges on atoms of TFSBA are shown in Figure 14. Note that the charge on hydrogens H(1) and H(2) is about 0.26. This is significantly larger than on hydrogens in the same positions on SBA or on hydrocarbons, which is about 0.23. Thus, hydrogens H(1) and H(2) are more acidic than typical hydrocarbon hydrogens. This is due to the fact that they are on the carbon that is beta to the highly electronegative fluorines. Configuration (A) on TFSBA-CO_2 is a quadradentate binding site, with one CO_2 oxygen interacting with H(1). The acidic hydrogen acts as a better Lewis acid for the CO_2 oxygen Lewis base. This, we believe, is the reason for the enhanced binding of configuration (A) for TFSBA-CO_2.

The charges on the two oxygen atoms of TFSBA are very similar to those of SBA. This is why the binding energies of configurations (B) and (C) are very similar for all the system studied. Configuration (D) for the TFSBA-CO_2 system has a binding energy of -11.7 kJ/mol. This is larger than that for the same configuration on TFIPA-CO_2. We believe that the increase in binding energy is again due to the increased acidity of the hydrogens on the

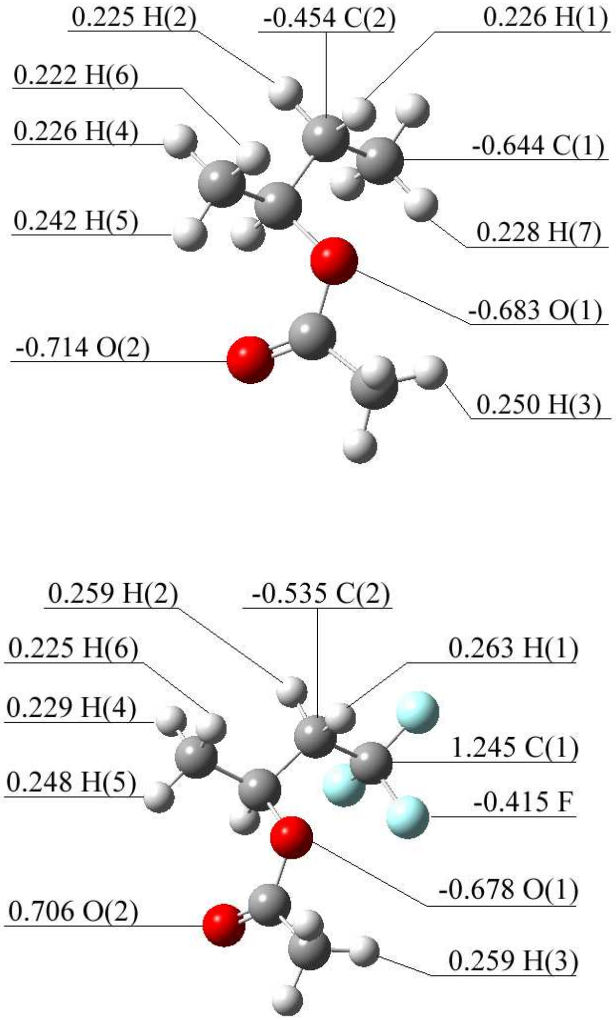

Figure 14: Charge distribution on the TFSBA (top) and SBA (bottom) molecules.

backbone. Note that our calculations could not locate a minimum for configuration (D) for SBA-CO_2, as was the case for IPA-CO_2.

4.4 FB-CO_2 AND BUTANE-CO_2

In order to further investigate the interactions between the CO_2 molecule and the backbones of the polymers, FB and butane are used as models of the fluorinated and non-fluorinated backbones, respectively. Starting from several initial configurations, we identified a single geometry with the strongest interaction for each of the systems. Figure 15 shows the optimized binding geometries for the systems. The binding energies for butane-CO_2 and FB-CO_2 are -8.4 and -12.1 kJ/mol, respectively. The FB-CO_2 binding energy is almost 3.7 kJ/mol larger in magnitude than that for butane-CO_2. The FB-CO_2 binding energy is close to the configuration (D) binding energies for TFIPA-CO_2 and TFSBA-CO_2. This indicates that the backbone of the semi-fluorinated polymers act as effective simultaneous Lewis acids (H-O) and Lewis bases (F-C) toward CO_2. These interactions are likely to significantly enhance the solubility of the polymer compared with non-fluorinated analogues. Note also that the

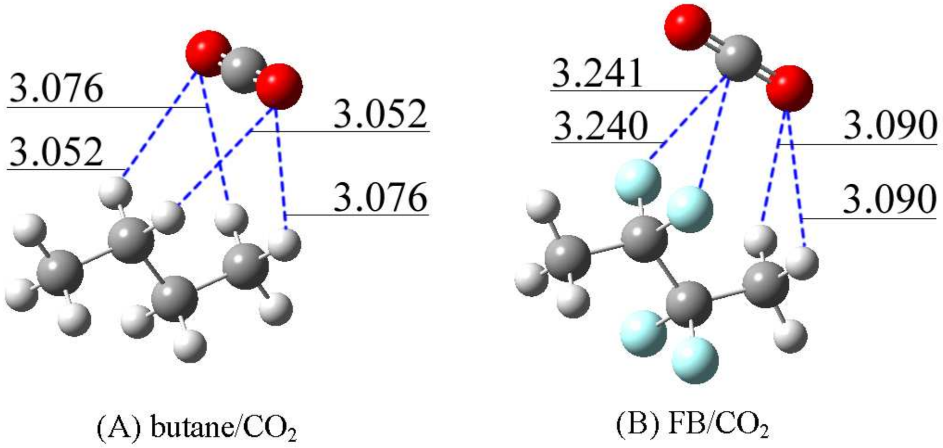

(A) butane/CO_2 (B) FB/CO_2

Figure 15: Optimized binding geometries for the n-butane-CO_2 and FB-CO_2 complexes. Distances are in Ångstroms.

acidic hydrogens are only available on semi-fluorinated backbones. This corroborates the experimental observation that high fractions of TFE in the co-polymer reduce the solubility.

4.5 DISCUSSION

A CO_2 molecule can act simultaneously as both a Lewis acid and as a Lewis base if the molecule with which it is interacting has both Lewis base and acid groups. Our molecular modeling results show that this is precisely the case for semi-fluorinated polymers such as TFE-co-VAc. Perfluorinated polymers lack Lewis acid sites. Furthermore, O-F interactions are only weakly attractive since both the oxygens in CO_2 and the fluorine in the polymer are electron-rich.[28] This is one of the major reasons that partially fluorinated polymers are more CO_2-philic than perfluorinated ones. Raveendran et al. have also observed enhanced binding of CO_2 with partially fluorinated molecules. They performed *ab initio* calculations on CF_nH_{4-n}–CO_2 for n=0 to 4. They concluded that there may be an optimal density of fluorine atoms in a molecule leading to maximum CO_2-philicity.[29] They attribute this optimal density to the competition among the individual electronegative fluorine atoms. In other words, fluorine atoms in highly fluorinated molecules are less effective electron donors. We believe this effect to be of minor importance compared with the requirement for a molecule to have both Lewis acid and base sites present in the correct geometry to interact simultaneously with CO_2. This is difficult to achieve in a small molecule like CF_nH_{4-n}.

Another important consideration is that fluorination of methane makes the hydrogen atoms become less acidic compared with hydrogen atoms in non-fluorinated methane.[29] This is not the case for larger molecules. The hydrogen atoms on the β-carbon to the fluorine atom are more acidic hydrogen atoms of n-butane. NBO charges for hydrogens on FB and butane are about 0.26 and 0.23, respectively. The enhancement of H-atom acidity relative to the hydrocarbon cannot be observed by studying semi-fluorinated methane.

Binding of CO_2 to carbonyl functional groups is virtually unaffected by the fluorination, as shown in Table 2. In contrast, Raveendran et al. noted that fluorination decreases the carbonyl CO_2-philicity of partially fluorinated acetaldehyde.[29] This decrease is only observed for very small molecules. Separation of the fluorine atoms from the carbonyl group by more than one carbon atom mitigates the effect of the fluorine on carbonyl-CO_2 binding. Note that the charges on the ether and carbonyl oxygens in both TFSBA and SBA are almost identical, as shown in Figure 14.

5.0 PHASE BEHAVIOR OF OXYGEN-CONTAINING POLYMERS IN CO_2

5.1 INTRODUCTION

This chapter is taken from one of our paper in preparation, "Phase Behavior of Oxygen-Containing Polymers in CO_2".[65] The experimental work was done by Dr. Sevgi Kilic and Stephen Michalik. The author did all of the *ab initio* calculations.

We hypothesize that a CO_2-philic material should possess a relatively low cohesive energy density, a relatively low glass transition temperature (high flexibility and high free volume), and a number of Lewis base groups to promote polymer-CO_2 interactions.

It has previously been assumed that for acetate-containing molecules, carbonyl oxygens are the most important sites for CO_2 interactions. A number of studies have been carried out to characterize carbonyl oxygen-CO_2 interactions.[33, 34, 66] None of the studies of acetate-CO_2 interactions have considered the impact of the ether oxygen in the acetate group. However, there have been two studies that investigate the interaction of CO_2 with isolated ethers.[67, 68]

Van Ginderen suggested on the basis of infrared spectroscopy and *ab initio* calculations that van der Waals complex formation occurs between the dimethyl ether oxygen atom and CO_2 carbon atom. Upon consideration of the lower contribution of ether oxygens (compared to carbonyls) to the cohesive energy density of a material,[69] and the flexibility and rotational freedom gained by addition of an ether oxygen, utilization of ether groups in the design of a CO_2-philic material could be more important than the carbonyl group if the former is judiciously integrated into the polymer structure. In this study, we incorporated ether and carbonyl oxygens into relatively simple (structurally) polymer chains in various ways and assessed the effect of such groups on the phase behavior of the polymers. Further, we have employed *ab initio* calculations to attempt to explain the phase results and guide future synthetic efforts.

5.2 RESULTS AND DISCUSSIONS

Experiments have been done for the poly(vinyl acetate) (PVAc), poly(vinyl methyl ether) (PVME), poly(vinyl ethyl ether) (PVEE), and poly(allyl acetate) (PAA). PVAc was found to be the most CO_2-soluble among all of the four polymers. PVEE, despite its relatively higher surface tension and thus the higher cohesive energy density, is substantially more CO_2-soluble than PVME. PAA is the analog of PVAc with an single methylene spacer group between the backbone and the pendent acetate group. However, poly(allyl acetate) with comparable molecular weight with PVAc is not miscible with CO_2 at pressures up to 60 MPa.

We have computed interaction energies of CO_2 molecules with monomers of PVAc, PVME, PVEE, and PAA. These monomers are isopropyl acetate (IPA), methyl isopropyl ether (MIE), ethyl isopropyl ether (EIE), and isobutyl acetate (IBA), respectively. We have also studied methyl isobutyl ketone (MIK) in order to investigate the carbonyl-CO_2 interaction. The molecular structures of PVAc, PVME, PVEE, PAA, and MIK are shown in Figure 16.

We identified one favorable binding mode for the ether oxygen-CO_2 group and two different binding modes for the carbonyl oxygen-CO_2 group. The two carbonyl oxygen-CO_2 binding geometries, (A) and (B), mainly differ in the orientation of CO_2 with respect to the second molecule, as shown in Figure 17. The calculated binding energies for these systems are summarized in Table 4.

It has previously been assumed that for acetate-containing molecules, carbonyl oxygens are the most important sites for CO_2 interactions. A number of studies have been carried out to characterize carbonyl oxygen-CO_2 interactions,[33, 35, 66] yet none have considered the impact of the ether-like ester oxygen in the acetate group. However, there have been two studies that investigated the interaction of CO_2 with isolated ethers.[67, 68] Our results of *ab initio* calculations in Table 4 clearly show that interaction energies of CO_2 with ether oxygens

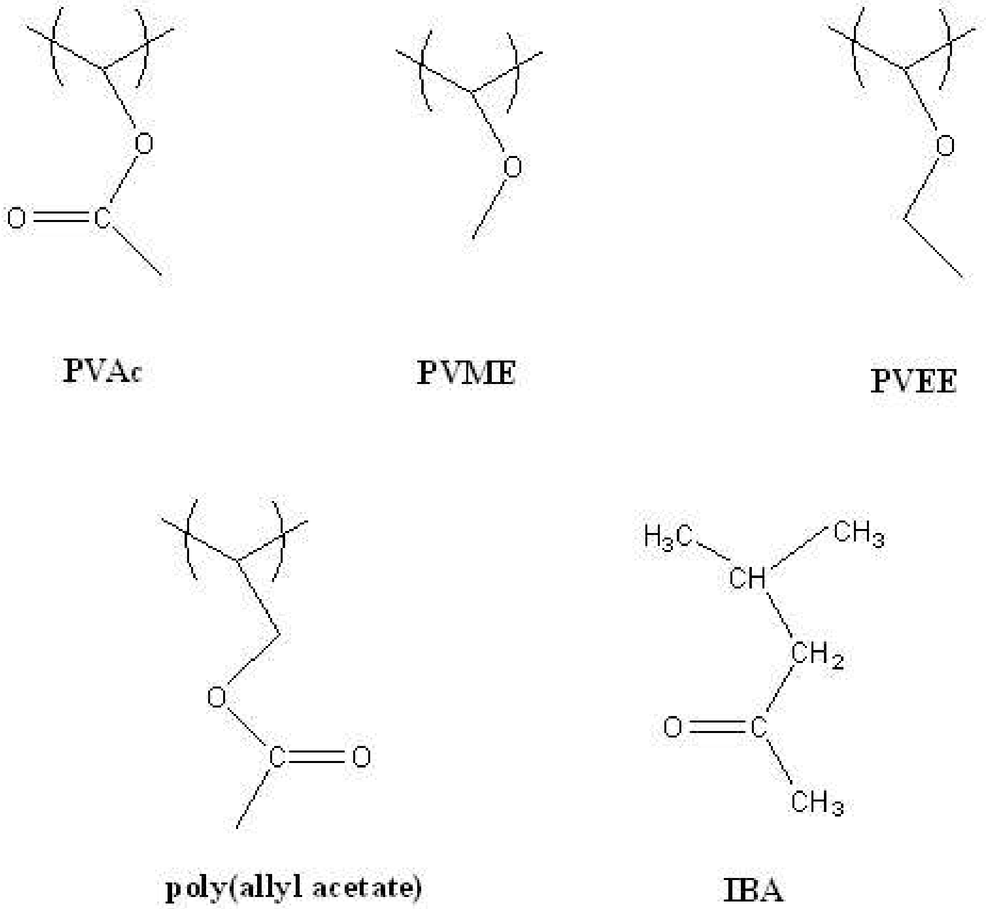

Figure 16: Molecular structures of poly(vinyl acetate) (PVAc), poly(vinyl methyl ether)(PVME), poly(vinyl ethyl ether) (PVEE), poly(allyl acetate) (PAA), and methyl isobutyl ketone (MIK)

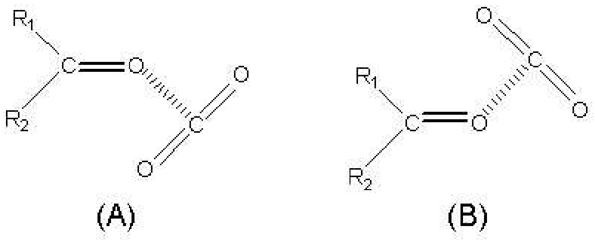

Figure 17: Two different binding geometries of carbonyl oxygen-CO_2 complex

Table 4: Interaction energies of various molecules with CO_2

Binding modes	Interaction energies (kJ/mol)		
	ether oxygen-CO_2	carbonyl oxygen-CO_2	
		(A)	(B)
IPA	-14.8	-14.2	-15.9
MIE	-18.0	N/A	N/A
EIE	-18.6	N/A	N/A
IBA	-15.1	-14.1	-14.3
MIK	N/A	-13.6	-16.0

in acetate groups and in isolated ethers are as favorable as those associated with carbonyl sites. For example, the binding energy of CO_2 with the ether oxygens in both IPA and IBA are comparable with the CO_2 binding to the carbonyl oxygens. Furthermore, isolated ethers (MIE and EIE) have binding energies larger than those in an isolated carbonyl (MIK). Note that the calculations presented here are for small molecules and do not account for the entropic and polymer-polymer contributions to solubility. Hence, one cannot directly predict the solubility of polymers from these calculations. Nevertheless, these results indicate that ether containing polymers are likely to be CO_2-philic.

Our experiments confirm that the presence of ether-linkages in a molecule is very important to lower miscibility pressures in CO_2. Figure 18 shows the phase behavior of poly(propylene) with a molecular weight of 425 (PP-425) and poly(propylene glycol)-mono-methylether (PPG-MME) (Mw=1,000)[70] in CO_2.

It should be noted that poly(propylene) with a molecular weight of 1,000 (PP-1000) is not miscible with CO_2 at concentrations above 0.5 weight percent at pressures below 50 MPa. PPG MME is miscible with CO_2 at much lower pressures than PP-425, despite the higher molecular weight and inclusion of a terminal hydroxyl group. Note that both polymers exhibit the same surface tension (31 mN/m at 20 °C), and hence solute self interaction is not an overriding factor here. The phase behavior results suggest that the ether oxygens in

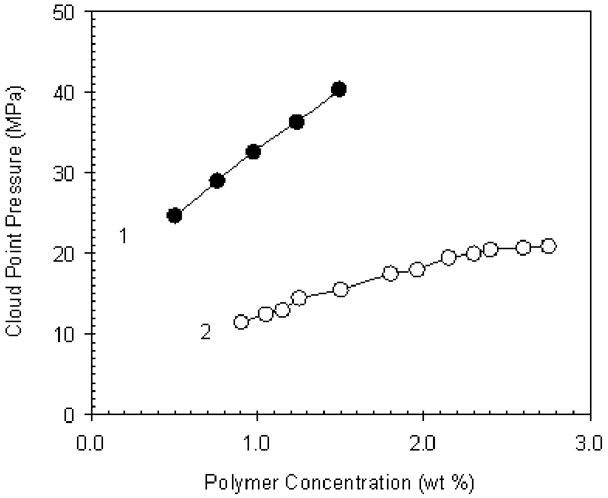

Figure 18: Phase behavior of 1. PP-425 (filled circles), 2. Poly(propylene glycol)-mono-methylether (Mw=1000) (open circles), at 295 K.

the PPG-MME are responsible for its superior miscibility compared to that of PP-425. In addition to providing a site for specific interactions, it is likely that the presence of oxygen in the PPG-MME enhances the entropy of mixing versus polypropylene. High molecular PPG exhibits a lower T_g than atactic poly(propylene), suggesting higher flexibility and free volume in the former. In addition, the value for σ, the ratio of the actual chain dimension to that of a freely rotating chain, is higher for atactic poly(propylene), suggesting that polypropylene is a stiffer chain. In summary, the addition of the ether oxygen to the backbone has a dramatic effect on phase behavior, apparently via the creation of sites for specific interactions with CO_2 and secondarily via enhancement of chain flexibility and thus entropy of mixing.

The phase behavior of two isomeric polymers of similar molecular weight, namely poly(vinyl methyl ether) (PVME) and poly(propylene glycol)-dimethylether (PPG-DME), was tested to assess the effect of oxygen placement on the phase behavior (Figure 19). As seen from the figure, placement of oxygen in the side chain has a positive effect on miscibility pressures (note that the PPG has a slightly lower molecular weight), although miscibility pressure curves show similar trends. The lower miscibility pressures of PVME can be attributed to relatively weaker self-interaction (lower surface tension, 29 mN/m at 25 °C). Although the

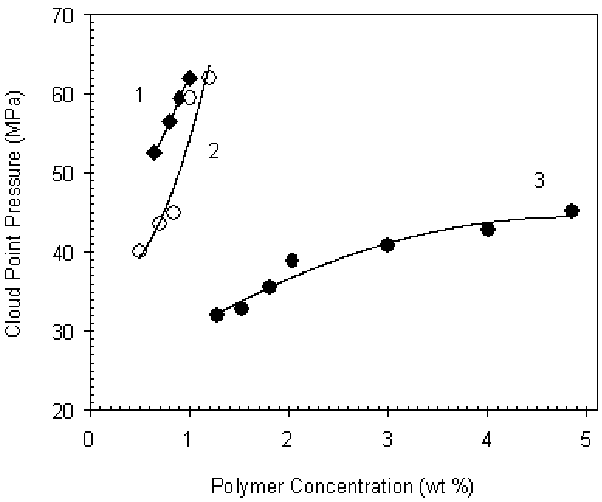

Figure 19: Effect of location of oxygen (backbone versus side chain) in the polymers on phase behavior: 1. PPG-DME (Mw=3500) (filled diamonds), 2. PVME (Mw=3850) (open circles), 3. PVEE (Mw=3800) (filled circles) at 295 K.

longer side chain branches of PVME might be expected to enhance free volume and hence the entropy of mixing,[38] the T_g of high molecular weight PVME is substantially higher than that of PPG, and the σ parameter for PVME is also substantially higher. The theoretical calculations do not differentiate between the PVME-CO_2 and the PPG-DME-CO_2 interactions, because the moieties used to represent these two polymers are identical. In summary, PVME is somewhat more CO_2-philic than PPG, possibly owing to slightly weaker self-interaction in PVME, but the exact source of the differences between these two polymers is not entirely clear.

Figure 19 also compares the phase behavior of PVME-3850 and PVEE-3800, where PVEE differs from PVME only by an extra methylene unit in the side chain. Despite the relatively higher surface tension and thus the higher cohesive energy density, PVEE is apparently more CO_2-philic than PVME. It has been suggested that as the side chain length increases, the polymer gains more free volume and thus the glass transition temperature decreases, resulting in enhanced entropy of mixing; this is indeed the case here, where high molecular weight PVEE exhibits a T_g of $-60\,^{\circ}$C versus $-31\,^{\circ}$C for PVME. Therefore, we surmise that the relatively better miscibility of PVEE (versus PVME) is entropically driven, although the ether oxygen in PVEE may also be more accessible to CO_2 for Lewis acid-Lewis base interactions due to the increased free volume. Regarding specific interactions between CO_2 and the ether oxygens, a single optimized geometry was obtained for the MIE-CO_2 dimer (analog to PVME), shown in Figure 20.

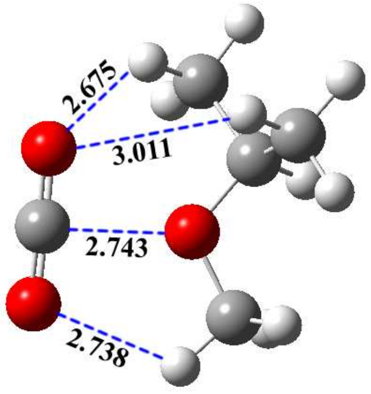

Figure 20: Optimized geometry for methyl isopropyl ether (MIE)-CO_2 complex. Interaction energy is -18.0 kJ/mol.

The interaction energy for this system is -18.0 kJ/mol. The charge on the ether oxygen is -0.684, as computed from an NBO population analysis. We also identified a single optimized binding geometry for the EIE-CO_2 complex (analog to PVEE), shown in Figure 21. The interaction energy is -18.6 kJ/mol and the NBO charge on the ether oxygen is 0.690. Hence, differences in the extent of specific interactions between CO_2 and the ether oxygens is not likely the basis for the differences in the phase behavior shown in Figure 19.

In summary, when one compares the behavior of PPG, PVME, and PVEE, it is clear that PVEE is the most CO_2-philic. Oddly, of the 3 polymers, PVEE also exhibits the highest surface energy, suggesting that PVEE exhibits the strongest self interactions. PPG exhibits both weaker self-interaction (lower surface tension) and is also a very flexible, high free volume material, yet PVEE exhibits substantially lower miscibility pressures. Our calculations

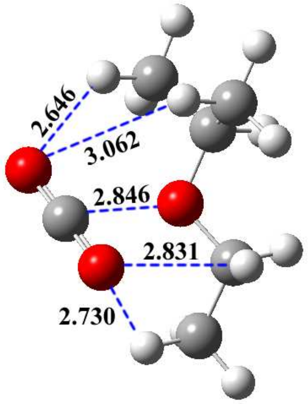

Figure 21: Optimized geometry for ethyl isopropyl ether (EIE)-CO_2 complex. Interaction energy is -18.6 kJ/mol.

do not reveal any clues to this behavior; a complete explanation of the effect of molecular structure on phase behavior in CO_2 is clearly still lacking.

Having observed that ether oxygens in the side chain, especially in PVEE, can reduce the miscibility pressures of polymers in CO_2, and knowing that incorporating an ether oxygen into the backbone (polyether) increases the chain flexibility and thus improves the miscibility, we prepared and tested the phase behavior of a series of polymers composed of a polyether backbone and number of methyl-ether groups in the side chain. Poly(epichlorohydrin) was chosen as a starting material and the side chain functionalization was then performed on this polymer, eliminating the effect of chain length and chain length distribution on the phase behavior. Also, by addition of methyl-ether groups to the epichlorohydrin polymer, analogs to PVEE were generated where the length of the side chain in the two polymer types is the same (the two side chains are isomers), and there is an extra oxygen in the backbone. It should be noted that the homopolymer of epichlorohydrin is not miscible with CO_2 at concentrations above 0.5 weight percent to the pressure limit of our equipment. We observed that 12% methyl ether substituted PPG partially dissolved in CO_2 at pressures as high as 50 MPa, but as the degree of substitution increased, the polymers remained substantially insoluble. It should be noted that the structure of the methyl ether-functional PPGs closely resemble that of a branched poly(ethylene oxide), which is known to exhibit poor miscibility in CO_2.[68] In summary, what appears to be a relatively small (and favorable) change in structure, the addition of a backbone ether oxygen (which was previously shown to be favorable in comparing PP to PPG) and the use of an isomer of the side chain in PVEE, produces an extremely negative change in the CO_2-philicity of the material. While this effect appears drastic, it is not without precedent. Rindfleisch and colleagues,[8] as well as Enick, et al.,[9] showed that the miscibility pressures of polymethyl acrylate and polyvinyl acetate differ by 100's of MPa, despite being isomers.

Figure 22 compares the phase behavior of PVEE with PVAc. These polymers exhibit

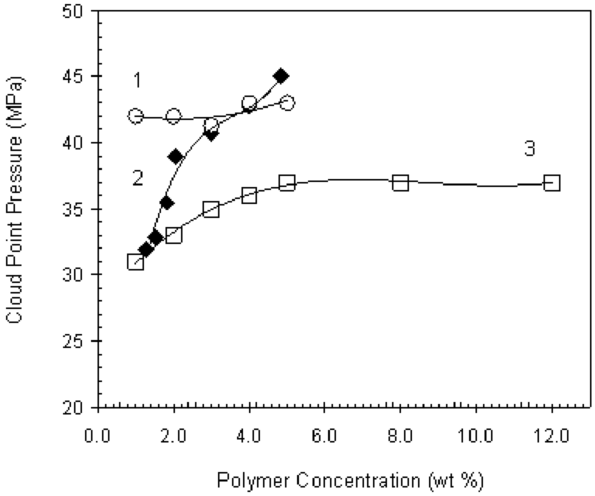

Figure 22: Comparison of phase behavior of 1. PVAc-7700 (open circles) 2. PVEE-3800 (filled diamonds) 3. PVAc-3090 (open squares) at 295 K.

the same cohesive energy density and the side chain lengths are also essentially the same. However, miscibility pressures for PVAc are clearly lower than those of PVEE in CO_2. Interestingly, the miscibility pressures for the two materials are comparable at low concentrations and diverge as concentration increases. This is not entirely surprising; the miscibility curves for each material must intersect the y-axis at the same point (CO_2's vapor pressure), while the rapid divergence shows how much more CO_2-philic PVAc truly is. It is also worth mentioning here that although PVAc with a molecular weight of 193,000 (2244 repeat units) exhibits miscibility with CO_2 at 67.6 MPa at 5 wt%,[9] PVEE with a molecular weight of 120,000 (1667 repeat units) is not miscible with CO_2 at 3.5 wt%, a pressure of 241 MPa, and elevated temperatures.

We used the IPA molecule as a reference to investigate the interactions of CO_2 with acetate groups and ether groups. We compared the interaction of CO_2 with the two oxygen containing groups in IPA with ether-CO_2 binding energies for MIE and EIE. Three different binding configurations were identified and are shown in Figure 23. The interaction energies are -14.8, -14.2 and -15.9 kJ/mol for ester oxygen binding, and carbonyl oxygen binding modes (A) and (B), respectively. (see Table 4) The NBO charges for the ester oxygen and the carbonyl oxygen of the IPA are -0.681 and -0.715, respectively. The interaction energies for the MIE-CO_2 and the EIE-CO_2 complexes are substantially higher than that of ether oxygen binding in the IPA-CO_2 complex (see Table 4). This indicates that isolated ether oxygens are more favorable than ester oxygens where interaction with CO_2 is concerned. The slightly more negative charge on the isolated ether oxygen (about -0.69) is consistent with this observation, since the larger charge gives a better Lewis acid-Lewis base interaction. However, this small difference of charges cannot completely explain the 3.2 to 3.8 kJ/mol difference in the interaction energies. Other factors contributing to the difference in the binding energies are discussed below.

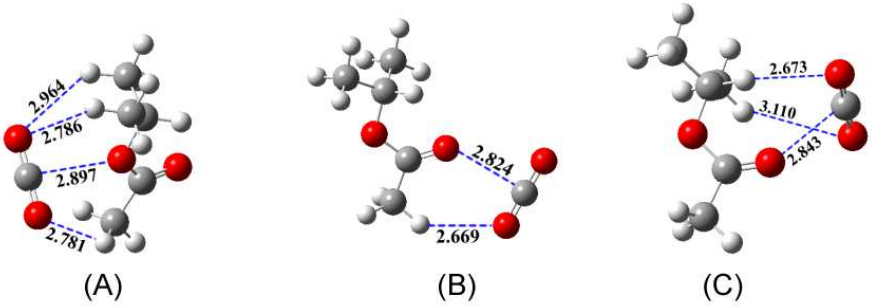

Figure 23: Three optimized binding geometries of isopropyl acetate-CO_2 complex.

The distance between the ether oxygen and the carbon of the CO_2 molecule ($O\cdots C$) for the MIE-CO_2 dimer is 2.743 Ångstrom (Figure 20), while the corresponding distance for the IPA-CO_2 dimer is 2.897 Ångstrom (Figure 23). The shorter O$\cdots$C distance for the MIE-CO_2 dimer contributes to the stronger interaction energy. Note that a MIE molecule has one less methyl group than an IPA molecule and hence has less steric hindrance for CO_2 approaching the ether oxygen; we believe this accounts for the shorter binding distance.

The O$\cdots$C distance for the EIE-CO_2 dimer is 2.846 Ångstrom (Figure 21), which is also shorter than for IPA-CO_2. In addition, we observe one extra "hydrogen bond" (H$\cdots$O) for the EIE-CO_2 dimer (Figure 21) as compared with the MIE-CO_2 and IPA-CO_2. The H$\cdots$O distances for the EIE-CO_2 dimer are all well within the definition of a C-H$\cdots$O "hydrogen bond".[71] This extra hydrogen bond contributes to the larger interaction energy.

Table 4 clearly shows that the binding energies of CO_2 with ester oxygens are weaker than binding energies for isolated ether oxygens. However, PVAc (the polymeric analog to IPA), is considerably more soluble in CO_2 than the polymeric analogs of MIE (PVME) and EIE (PVEE). The higher solubility of PVAc may be due to the fact that the acetate group has more binding modes available for CO_2, compared with the ether polymers. PVAc has three binding modes per monomer unit, one with the ester oxygen and two with the carbonyl oxygen (see Figure 23). The ether monomers can only accommodate one CO_2 near the ether oxygen. Therefore, the total interaction energy of an IPA-CO_2 dimer surpasses that of a MIE-CO_2 and a EIE-CO_2 dimer. In other words, "quantity" is more important than "quality", at least in this case.

In summary, PVAc is more CO_2-philic than PVEE, despite having comparable cohesive energy density (and hence comparable self-interaction strength). Further, high molecular weight PVAc exhibits a higher T_g than PVEE, which would suggest that PVEE exhibits greater chain flexibility and higher free volume. Nevertheless, PVAc exhibits lower miscibility pressures. Furthermore, it is also possible that the ester oxygen of PVAc provides rotational freedom to the carbonyl group, facilitating carbonyl-CO_2 interactions.

One might imagine that the interaction of CO_2 with either the ether oxygen in PVEE or the ester oxygen in PVAc would not be as favorable as carbonyl oxygen-CO_2 interactions due to steric hindrance from the long polymer backbone chain. If that were true, only the carbonyl group in PVAc would be involved in Lewis acid-Lewis base interactions with CO_2. In an effort to understand to assess the accessibility issue, methyl acetate-functional

PPGs of various degrees of substitution (12%, 22%, 44%, 69%, and 100%) were prepared. The polymers were generated via the modification of a homopolymer of epichlorohydrin. Interestingly, we observed that addition of methyl acetate side chains to polyether backbone shifts the miscibility pressure curve to higher pressures rather than lower. In other words, PPG with no methyl acetate substitution (100% reduced PECH) is more CO_2-philic than any of the methyl acetate-functional PPG's (Figure 24).

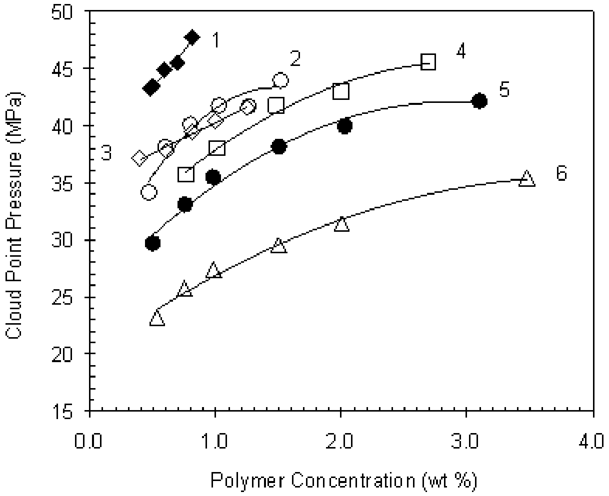

Figure 24: Phase behavior of methyl acetate-substituted PPGs, 1. 100% (filled diamonds), 2. 44% (open circles), 3. 69% (open circles), 4. 12% (open squares), 5. 22% (filled circles), 6. 0% (open triangles), at 295 K.

These results are consistent with those observed for the methoxy-functional polyepichlorohydrins, the presence of the single methylene group between either the methoxy ether or the acetate and the backbone has a severe deleterious effect on phase behavior. We have tried to explain this effect through *ab initio* calculations. The IBA molecule has a similar structure to IPA, albeit with a CH_2 group spacer between the isopropyl group and the ether oxygen. Similar to IPA, we obtained three optimized geometries for the IBA-CO_2 complex, shown in Figure 25.

The interaction energies for these three binding geometries are -15.1, -14.1 and -14.3 kJ/mol, respectively, giving an average binding energy of -14.5. The average binding energy for the IPA-CO_2 dimer is -15.0 kJ/mol, as can be seen from Table 4. This trend in interaction

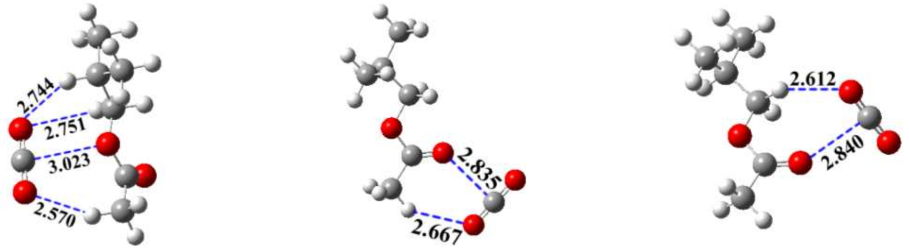

ether oxygen/CO_2 carbonyl oxygen/CO_2 (A) carbonyl oxygen/CO_2 (B)

Figure 25: Optimized binding geometries for isobutyl acetate (IBA)-CO_2 complex. Interaction energies are -15.1, -14.1, and -14.3 kJ/mol for the binding modes from left to right.

energies is consistent with the difference in CO_2 solubilities for polymers with a CH_2 spacer group. The NBO charges for the ether oxygen and the carbonyl oxygen of IBA are -0.675 and -0.707, respectively. These are also smaller in magnitude than the charges on the IPA oxygens (see above). The difference in charges on the oxygens is also consistent with the weaker interactions. However, the differences in interaction energies and partial charges are not nearly large enough to explain the dramatic differences in solubilities observed in experiments. We therefore conclude that other factors must exist that cannot be captured by our *ab initio* calculations.

From the data described above, it appeared that addition of a single methylene group between either pendant methyl ether or acetate groups and the polymer backbone created a serious adverse effect on miscibility with CO_2. To confirm this, we prepared the analog of PVAc with this additional methylene group, i.e., poly(allyl acetate). It has been shown previously that poly(vinyl acetate)s are miscible with CO_2 at relatively moderate pressures.[8, 9] Consistent with our results for the functional polyethers, poly(allyl acetate) with molecular weight of 7,800 (78 repeat units) is not miscible with CO_2 at pressures up to 60 MPa and concentrations at or above 0.8 wt%. By contrast, poly(vinyl acetate) with molecular weight of 7,700 (89 repeat units) is miscible with CO_2 at pressures of ca. 43 MPa at concentrations ranging from 0.5 to 5 wt% (Figure 24).[9] These results are entirely consistent with our data for methyloxymethyl and methyl acetate-functional polyethers-it is clear that incorporation of an extra methylene unit increases miscibility pressures dramatically.

Finally, we have performed *ab initio* calculations on isolated carbonyl oxygen-CO_2 moieties. We chose the MIK molecule, which contains only one carbonyl oxygen, as a model ketone compound. We identified two optimized binding geometries for the carbonyl oxygen-CO_2 interaction, (A) and (B), shown in Figure 26.

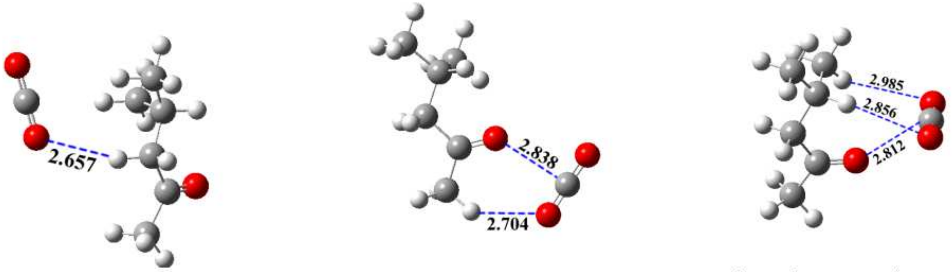

hydrogen/CO_2 carbonyl oxygen/CO_2 (A) carbonyl oxygen/CO_2 (B)

Figure 26: Optimized binding geometries for methyl isobutyl ketone (MIK)-CO_2 complex. Interaction energies are -7.5, -13.6, and -16.0 kJ/mol for the binding modes from left to right.

The interaction energies for the two binding geometries are -13.6 and -16.0 kJ/mol, respectively. We also performed optimization calculations by placing the CO_2 molecule on the opposite side of the carbonyl oxygen, where an ether oxygen would exist in an IPA molecule. This calculation resulted in a very weak binding mode (Figure 26), which contains virtually only $H\cdots O$ interactions and has an interaction energy of -7.5 kJ/mol. This is a much weaker binding than for the ether oxygen site on the IPA molecule.

The interaction energy of the geometry (A) of the MIK-CO_2 dimer is slightly lower than that of the IPA-CO_2 dimer, in spite of the very similar binding geometries for the two dimers. The interaction energies for mode (A) are -13.6 and -14.2 kJ/mol for MIK-CO_2 and IPA-CO_2, respectively. The isolated carbonyl oxygen of MIK is less electron-rich than the carbonyl oxygen of an IPA molecule, having NBO charges of -0.660 and -0.715 for the MIK and IPA carbonyl oxygens, respectively. The existence of the ester oxygen in the acetate molecule enhances the electronegativity of the carbonyl oxygen, which results in more favorable interactions with CO_2. The lower charge could result in slightly weaker $O \cdots C$ binding for the MIK-CO_2 complex. The lower interaction energy, coupled with the loss of the ester oxygen binding site, will very likely decrease the CO_2-philicity of the MIK molecule and also of polymers containing only ketone functional groups, relative to polymers with acetate groups. Experiments are needed to verify this prediction. One might expect that binding mode (B) for MIK would likewise be weaker than the corresponding mode (B) for IPA. However, the energies are roughly the same at -16.0 and -15.9 kJ/mol for MIK-CO_2 and IPA-CO_2, respectively. There are two reasons for the increased binding for mode (B) relative to mode (A) in MIK-CO_2. Firstly, the carbon on CO_2 is closer to the carbonyl oxygen in mode (B) than in mode (A), which increases the Coulombic interaction potential. Secondly, the $O \cdots H$ interactions between the oxygens on CO_2 and hydrogens on MIK are stronger for mode (B). Not only does mode (B) have two $O \cdots H$ interactions, but the H atom for which the $O \cdots H$ distance is 2.856 Ångstrom is more acidic (0.247) than the H atoms on the CH_3 group at the end of the MIK molecule.

5.3 CONCLUSION

The phase behavior of a series of model oxygen-containing polymers in CO_2 was measured to attempt to disentangle the coupled effects of self-interaction strength, cross interaction strength, and entropy on the miscibility pressures of polymers in CO_2. We can conclude that adding an ether oxygen to a hydrocarbon polymer, either in the backbone or the side chain, enhances "CO_2-philicity" by providing sites for specific interactions with CO_2 as well as by enhancing the entropy of mixing by creating more flexible chains with higher free volume.

Ab initio calculations show that ether oxygens, both isolated and in ester linkages, provide very attractive interaction sites for CO_2 molecules. The importance of the ester oxygens in acetate groups seems to have been ignored in previous studies. The binding energy for an isolated ether oxygen with CO_2 is better than that for a carbonyl oxygen-CO_2 complex. However, acetate functionalized polymers are more CO_2 soluble than polymers with only ether functionalities because acetate functional groups contain a total of three binding sites for CO_2 interactions, compared with only one for the ether functional group. Thus, quantity is more important that quality in this case. We predict that an isolated carbonyl oxygen (ketone functional groups) will be less CO_2-philic than acetate functionalized polymers. In summary, the existence of an ether oxygen in an ester molecule has two positive effects to the interactions with CO_2 molecules. First, it provides a much stronger attractive site than the CH_2 group for CO_2 interactions. Second, it makes the carbonyl oxygen more electronic rich and hence more favorable for CO_2 bindings.

6.0 DESIGN AND EVALUATION OF NON-FLUOROUS CO_2-SOLUBLE POLYMERS

6.1 INTRODUCTION

This chapter is taken from a paper in preparation, "Design and Evaluation of Non-fluorous CO_2-Soluble Polymers".[72] The experimental work was mainly done by Dr. Lei Hong. Inchul Kim, Jacob Crosthwaite, Andy Hamilton, and Mark Thies also had important contributions to the experiments. The author did all the *ab initio* calculations.

To date, a number of non-fluorous CO_2-philes, such as poly(propylene glycol), poly(vinyl acetate) (PVAc) and poly(ether-carbonate), have been identified.[8, 6, 7] For example, PVAc is the most CO_2-soluble, low or high molecular weight, oxygenated-hydrocarbon-based polymer (polymers that contain only C, H, and O) that has been identified. PVAc can dissolve in CO_2 at a pressure of 43.6 MPa from 1 to 5 wt% with a PVAc molecular weight of 125,000 (M_W, 145 repeat units based on weight-average molecular weight).[9] It is for this reason that PVAc oligimers have been successfully incorporated as the CO_2-philic tails of novel CO_2-soluble ionic surfactants.[73, 74] However, the dissolution of PVAc in CO_2 requires far greater pressure than is required for the dissolution of fluoroacrylate polymers.[2, 75, 76] The ideal CO_2-philic polymer with 10's - 100's of repeat units should exhibit miscibility in CO_2 under mild conditions (temperature $T < 100\,^{\circ}\mathrm{C}$ and pressure $P < 20\mathrm{MPa}$) at a concentration on the order of 1wt%. There is a critical need to develop non-fluorous polymers that have higher CO_2-solublity because no existing non-fluorous polymers fulfill these criteria.

Recent efforts in the area of CO_2-philic materials have focused on the rational design of non-fluorous CO_2-soluble polymers. Both experimental and theoretical approaches have been used in an attempt to identify the molecular-level features of a polymer that facilitate its solubility in CO_2. Beckman et al. have developed a set of heuristics for the design of CO_2-philic polymers.[77] that includes the following: (1) Flexible chains. Ether oxygen linkages, for example, can impart flexibility to the polymer backbones or side chains. (2) High free volume. branched structures, such as the tert-butyl group, can give rise to a high free volume. (3) Low crystallinity. Side chain branching structures generally decrease the crystallinity. (4) Low glass transition temperature (T_g). (5) Presence of functional groups that exhibit specific thermodynamically favorable interactions with CO_2, such as carbonyl oxygens.[32, 33, 34] and acetate groups.[8, 9] In addition, some molecular features have been found to have a negative impact on CO_2-solubility of polymers. Two examples are amine-functional groups and allyl polymers (polymers that have a -CH_2- spacer between the backbone and the pendant group or side chain). These heuristics have been used with some success.[77, 78, 65] However, our experience indicates that the heuristics are more likely to fail than to result in the successful design of a CO_2-soluble polymer. For an example, acetylation of a polymer side-chain alone does not ensure CO_2-solubility. Poly(methylene acetate) has a higher degree of acetylation than PVAc, yet it has a very high melting point and is insoluble in CO_2. Replacement of the methyl group in the side chains of PVAc with a tert-butyl group results in poly(vinyl pivalate), which should exhibit higher CO_2-solubility according to heuristics (2) and (3). However, poly(vinyl pivalate) does not dissolve in CO_2 at 1 wt%, 25 °C, and pressures up to 68.9 MPa. Finally, poly(methyl acrylate) (PMA) is an isomer of PVAc that has a T_g that is 19 °C lower than PVAc ($T_\mathrm{g} = 9\,°\mathrm{C}$ for PMA; $T_\mathrm{g} = 28\,°\mathrm{C}$ for PVAc), but PMA is much less soluble in CO_2 than PVAc.[9] For example, the cloud point pressures for PMA and PVAc in CO_2 are about 225 MPa and 64 MPa, respectively, for both polymers with a chain length of about 360 repeat units (based on weight average molecular weight) and at a concentration of 5 wt%. The lack of general design principles for CO_2-philic polymers highlights the need for a fundamental molecular-level understanding of the issues that govern solubility of polymers in CO_2.

One approach to investigate the specific interactions is to use molecular modeling. In principle, molecular modeling can be used to compute nearly all thermodynamic properties of the CO_2-polymer systems by using statistical mechanics simulations. However, these simulations require sufficiently accurate molecular potentials, which are not generally available.

An alternative method is *ab initio* quantum mechanical calculations. In principle, quantum mechanical methods are able to produce highly accurate interaction energies between CO_2 and specific polymer moieties.

Several groups have used quantum mechanics to characterize CO_2 interactions with small molecules. Nelson and Borkman used *ab initio* methods to investigate the splitting of the ν_2 vibrational mode for CO_2 interacting with carbonyl groups in small molecules, such as methyl acetate.[33] Raveendran and Wallen identified hydrogen bonding between the oxygen atoms of CO_2 and H atoms bonded to carbons in a target molecule as an important feature of CO_2-philic molecules.[34, 66] These C-H$\cdots$O hydrogen bonds are weaker than typical hydrogen bonds, but still substantially contribute the binding energy of CO_2 with molecules that are soluble in CO_2. Calculations by Kilic et al. suggest that the interaction energies between CO_2 and ether oxygens are as strong as between CO_2 and carbonyl oxygens.[13] Hence, ether groups may also play an important role in CO_2-polymer interactions. *Ab initio* calculations have shown that CO_2 can act simultaneously as both a Lewis-acid (carbon atom) and Lewis-base (oxygen atom) to form strong interactions with moieties that represent CO_2-philic polymers.[13, 64]

Quantum mechanics has typically been used to identify favorable interactions between CO_2 and molecules that are known to be soluble in CO_2, but has not previously been used to predict specific polymers that are CO_2-philic. We here report results for three new oxygenated-hydrocarbon-based polymers that were designed based on *ab initio* modeling of CO_2 interacting with small molecules. The corresponding polymers were synthesized and their cloud points in liquid (25 °C) CO_2 have been measured. This paper is the first attempt of which we are aware to design CO_2-solube polymers from the *ab initio* modeling. At the outset we acknowledge that there are severe limitations to *ab initio* modeling of CO_2-polymer interactions. First, it is impossible to model an entire polymer using high-level *ab initio* methods. One must represent the polymer with small moieties that mimic polymer segments. Only CO_2-polymer segment interactions can be computed because of very unfavorable scaling with the number of atoms in the system. Thus, no configurational entropy information is available from the calculations. Second, no polymer-polymer interactions are included in the calculations. Third, density effects of the solvent are not accounted for in the calculations.

Fourth, no temperature effects are included. Therefore, energeticically favorable interactions between CO_2 and polymer segments as calculated from first principles will not guarantee CO_2-solubility of the polymers. For example, PVAc and PMA have very different cloud point pressures in CO_2, as noted above, although *ab initio* calculations show that their monomers (representative moieties) have virtually identical interaction energies with CO_2.[13]

6.2 COMPUTATIONAL

We used *ab initio* molecular orbital methods to identify the binding modes of the candidate CO_2-philic molecules with CO_2. The small molecules chosen represent moieties contained in hypothetical polymers. The Gaussian 03.[63] software package was used for all our calculations. The calculation of the interaction energies between CO_2 and the molecules of interest as carried out in three steps. First, we made initial guesses for the configurations by placing a CO_2 molecule at various locations around the target molecule, close to the oxygen functional groups. Second, we used the MP2 level of theory with the 6-31+g(d) basis set to optimize the initial configurations. We chose this relatively small basis set to increase the efficiency of the optimization calculations. Finally, we performed single point energy calculations with MP2 and the Dunning aug-cc-pVDZ basis set[79] on the optimized structures to obtain more accurate interaction energies. Counterpoise (CP) corrections[59] were applied to the single point calculations to approximately account for the basis set superposition errors (BSSE). Extrapolation to the complete basis set limit is required to fully account for BSSE. However, complete basis set extrapolations are computational prohibitive. We therefore used the average of the raw and CP corrected interaction energies to approximate the complete basis set limit interaction energies. This method has been tested and used for similar systems.[13] This approach was suggested by Feller and Jordan.[62] All of the energetic data reported in this work are the average values of the raw and CP corrected energies. We have performed charge analysis calculations for the molecules of interest, using the natural bond orbital (NBO) method.[80]

6.3 MOLECULAR DESIGN

In this section we describe the rational for choosing the moieties on which the polymers are based. The moieties are designed and chosen based on the findings from some of our previous studies.

We have previously investigated the interactions between CO_2 and segments of poly(tetrafluoroethylene-co-vinyl acetate) (poly(TFE-co-VAc)); we have identified several factors that contribute the high solubility of poly(TFE-co-VAc) in CO_2.[13] We have also calculated the interactions between CO_2 and certain other oxygenated-hydrocanbon moieties.[65, 13] Through all the calculations, we rationalized several design principles.

First, CO_2 acts as both Lewis acid and Lewis base while interacting with the polymer. Therefore, both Lewis acid and Lewis base sites of the CO_2-philes should be arranged geometrically favorable for binding with CO_2 simultaneously. Multi-site bindings usually help with the interaction energies.

Second, more binding modes were found for the CO_2-fluorous molecule complex than the CO_2-nonfluorous analogue complex because of the fluorination of the backbone part, which is generally not CO_2-philic without the fluorination. Therefore, we attempted to additional CO_2 binding modes for the backbone part of the nonfluorous molecules using only C, H, and O.

Third, electron withdrawing groups, such as fluorine atoms, enhance the acidity of the nearby hydrogen atoms,[81] which is favorable for CO_2 interactions. While designing new molecules, we tried to create more acidic hydrogen atoms by only using oxygenated-functional groups and placing them properly. We found that the more acidic protons are always three bonds away from the electron withdrawing group. This pattern is shown in Figure 27. The electron withdrawing group attracts more electrons from its closet carbon atom, making the carbon atom more electrostatic positive. As a resonance effect, the more positive carbon atom thus induces the atom next to it to be less acidic and so on.

To further confirm this pattern, we have performed NBO calculations for some simple model molecules, as shown in Figure 28. The results agree with our observation very well. The acidic protons favor the binding of the molecule with CO_2. Therefore, one should be

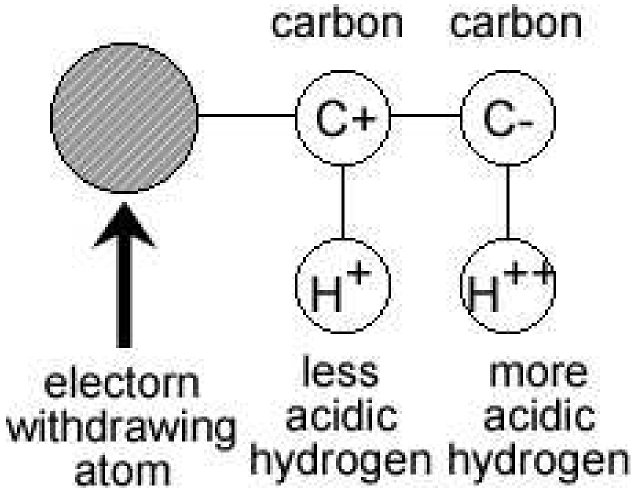

Figure 27: Effects of an electron withdrawing group on charge distributions. An electron withdrawing group, such as fluorine or oxygen, induces a partial positive charge on the α-carbon atom, but the β-carbon is negatively charged. Likewise, hydrogen bound to the α-carbon(β-carbon) is less(more) positive relative to alkane hydrogens.

aware of the creation of more acidic protons while designing new CO_2-philes. We performed a simple classical charge-charge interaction calculation, using Equation 6.1, to quantify the effect of hydrogen acidity on the O$\cdots$H interaction energy. Using the aldehyde in Figure 28 as an example, we chose the most acidic hydrogen atom (0.251), the least acidic hydrogen atom (0.145), and the oxygen atom (-0.632) to perform the calculations. The results are shown in Figure 29. We can see that the acidity of hydrogen atom does have important effects on the interaction energy, especially when r_{OH} is small, which is the case while hydrogen bonding forms. We should point out that the interaction energy values in Figure 3 are calculated from classical formula. Thus, they cannot be directly compared to the *ab initio* calculation results.

$$\Delta U = \frac{1}{4\pi\varepsilon_0}\frac{q_{\mathrm{O}}(q_{\mathrm{H(2)}} - q_{\mathrm{H(1)}})}{r_{\mathrm{OH}}} \tag{6.1}$$

We have designed three new possible non-fluorous CO_2-philic molecules based on the three design principles discussed above. In addition, we used the segments of poly(TFE-co-VAc) as model molecules to start the design, since the polymer was previously shown to be very

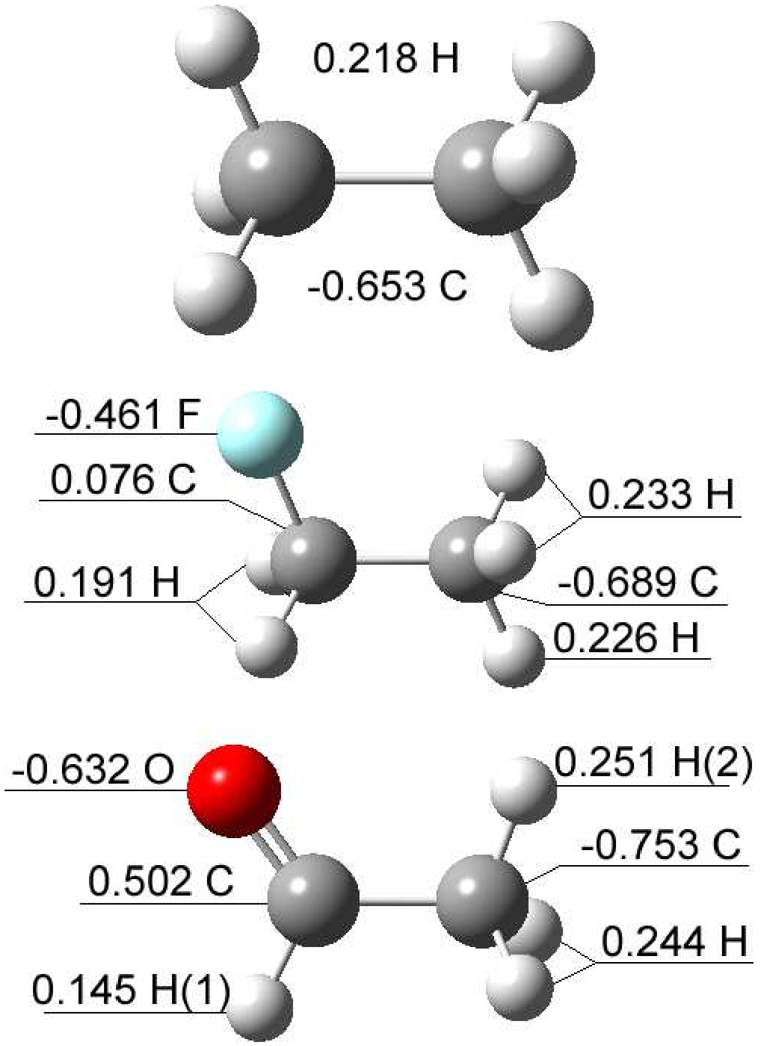

Figure 28: The effects of electron withdrawing groups on the acidities of hydrogen atoms. More acidic hydrogen atoms are usually separated by three bonds from the electron withdrawing groups.

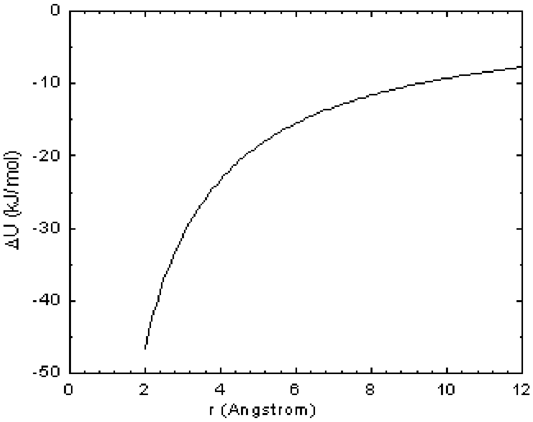

Figure 29: Effects of hydrogen acidity on O· · · H interaction energies. q_{O} = -0.632, $q_{\mathrm{H(1)}}$ = 0.145, and $q_{\mathrm{H(2)}}$ = 0.251. The energy difference deceases while the O· · · H distance increases.

CO_2-soluble.[64] The candidate molecules are methoxy isopropyl acetate (MIA), 2-methoxy ethoxy-propane (2MEP), and 2-methoxy methoxy-propane (2MMP), shown in Figure 30.

These molecules are composed of C, H, and O atoms only. They should be able to provide sites for CO_2 to interact with as both Lewis-acid and Lewis-base. The MIA molecule is modified from 4,4,4-tri-fluoro-sec-butyl acetate molecule (one segment of poly(TFE-co-VAc)) by replacing the CH_2-CF_3 group with an O-CH_3 group. We expect the additional oxygen atom will provide valuable binding sites in the backbone part for CO_2 molecules and also affect the acidities of nearby hydrogen atoms. 2MEP and 2MMP both have the diether structure. They are modified from 3,3,3-tri-fluoro isopropyl acetate molecule (another segment of poly(TFE-co-VAc)) by taking out the fluorination in the backbone and replacing the carbonyl oxygen with an O-CH_3 group. The substitutions of O-CH_3 groups are chosen to test ether oxygen atoms, which can provide more flexibility and interacts favorably with CO_2. In addition, the structures of all three molecules are expected to gain multi-binding sites for CO_2 molecule interacting with. For an example, the two ether oxygen atoms in MIA are expected to be able to bind with the carbon atom of CO_2 molecule simultaneously. That is also the case for the two ether oxygen atoms in the two diether molecules.

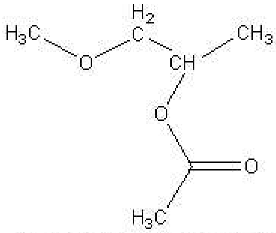

(a) methoxy isopropyl acetate (MIA)

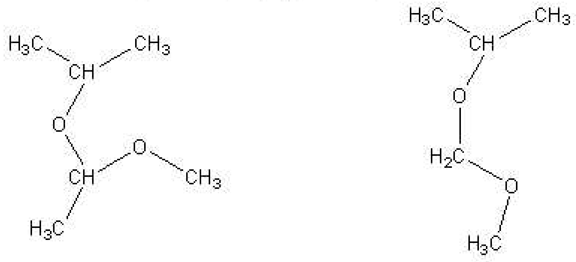

(b) 2-methoxy ethoxy-propane (2MEP)   (c) 2-methoxy methoxy-propane (2MMP)

Figure 30: Schematics of the three CO_2-phile candidates: (a) methoxy isopropyl acetate, (b) 2-methoxy ethoxy-propane, (c) 2-methoxy methoxy-propane.

6.4 RESULTS AND DISCUSSION

6.4.1 Methoxy isopropyl acetate (MIA)

MIA contains both ether oxygen and carbonyl group. These oxygen atoms can act as Lewis-bases while binding with CO_2. The pendant part of this molecule is the same as that of isopropyl acetate (IPA), which is the moiety used to represent PVAc.[64] One of the reasons for including the oxygen atom in the polymer backbone was to mimic the effect of fluorine in TFSBA. Therefore, we compare calculations for MIA with our previous calculations for IPA and TFSBA.[13, 64]

We performed NBO charge analysis for all of the three molecules shown in Figure 31. The charges on the atoms (H(1), O(1), and O(2)) of the pendant groups of all the three molecules are similar. This indicates that the pendant groups are not sensitive to the changes of the backbone. Therefore, we expect the interaction energies will be similar for the binding modes of CO_2 interacting with the pendant for all the three molecules. The presence of the electron

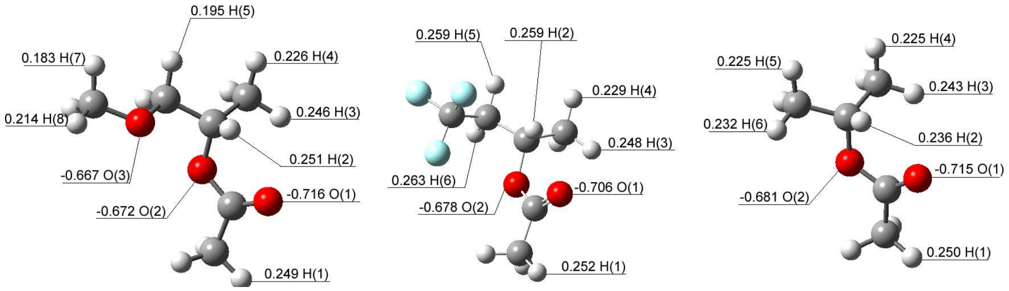

Figure 31: NBO charge distributions for methoxy isopropyl acetate (MIA) (A), 4,4,4-trifluoro-sec-butyl acetate (TFSBA) (B), and isopropyl acetate (IPA) (C)

withdrawing groups in these molecules makes some of the hydrogen atoms more acidic than the hydrogen atoms in a hydrocarbon molecule. As we have mentioned above, the more acidic hydrogen atoms are separated by three bonds from the electron withdrawing groups, while the hydrogen atoms on the alpha carbon atoms of the electron withdrawing groups are generally less acidic. Hydrogen atoms H(5) and H(6), which are on beta carbon atom of the fluorine atoms, are more acidic in TFSBA; Hydrogen atoms H(5), H(7), and H(8), which are on the alpha carbon atom of the oxygen atom (O(3)), are less acidic in MIA. The case of hydrogen atom, H(2), is relatively complicated. It is on the alpha carbon atom of O(2) and also on the beta carbon atom of O(1) in all of the three molecules. However, in MIA and TFSBA, H(2) has other electron withdrawing groups close to it. In MIA, the additional electron withdrawing group is the oxygen atom (O(3)). In TFSBA, the additional electron withdrawing groups are the fluorine atoms. Therefore, H(2) is more acidic in both MIA and TFSBA than in IPA.

We have identified five different binding modes for MIA interacting with a CO_2 molecule (shown in Figure 32). The dash lines represent the main interactions sites between MIA and CO_2 molecules. In binding mode (A) and (B), the carbon atom of CO_2 molecule interacts with two oxygen atoms of MIA molecule (one ether oxygen and one carbonyl oxygen in (A), ester and ether oxygens in (B)). In binding mode (C), the carbon atom of CO_2 interacts mainly with the ether oxygen atom in the backbone of MIA molecule. In binding modes (D) and (E), CO_2 molecule mainly interacts with the pendant part of the MIA molecule.

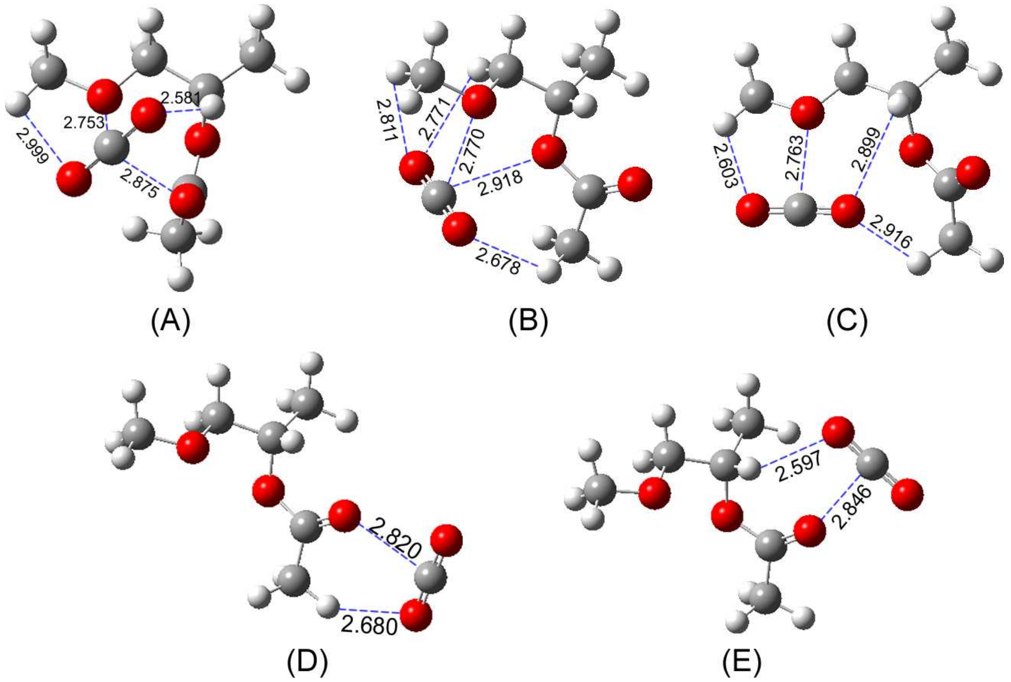

Figure 32: Five different binding modes of methoxy isopropyl acetate-CO_2 complex. Dash lines indicate the binding sites. Numbers are the distances between two atoms.

Both TFSBA and IPA molecules have similar binding modes with CO_2 as in (D) and (E) of the MIA-CO_2 system. In addition to the binding mode (D) and (E), the TFSBA and IPA molecules have another distinct binding mode, (F), where CO_2 interacts mainly with the ester oxygen.[13, 64] TFSBA has yet another binding mode, (G), were CO_2 mainly interacts with the backbone.[64] The interaction energies for the MIA-CO_2 system are listed in Table 5, along with the interaction energies for the TFSBA-CO_2 and IPA-CO_2 systems.

Table 5: Interaction energies (kJ/mol) of CO_2 with methoxy isopropyl acetate (MIA), 2-methoxy ethoxy-propane (2MEP), 2-methoxy methoxy-propane (2MMP), isopropyl acetate (IPA), 4,4,4-tri-fluoro-sec-buytl acetate (TFSBA), and 3,3,3-tri-fluro isopropyl acetate (TFIPA).

Binding mode:		(A)	(B)	(C)	(D)	(E)	(F)	(G)	Sum
Interaction energies	MIA-CO_2	-22.5	-23.6	-21.9	-14.3	-15.8	n/a	n/a	-98.1
	2MEP-CO_2	-18.4	-22.1	n/a	n/a	n/a	n/a	n/a	-40.5
	2MMP-CO_2	-20.2	-22.6	n/a	n/a	n/a	n/a	n/a	-42.8
	IPA-CO_2	n/a	n/a	n/a	-14.2	-15.9	-14.8	n/a	-44.9
	TFSBA-CO_2	n/a	n/a	n/a	-13.8	-15.5	-18.8	-11.7	-59.8
	TFIPA-CO_2	n/a	n/a	n/a	-13.0	-15.9	-15.9	-9.6	-54.4

Binding modes (A), (B), and (C) have stronger interaction energies than those for binding modes (D) and (E) for MIA-CO_2. This is to be expected because binding modes in (A)–(C) are at least "quadradentate" having four (or five for (B)) interaction points (dashed lines in Figure 33). In contrast, modes (D) and (E) are bidentate, as can be seen in Figure 33. The interaction energies for binding modes (D) and (E) of MIA-CO_2 are virtually identical to those of TFSBA-CO_2 and IPA-CO_2. We conclude that differences in the backbone of the molecules has a very small effect on the pendant groups. The NBO charge calculations we discussed before are also consistent with this conclusion (Figure 32).

MIA has more binding modes with CO_2 as compared with IPA and TFSBA (Table 5). Furthermore, these additional binding modes all have higher interaction energies with CO_2. It is tempting to use the sum of the binding energies (last column in Table 5) as a rough estimate of the CO_2 solubility of the corresponding polymer. However, this metric does not in any way account for polymer-polymer interactions or binding modes that may appear or disappear as one goes from small moieties to full polymers. Nevertheless, the sum of binding energies does work as a figure of merit for comparing TFE-co-VAc and PVAc, the polymers represented by TFSBA and IPA. The binding energy sum for TFSBA and IPA are -59.8 and -44.9 kJ/mol, respectively, indicating that TFE-co-VAc should be more soluble in CO_2 than PVAc. This is indeed the case, as already discussed.[64] The MIA molecule clearly shows the strongest interaction energy with CO_2 compared with TFSBA and IPA. The binding energy metric indicates that a suitable polymer based on MIA should be quite CO_2-philic in terms of both "quantity" (number of binding modes) and "quality" (strength of individual binding modes).

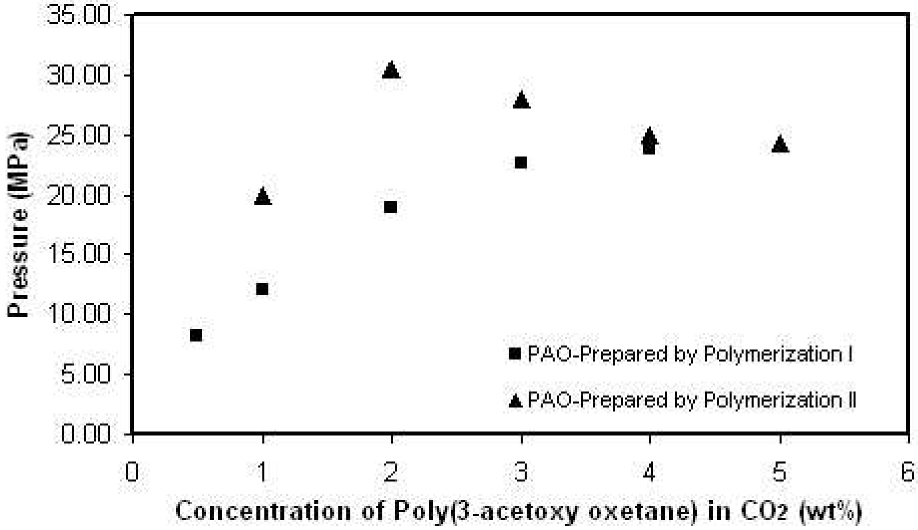

Figure 33: Pressure-composition diagram for the CO_2 + poly(3-acetoxy oxetane) system at 25 °C

We have measured the CO_2-polymer phase equilibria of the PAOs based on the MIA molecule. As we mentioned above, two samples of PAO were prepared using the previously described techniques. According to MALDI, the chain length of PAO are estimated about 8-mer and 7-mer for polymers made from polymerization I (the squares) and II (the triangles) shown in Figure 33, respectively. The two polymers displayed comparable cloud point pressures. The cloud point pressure of the PAO 7-mer is about 10 MPa higher than for PVAc with 11 repeat units,[9] when both are at 5wt%.

6.4.2 2-methoxy ethoxy-propane (2MEP) and 2-methoxy methoxy-propane (2MMP)

We have computed the NBO charges for 2MEP and 2MMP; these are given in Figure 34. The two molecules have very similar structures and both contain two ether oxygens. The only difference is that 2MEP has one more CH_3 group than 2MMP. Their charge distributions are similar, however, the additional CH_3 group in 2MEP renders some hydrogen atoms more acidic. We note that these more acidic hydrogen atoms are all on the beta carbon atom to the oxygen atoms; that is, the H atoms are separated from the O atoms by three bonds, as required by the heuristic discussed above.

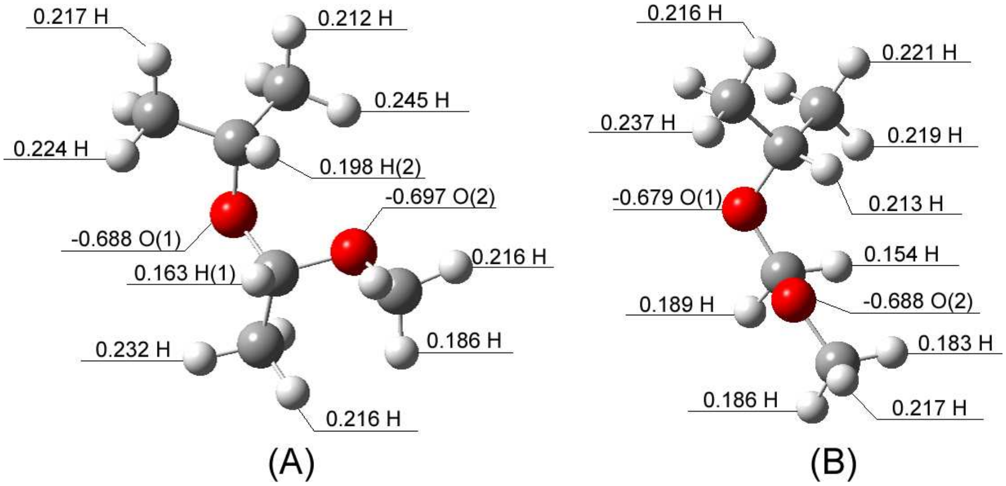

Figure 34: NBO charge distributions for 2-methoxy ethoxy-propane (A) and 2-methoxy methoxy-propane (B)

Two different binding modes have been identified using *ab initio* calculations for these molecules. They are shown in Figure 35 and Figure 36 for 2MEP and 2MMP, respectively.

We compare the binding energies to those for the TFIPA-CO_2 and IPA-CO_2 systems and report the results in Table 5. The binding modes for TFIPA-CO_2 and IPA-CO_2 systems are named as (D), (E), (F), and (G). For more details, please refer to our previous work.[64] The

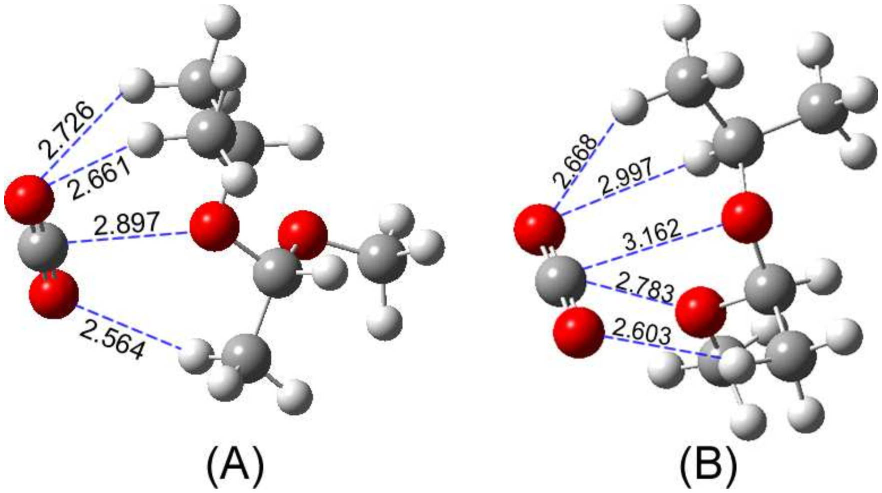

Figure 35: Two different binding modes for the 2-methoxy ethoxy-propane(2MEP)-CO_2 system. Dash lines indicate the binding sites. Numbers are the distances between two atoms.

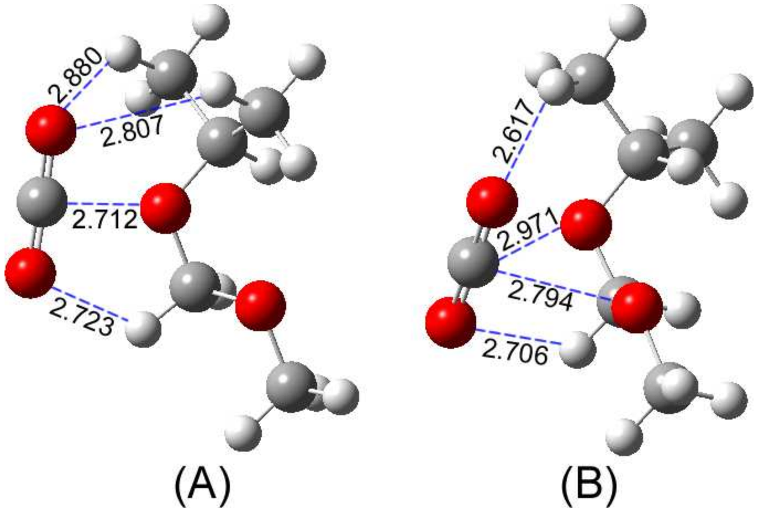

Figure 36: Two different binding modes for the 2-methoxy methoxy-propane (2MMP)-CO_2 system. Dash lines indicate the binding sites. Numbers are the distances between two atoms.

interaction energies for the 2MEP-CO_2, 2MMP-CO_2, IPA-CO_2, and TFIPA-CO_2 systems are listed in Table 5.

The NBO calculations show that 2MEP has more acidic hydrogen atoms than 2MMP. These more acidic hydrogens interact with the oxygen atom of CO_2 in binding mode (A). Note that the interaction energy of binding mode (A) for 2MMP is 1.8 kJ/mol stronger than the corresponding interaction energy for 2MEP. This is the opposite of what would be expected from the charge distribution alone. Close examination of the structures of binding mode (A) for both molecules indicates that the CO_2 molecule is closer to the oxygen in 2MMP than for 2MEP based on the $C\cdots O$ distance. The $C\cdots O$ interactions are likely to be more important than the $O\cdots H$ interactions because the charge on the carbon atom (1.25) in CO_2 is much larger than the charge on a hydrogen atom (<0.3 from our calculations) in an oxygenated-hydrocarbons. Therefore, the shorter $C\cdots O$ distance between 2MMP and CO_2 leads to stronger interactions that may compensate for the less acidic hydrogen atoms in 2MMP compared with 2MEP. The longer $C\cdots O$ distance for the 2MEP-CO_2 system compared with 2MMP-CO_2 is due to steric repulsion with the additional CH_3 group.

Finally, the $C\cdots O$ interaction (carbon atom of CO_2 and oxygen atom of the interested molecule) is even more important (energy wise) compared to $H\cdots O$ interaction. Although more acidic hydrogen atoms usually increase the CO_2-philicity of a molecule, the geometry required to achieve more acidic hydrogen atoms sometimes has negative effects to the $C\cdots O$ interactions. One should be careful of not sacrificing good $C\cdots O$ interaction for the more acidic hydrogen atoms. We did some simple model calculations to elucidate this point more clearly, shown in Figure 37.

Diethyl ether has more acidic protons and even more proton sites binding with CO_2. In addition, the polarizability of diethyl ether (7.692 Å^3) is larger than dimethyl ether (4.268 Å^3), which generally leads to stronger bindings with CO_2 molecules. However, the interaction energy between dimethyl ether and CO_2 are much stronger. We believe stronger $C\cdots O$ interaction exists in dimethyl ether-CO_2 system due to its shorter $C\cdots O$ bonding distance. Therefore, there exists tradeoff between good $C\cdots O$ interactions and good $O\cdots H$ interactions (acidic protons).

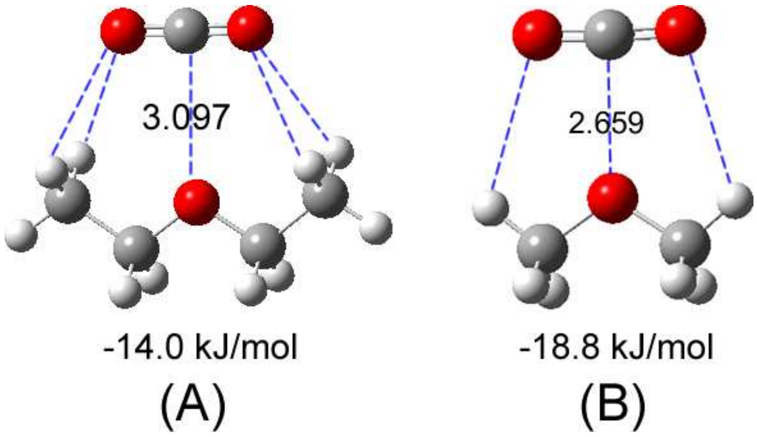

Figure 37: Interactions energies and binding modes of diethyl ether (A) and dimethyl ether (B) binding with CO_2 molecule. Geometric hindrance of CH_3 groups causes the CO_2 molecule being pushed further away from the diethyl ether molecule.

The CO_2 molecule acts as both a Lewis acid and a Lewis base in binding with 2MEP and with 2MMP. The CO_2 oxygens interact with hydrogens on the diethers. The carbon in CO_2 interacts with one of the two oxygens in the diether for binding mode (A), while the carbon interacts with both oxygens in binding mode (B) (see Figures 35 and 36). The binding energies for binding mode (B) are larger than those for binding mode (A), as can be seen from Table 5. The stronger binding for mode (B) is a result of the CO_2 carbon atom interacting with both ether atoms.

We have only been able to identify two binding modes for CO_2 with 2MMP and 2MEP, whereas other moieties tested here have from three to five identifiable binding modes (see Table 5). However, the strength of the 2MMP and 2MEP binding modes are quite large so that the sums of the binding energies are comparable to that for IPA, but smaller than those for the other molecules considered (see last column in Table 5). This raises issues of "quality" versus "quantity", i.e., will a small number of high-energy binding modes facilitate CO_2-solubility as well as a larger number of binding mode with smaller binding energy? This question cannot be addressed through quantum mechanical calculations.

The preparation of PVMEE and PVMME polymers are based on the prediction of CO_2-philicity of 2MEP and the 2MMP moieties, respectively. Increasing polymer free volume

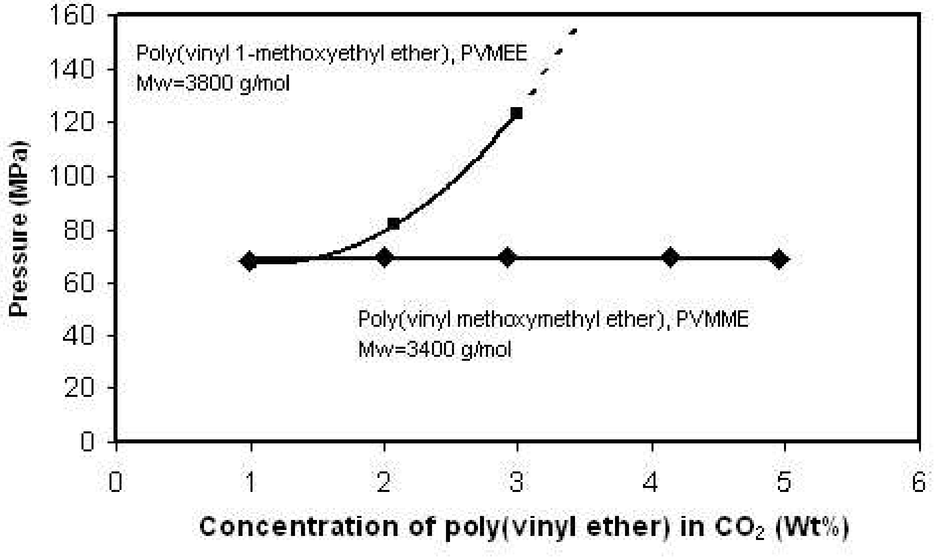

Figure 38: Pressure-composition diagram for CO_2 + poly(vinyl ether) systems at 25 °C

should increase the CO_2 solubility of a polymer, according to the heuristics discussed above. Therefore, we expected PVMEE to be more CO_2 soluble than PVMME because the additional methyl group in the PVMEE side chain should result in a larger free volume. The experimentally measured cloud point pressures for PVMEE and PVMME in CO_2 are plotted in Figure 38 as a function of polymer weight percent. At low weight percent solubility is driven by entropic considerations and both PVMEE and PVMME have similar cloud point pressures at 1 wt%. Enthalpic considerations become more important at higher concentrations and we see that the cloud point pressure for PVMEE increases dramatically with increasing weight percent (Figure 38). In contrast, the cloud point pressure curve for PVMME is remarkably flat. The reduced solubility (higher cloud point pressures) for PVMEE at higher concentrations may be attributable to the methyl group on the side chain sterically hindering CO_2 from accessing binding sites in the side chain. This is in qualitative agreement with the *ab initio* calculations, which indicate that the binding energy for mode (A) is smaller for 2MEP than for 2MMP due to steric repulsion. However, the difference in the binding energies is small and cannot account for the large difference in the observed solubilities.

Increasing free volume should decrease the glass transition temperature, indicating that PVMEE should have a lower T_g than PVMME because the extra methyl group on the PVMEE side chain should increase free volume. However, the T_g for PVMEE ($-1.20\,^\circ$C) is about $15.5\,^\circ$C higher than for PVMME ($-16.74\,^\circ$C). The extra methyl group in PVMEE apparently reduces the side chain mobility. Hence, part of the difference in CO_2-solubility between PVMEE and PVMME could be due to differences in the glass transition temperatures, although T_g is not always a good predictor of CO_2 solubility, as discussed above. Although PVMME was indeed CO_2-soluble, it required much higher pressure for dissolution at 5wt% in CO_2 than PVAc.[9]

We assess the usefulness of sum of the calculated binding energies, reported in the last column of Table 5, for predicting CO_2 solubility of the new polymers. 2MEP and 2MMP have a binding energy sum that is similar to that of IPA, indicating that PVMEE and PVMME should be similar to PVAc in CO_2 solubility. This, however, is not the case. PVMEE is not soluble at 5 wt% at any experimentally accessible pressure. PVMME is soluble at 5 wt% but has a cloud point pressure roughly double that of PVAc with a similar molecular weight (Figure 39). The higher cloud point pressures for the diether polymers may be due (in part) to fewer CO_2 binding modes available for the diethers compared with other molecules, as discussed above.

The sum of binding energies is highest for MIA (Table 5) and by this measure the PAO polymer should have the highest solubility in CO_2 of the polymers assessed in this work. This, however, is not the case. At 5 wt% PAO exhibits a higher cloud point pressure than PVAc with the similar number of repeat units (Figure 39). Obviously, the sum of binding energies does not appear to be an only predictor of the relative solubility of polymers.

There are certainly many factors that contribute to the solubility of a polymer that are not captured by a simple figure of merit such as the sum of binding energies. However, it is possible that the higher cloud point pressure observed for PAO is a result of PAO being terminated with CO_2-phobic hydroxyl end groups. Terminal groups can have a dramatic effect on the phase behavior of relatively short polymers.[83] It could be that a higher molecular weight PAO would have a lower cloud point pressure than PVAc with a similar chain

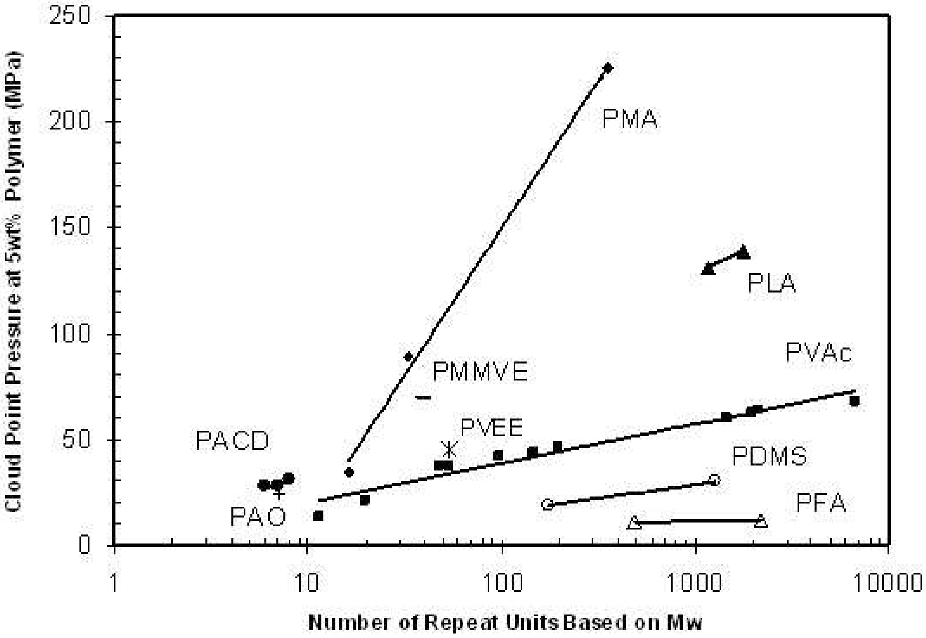

Figure 39: Could point pressures at ∼5% polymer concentration and 25 ^oC for binary mixtures of CO_2 with polymers as a function of number of repeat units based on weight average molecule weight, where PFA, PDMS, PVAc, PLA, PMA, PACD, PAO, PVEE and PVMME represent poly(fluoroalkyl acrylate)[9], poly(dimethyl siloxane)[9], poly(vinyl acetate)[9], poly(lactic acid)[9], poly(methyl acrylate)[9], per-acetylated cyclodextrin[82], poly(acetoxy oxetane), poly(vinyl ethyl ether) and poly (vinyl methoxymethyl ether), respectively.

length because the longer chain lengths would moderate the effect of CO_2-phobic end groups. Unfortunately, our previous attempts to synthesize a high molecular weight PAO have failed.

6.4.3 Conclusion

We have synthesized and evaluated three oxygenated hydrocarbon-based CO_2-soluble polymers based on the predictions made from *ab initio* modeling. The polymers, PAO, PVMME, and PVMEE, are naturally derived from the identified CO_2-philic "monomer" moieties, MIA, 2MME, and 2MEE, respectively. All three polymers are indeed soluble in CO_2 and represent new additions to the very short list of non-fluorous CO_2-soluble polymers. A summary of the cloud point pressures of polymers that show substantial solubility at 5%wt in CO_2 is given in Figure 39. Although PMMVE is less soluble than PVAc in CO_2, it is still more soluble than poly(methyl acrylate) (PMA). The ether oxygen close to the backbone in PMMVE does introduce an entropic favor for dissolving comparing the carbonyl group connecting with the backbone in PMA. A 7-mer per-acetylated cyclodextrins (PACD) has 21 acetate moieties totally while a 7-mer PAO only has 7 acetate moieties. But the cloud point pressure of PAO is slightly lower than that of 7-mer PACD. We concluded that the CO_2-philicity takes advantage of our structural design. The cloud point pressures of the three new polymers are higher than that of PVAc with a similar chain length. Nevertheless, the synthesis of three new polymers that dissolve in CO_2 is still a notable achievement, given that most polymers synthesized using the heuristic approach discussed above have not been soluble in CO_2 at 5 wt% and 138 MPa (the limit of our equipment).

We have made great attempts to use *ab initio* modeling as a guidance of designing new CO_2-philic materials. Although the theoretical results did not perfectly match the experimental results, they provided valuable information and insights. One can modify the current polymer moieties to design more new candidates or combine them together as co-polymers. However, in order to fully understand the mechanism of CO_2-solubility, statistical mechanical modeling is still required.

7.0 DEVELOPING STATISTICAL MECHANICAL SIMULATION PROGRAM FOR CO_2-POLYMER SYSTEMS: A NEW SIMULATION SCHEME

7.1 THEORY

The major thrust of our theoretical work will be to develop efficient methods for computing the cloud point curves of reasonably sized polymers in CO_2. To the best of our knowledge, there are no methods currently available for computing cloud point curves within molecular simulations. We propose a new simulation scheme, Hybrid Semi-grand Ensemble Monte Carlo.

This method is similar in spirit to the grand canonical Monte Carlo simulation. However, only CO_2 molecules will be inserted and deleted during the simulation. The simulation starts with a box of pure polymer. Multiple time-step hybrid Monte Carlo will be used to generate polymer configurations. After an equilibration period grand canonical Monte Carlo is carried out throughout the entire simulation cell, with trial creation and deletion of CO_2 molecules at a fixed chemical potential or bulk gas pressure. The system will then be equilibrated.

The algorithm is shown in 40. The semi-grand partition function is taken to be the first Legendre transform of the Gibbs free energy, transforming out the polymer chemical potential. The differential form is written as The ensemble of this simulation is described as following equation.

$$dM = -SdT + VdP + N_{\mathrm{CO_2}} d\mu_{\mathrm{CO_2}} - \mu_{\mathrm{P}} dN_{\mathrm{P}} \tag{7.1}$$

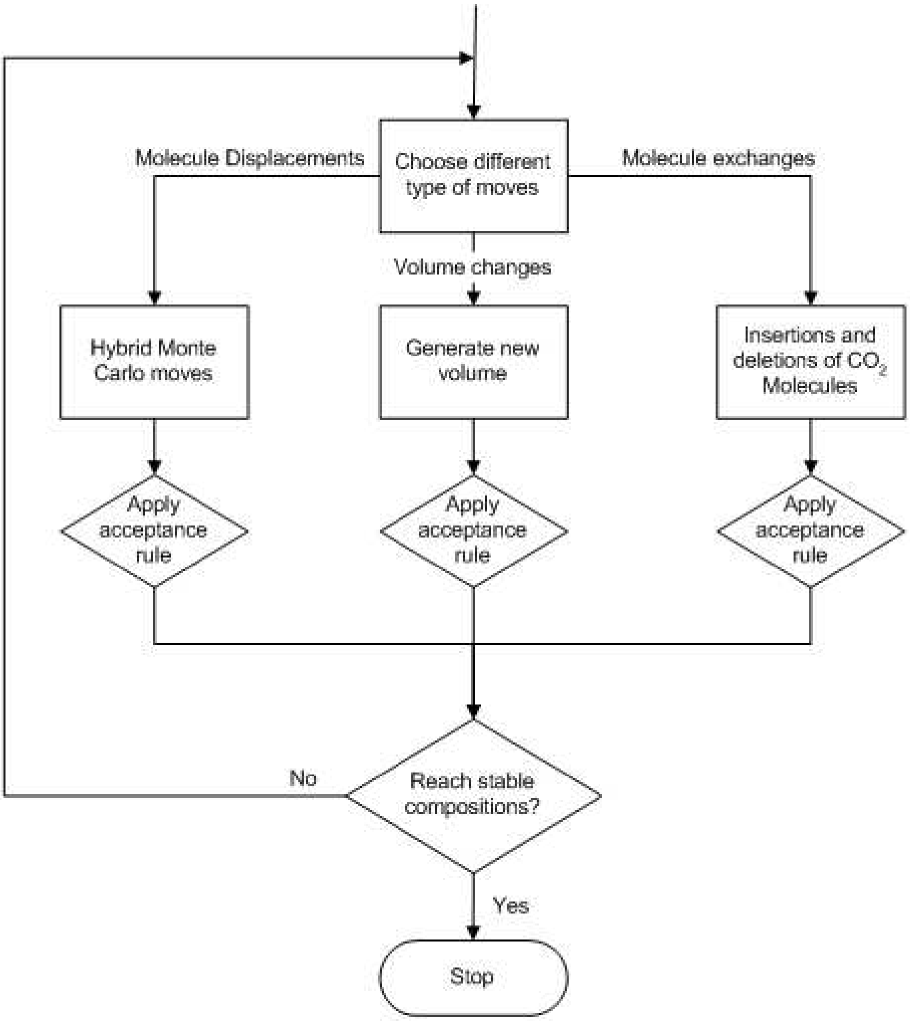

Figure 40: Flow chart of the Hybrid Semi-Grand Canonical Monte Carlo simulation for mixtures.

where μ_{CO_2} and μ_{P} are chemical potentials of CO_2 molecules and polymer molecules, respectively. N_{CO_2} and N_{P} are numbers of CO_2 molecules and polymer molecules, respectively. Equation 7.1 is the differential form of the first Legendre transform of Gibbs free energy (G).

The specified (canonical) variables are pressure, temperature, chemical potential of CO_2, and the number of polymer molecules in the system. The calculated variables are the volume (density) and number of CO_2 molecules in the system. A single simulation cell holds a given number of polymer molecules. The volume of the cell fluctuates to maintain the pressure at a fixed value. The chemical potential or fugacity of CO_2 is fixed so as to give a pressure of CO_2 that is close to, but slightly less than the system pressure. This is because the polymer vapor pressure is low, so that the total system pressure is due almost entirely to the CO_2 pressure (fugacity). If the system pressure is below the cloud point pressure for a CO_2-polymer mixture (e.g. 1 wt%), then number of CO_2 molecules in the system will increase until the concentration drops below 1%. In that case, the pressure of the system can be increased and a new simulation can be run. The advantage of this method is that the pressure is directly specified. The disadvantage is that several simulations must be run to identify a single cloud point. It will also be difficult to achieve a desired value of the weight percent polymer in the system with the semi-grand method.

7.2 TEST WITH SIMPLE MOLECULES

We have performed test calculations with the semi-grand ensemble. We coded the method and applied it to a hypothetical mixture of Kr-Ar that showed liquid-liquid equilibrium. The results are shown in Figure 41. The mixing rules have been modified so that the Kr-Ar interactions are much less favorable than the like-like interactions. Gibbs ensemble Monte Carlo has been used to generate the LLE phase diagram for this mixture, giving compositions of the Ar and Kr rich phases of 0.11 and 0.90 mole fraction Kr, respectively. Our semi-grand calculations are in excellent agreement with the Gibbs ensemble data. Note that only Kr was created or deleted in these simulations. This trivial example is a proof-of-concept that the semi-grand ensemble will work. The Gibbs ensemble method is much more efficient for this simple mixture, but will not work for complex mixtures of CO_2 and long-chain branched polymers.

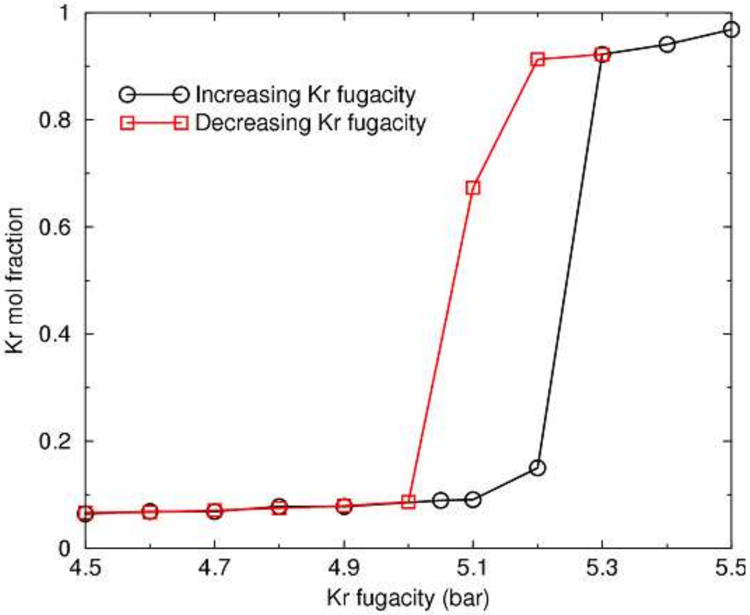

Figure 41: Test calculations performed within the semi-grand ensemble method for a hypothetical Kr-Ar mixture with the potential parameters tuned to give liquid-liquid equilibrium. The composition of the Ar and Kr rich phases from Gibbs ensemble calculations are 0.11 and 0.90 in Kr mole fraction, respectively.

8.0 ADSORPTION OF ALKANES ON SINGLE WALL NANOTUBES

8.1 INTRODUCTION

This chapter is adopted from one of our publications, “Observation of a one-dimensional adsorption site on carbon nanotubes: Adsorption of alkanes of different molecular lengths”.[84] The experimental work was done by Petro Kondratyuk. The author did all of the simulations work.

Single wall carbon nanotubes (SWNTs) have attracted significant scientific interest as adsorption media since their discovery. They are known to have high binding energy adsorption sites in the interior as well as in the grooves between adjacent nanotubes on the outside surface of SWNT bundles.[10, 11] The high binding energies on nanotubes, as compared to planar graphene sheets, stem from effective van der Waals interactions caused by the proximity of the curved nanotube walls in those adsorption sites.

Molecular adsorption in the interior, in the groove sites, and on the exterior surface of the nanotubes has been observed in a number of studies employing various experimental techniques.[85, 86, 87, 88, 89, 90, 91, 92] In the case of interior sites, an oxidative treatment is required to produce entry ports that allow the adsorbate molecules to access the nanotube interior.[93] Such entry ports are usually created during the oxidative acid purification of the nanotubes to remove graphitic impurities after synthesis. Oxidative treatment with gaseous O_3 followed by annealing at 1073 K has also been shown to strongly enhance adsorption kinetics into the interior by introducing additional entry ports on the nanotube walls.[93, 94] Here we present a combined experimental and simulational study of the adsorption of five linear alkanes, *n*-pentane to *n*-nonane, and a branched alkane molecule, 2,2,4-trimethylpentane on SWNT adsorption sites.

Adsorption of alkane molecules of different molecular length and shape on zeolites has been extensively studied.[95, 96, 97, 98, 99] It was found that generally the adsorption capacity depended inversely on the size of the molecule. However, this effect was masked by the structural peculiarities of zeolite adsorption sites, especially for shorter alkanes. In the case of carbon nanotubes, the adsorption space contains no charge centers and is more uniform at the atomic scale. Thus a smoother dependence of adsorption capacity on molecular length was to be expected for the molecules we studied, as was observed.

In this study, temperature programmed desorption (TPD) is the experimental tool used to characterize the adsorption of these different alkanes; Hybrid Monte Carlo simulations were used to probe the molecular-level details of alkanes adsorbed on different sites on the SWNT bundles. As these molecules are chemically very similar and differ only in carbon chain length (linear alkanes) or chain connectivity (2,2,4-trimethylpentane), observing the capacities of different SWNT adsorption sites toward them allowed us to extract information about the density of molecular packing in these sites as well as effects of the adsorption site geometry.

8.2 EXPERIMENTAL

Temperature programmed desorption experiments were performed in an ultrahigh vacuum (UHV) chamber equipped with a 150 L/s turbomolecular pump and a 360 L/s ion pump. The system achieved a base pressure of 2.5×10^{-10} Torr after bakeout.

The SWNTs used in the current experiments were produced by R. Smalley and collaborators using pulsed laser vaporization of graphite with a Ni-Co catalyst.[100, 101] They were purified using an oxidizing aqueous solution of HNO_3 and H_2SO_4 to remove catalytic and graphitic impurities present after synthesis.[102]

The tube diameter distribution was centered near 13.6 Å, while the most probable length was approximately 320 nm. The nanotube sample employed here has been extensively studied before.[91, 103, 104]

The nanotube sample weighing approximately 36 μg was deposited in air from a suspension in dimethyl formamide onto a gold plate measuring 10×14 mm. The solvent was then allowed to evaporate at room temperature.

The gold support plate was attached to the sample holder assembly inside the vacuum chamber via two tungsten support wires. By passing current through the wires the gold plate and SWNTs on it can be heated up to 1100 K. The sample holder also serves to thermally link the sample to a liquid nitrogen-filled dewar, allowing cooling to 89 K. A PID temperature control system was implemented to regulate the heating power fed to the tungsten wires. Temperature was monitored with a type K thermocouple attached to the gold plate. The thickness (0.5 mm) and excellent thermal conductivity of the gold plate served to prevent temperature gradients across the sample during TPD experiments.

An identical gold plate containing no nanotubes was used as a reference to observe the adsorption on the support plate itself. It was found that the maximum non-multilayer adsorption on the support plate comprised less than 1% of the amount of molecules adsorbed on the SWNTs due to the much larger surface area SWNTs provide for the adsorbate.

The sample and reference were heated to 1073 K for 10 minutes before every set of experiments in order to decompose oxygen-containing functionalities that might have been present on the nanotubes. Functional groups at SWNT entry ports have earlier been found to prevent molecular access into the interior of the nanotubes.[93]

Adsorbate delivery to the surface was accomplished by means of a collimated molecular beam doser with a limiting pinhole conductance.[105, 106] The limiting conductance was absolutely calibrated using Xe and CCl_4 effusion and found to scale inversely as the square root of molecular weight, as predicted by the classical effusion equation. The effusion rates for all alkanes were thus recalculated using the inverse square root of mass law from the CCl_4 value. For *n*-pentane the dosing rate at the sample surface was calculated to be 1.27×10^{13} C_5H_{12} Torr^{-1} s^{-1} cm^{-2}.

The temperature-programmed desorption experiment was conducted as follows. First the sample was rotated to the doser position remaining there for the required dosing time. Then the sample was reproducibly positioned ~1 mm in front of a shielded quadrupole mass spectrometer (QMS) and the temperature was linearly increased at a rate of 2 K/s to cause the desorption of the molecules and the QMS signal was recorded as a function of temperature. The end cap of the QMS shield was biased to -100 V to prevent stray electrons from the ionization chamber from reaching the sample.

All the data in this work was acquired with a semi-automatic computer controlled system earlier built specifically for large numbers of closely controlled temperature programmed desorption experiments. This system integrates the functions of sample translation between doser and QMS positions, temperature control and QMS signal recording. Its construction and operation are explained in detail elsewhere.[103]

After each temperature programmed desorption experiment an additional experiment that served to calibrate the sensitivity scale was carried out with the same adsorbate molecule. The calibration procedure involved taking a TPD desorption profile of a standard amount of the adsorbate (2.0×10^{15} molecules cm^{-2}) and dividing the preceding TPD profile by the integrated intensity of the calibration measurement. By multiplying the result by the number of molecules in the calibration exposure, a physically relevant measure of the desorption rate, in molecules cm^{-2} K^{-1}, could be obtained.

This calibration procedure served a double purpose. First, it corrected for the slow sensitivity drift in the mass spectrometer due to sensitivity changes in the electron multiplier. Secondly, it allowed a direct comparison of TPD spectra between different adsorbate molecules, because for all desorption experiments carried out after the calibration measurement, the areas under the TPD spectra correspond to the number of molecules that desorb over the temperature range in question.

This desorption rate is connected to the conventional kinetic rate, in molecules cm^{-2} s^{-1}, by the temperature increase rate dT/dt during the desorption experiment. The dosing temperature for the calibration experiment was chosen to be low enough to ensure unity sticking coefficient.

8.3 THEORETICAL

We used the hybrid Monte Carlo (HMC) method.[107] to perform the simulations on the nanotubes/alkane system. The HMC technique is reported to be more efficient than either MD or simple MC for simulating long-chain molecules.[108, 109] The multiple-time-step method[110] was used to integrate the intra-molecular degrees of freedom. The nanotube bundle used in the simulations consisted of two (10,10) nanotubes, each containing 20 unit cells (length 49 Å). The gap between the walls of the adjacent tubes was set to 3.2 Å. We chose this "minimal" SWNT bundle to reduce computational demands. The nanotube bundle was placed in the center of a cubic simulation cell 200 Å on a side. Periodic boundary conditions were applied in all three directions. Adsorption of alkanes on the interior, groove, and outside sites was studied. Real SWNT bundles will also have interstitial sites;[111] we have not considered these sites in this work, since we expect that the contribution due to interstitial adsorption to be negligible. We used an atom-explicit model for nanotubes, taking the Lennard-Jones parameters for graphite ($\sigma = 3.4$ Å, $\varepsilon = 28.0$ K) [112] for the nanotube carbons. We used the transferable potentials for phase equilibria (TraPPE)[113, 114] united atom model for alkane molecules. The alkane-alkane potential is divided into non-bonded, bond stretching, bond bending and torsion terms, given by the following equations

$$u(r_{ij}) = 4\varepsilon_{ij}\left[\left(\frac{\sigma_{ij}}{r_{ij}}\right)^{12} - \left(\frac{\sigma_{ij}}{r_{ij}}\right)^{6}\right] \tag{8.1}$$

$$u_{stretch} = \frac{1}{2}k_r\left(r - r_0\right)^2 \tag{8.2}$$

$$u_{bend} = \frac{1}{2}k_\theta\left(\theta - \theta_0\right)^2 \tag{8.3}$$

$$u_{tors} = c_0 + c_1\left[1 + \cos\phi\right] + c_2\left[1 - \cos(2\phi)\right] + c_3\left[1 + \cos(3\phi)\right] \tag{8.4}$$

We used standard Lorentz-Berthlot combining rules to calculate σ_{ij} and ε_{ij},

$$\sigma_{ij} = \frac{1}{2}\left(\sigma_{ii} + \sigma_{jj}\right) \tag{8.5}$$

$$\varepsilon_{ij} = \sqrt{\varepsilon_{ii}\varepsilon_{jj}} \tag{8.6}$$

The potential parameters used are given in Table 6 and Table 7. The TraPPE model defines a united atom segment as a single CH_3, CH_2, CH, or C group.

Table 6: Lennard-Jones Parameters for TraPPE-UA Field.

Pseudo-atom	ε/k_B [K]	σ [Å]
CH_4	148	3.73
CH_3	98	3.75
CH_2	46	3.95
CH	10	4.68
C	0.5	6.4

We have calculated the number of segments of molecules adsorbed on the inside, groove, and outside sites. A segment is identified as being inside a nanotube if its (x, y) coordinates lie within the radius of either of the natotubes (the area inside the solid circles representing the nanotubes in the Figure 42) and the z coordinate lies in the range covered by the extent of the nanotubes in the simulation box. The z axis coincides with the nanotube axis in our simulation cell. Segments are identified as being in the groove site if they lie within a cylinder of radius 2.90 Å centered in the nanotube groove sites (dashed circles in Figure 42). The center of the groove site cylinders are located a distance of 9.68 Å from the center of the nanotubes, on a vector directed 30^o above and below the plane containing the nanotubes (see Figure 42). A segment is identified as adsorbed on the exterior sites of the nanotubes if it lies within an annular region defined by the radii 6.78 and 11.88 Å from the nanotube centers, and if the segment is not within the groove sites. The outside adsorption sites are schematically shown as the gray shaded region in Figure 42. All other segments that do not lie within one of these three sites are identified as being in the multi-layer or the gas phase.

We have performed two types of simulations, namely NVT and modified grand canonical Monte Carlo simulations for various nanotubes/alkane systems. The NVT simulations were

Table 7: Bonded Parameters for the TraPPE-UA Force Field.

Stretch	$\mathbf{r}_0$ [**Å**]		$\mathbf{k}_r/\mathbf{k}_\mathrm{B}$ [**K**]	
CH_x-CH_y	1.54		130924.4893*	
Bend	θ_0		$\mathbf{k}_\theta/\mathbf{k}_\mathrm{B}$ [**K**]	
CH_x-(CH_2)-CH_y	114		62 500	
CH_x-(CH)-CH_y	112		62 500	
CH_x-(C)-CH_y	109.47		62 500	
Torsion	$\mathbf{c}_0/\mathbf{k}_\mathrm{B}$ [**K**]	$\mathbf{c}_1/\mathbf{k}_\mathrm{B}$ [**K**]	$\mathbf{c}_2/\mathbf{k}_\mathrm{B}$ [**K**]	$\mathbf{c}_3/\mathbf{k}_\mathrm{B}$ [**K**]
CH_x-(CH_2)-(CH_2)-CH_y	0	335.03	-68.19	791.32
CH_x-(CH_2)-(CH)-CH_y	-251.06	428.73	-111.85	441.27
CH_x-(CH_2)-(C)-CH_y	0	0	0	461.29
CH_x-(CH)-(CH)-CH_y	-251.06	428.73	-111.85	441.27

*This parameter is from OPLS-UA force field

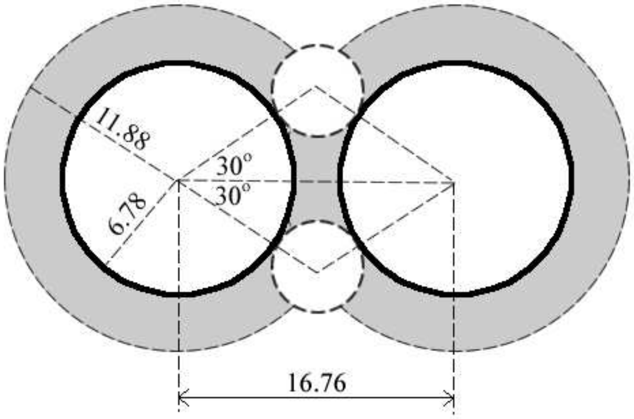

Figure 42: Interior, groove and exterior sites of a nanotube bundle. The unit in the figure is Å.

used to find the coverages of molecules in the different bundle sites for each of alkanes. The initial states for the NVT simulations were prepared by exposing the nanotube bundle to two liquid-like drops of alkane molecules, one at each end of the bundle. The molecules then occupied the interior, groove, external, multilayer sites, depending on the total number of molecules and the temperature. The liquid droplets were prepared from an isobaric-isothermal simulation of pure alkane molecules at 313.15 K and 60.0 MPa, where the starting configuration was a gas phase; the very high pressure was used to quickly reach a liquid-like density. The equilibration period was typically 200 000–400 000 HMC steps, where each step consisted of five MD long time steps followed by a HMC acceptance or rejection move. A typical value for the long time step in the MD run was around 15 fs. Five inner (short) time steps were taken for each long time step. The modified grand canonical ensemble simulations were designed to mimic the process of the TPD experiments and therefore we did not simulate a proper grand canonical ensemble. A typical TPD experiment is carried out by dosing a system with a known amount of alkane, followed by pumping the system to ultra high vacuum of around 10^{-8} Pa. The system is then heated and material desorbs into the vacuum; molecules that desorb are pumped away so fast that no readsorption can take place. We have mimicked this process by staring from a pentane-saturated nanotube bundle, obtained through the first type of simulation, followed by grand canonical-type moves to delete the pentane at a pressure of 10^{-4} Pa. No attempt to create molecules was made. Obviously, the equilibrium state for this type of simulation is a system with no adsorbed molecules. We are therefore not interested in the limiting distribution of this type of simulation. We use these modified grand conical simulations to probe, in an approximate way, the rate of desorption for pentane from each of the different sites on a SWNT bundle.

8.4 RESULTS AND DISCUSSION

As has been shown before,[103] alkane molecules can be adsorbed in four distinct environments on single wall carbon nanotubes, resulting in four resolved features in temperature desorption spectra. Figure 43 shows the representative temperature programmed desorption

(TPD) traces from three alkanes—n-pentane, n-nonane and 2,2,4-trimethylpentane (iso-octane).

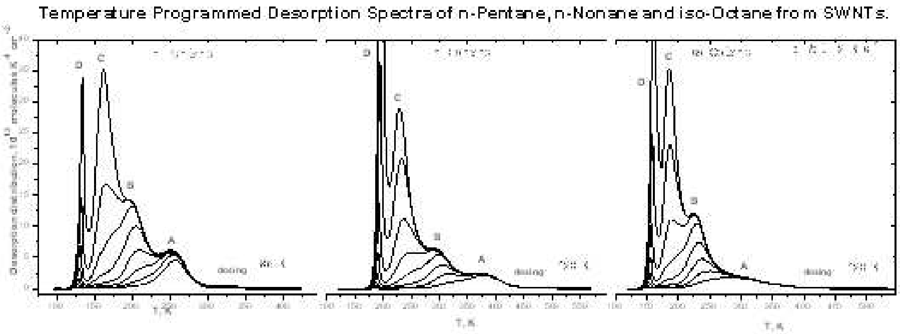

Figure 43: TPD spectra of n-pentane, n-nonane and iso-octane on SWNTs. Exposures are the same for all three compounds. They start at 2.16×10^{15} molecules cm^{-2} and increase by a factor of $2^{1/2}$.

The n-pentane and n-nonane spectra look qualitatively very similar, displaying four prominent features, labeled with letters A to D, that correspond to four different adsorption environments with certain adsorption energies and entropies. TPD spectra of other linear alkanes (n-hexane, n-heptane and n-octane, not shown) present similar spectra, with the difference being the position and relative intensities of the four peaks, as in the case of n-pentane and n-nonane.

Peak D can be easily identified. The overlapping leading edges of the D features in these spectra facilitate their assignment as the multilayer peaks. They result from the desorption of bulk-like adsorbate that forms on the SWNTs at high exposures to the hydrocarbon molecules and are not characteristic of nanotube adsorption sites. At the same time, none of the A, B or C features are present on the blank gold reference, meaning that these features originate from the adsorbate bound on the nanotubes. Thus, in the following we will limit our discussion to the A, B and C desorption features.

It can be seen that for all three adsorbates features A and B are saturated at the highest exposures shown in Figure 43, while features C and D continue to grow. Consequently, this exposure range should allow the determination of the capacities for sites A and B.

Based on the A process occurring at the highest temperature, as well as relative capacities of sites A and B toward molecules with different molecular lengths, we assign site A as nanotube interior and site B as the grooves on the outside of SWNT bundles. Such assignment is confirmed by molecular simulations carried out on model SWNT-alkane systems. Here we summarize the findings leading to this assignment.

We have shown earlier[103] that in the case of a rather dissimilar molecule, CCl_4, the same three desorption peaks are observed. Displacement experiments involving simultaneous adsorption of CCl_4 and n-nonane showed that the features A and B, and possibly C, correspond to the same adsorption sites on nanotubes in the case of these two molecules. As the alkanes, which are the focus of the current study, must be much more similar to each other in their adsorptive properties than n-nonane and CCl_4, it can be concluded with a very high degree of certainty that different alkanes occupy the same three adsorption sites on the SWNT surface, and that desorption processes A, B and C are sampling the same sites for different hydrocarbons.

Due to the use of the normalization procedure described in the experimental section, the areas under individual features reflect the amount of adsorbate found on that site, and additionally, the areas under the TPD features can be compared directly for different molecules. Thus, in order to estimate the amount of adsorbate molecules on adsorption sites A and B, the areas under these two peaks must be found. This task presents challenges, as a significant overlap of different peaks prohibits straightforward integration. Modeling of the spectra as a sum of first order desorption peaks is also problematic due to apparent repulsive adsorbate-adsorbate interactions. In Figure 43, these interactions manifest themselves in the shift of peak maxima to lower temperatures as the adsorbate coverage increases.

In order to circumvent this difficulty in measuring the areas of A and B, we conducted a series of experiments where the dosing temperature of the alkanes was varied around the onset temperature of the two peaks instead of dosing at a low temperature where all molecules would be adsorbed either on nanotubes or into a multilayer. Such a procedure effectively prevents the adsorption on surface sites that desorb the adsorbate around of below the temperature of dosing. In these experiments the exposure was chosen to be large enough so that a stationary state on the surface was reached and no further accumulation of the molecules on SWNTs occurred.

Modified grand canonical simulations for the pentane/nanotube system were carried out at various temperatures, from 125 K to 350 K. The starting state was achieved from the HMC simulations of nanotube/pentane system at 125 K. Although the modified grand canonical simulations do not have a real time scale, the relationship between the number of pentane molecules deleted from the system for a fixed number of MC steps and temperature is related to the desorption rates deduced from TPD experiments. Both the experiments and simulations are driven by entropic and energetic considerations. Therefore, we believe the simulations provide information that can be useful for comparing with the TPD experiments. The relative changes in coverage on each of the three sites as a function of temperature are plotted in Figure 44. The coverages are plotted for a fixed number of MC steps and are

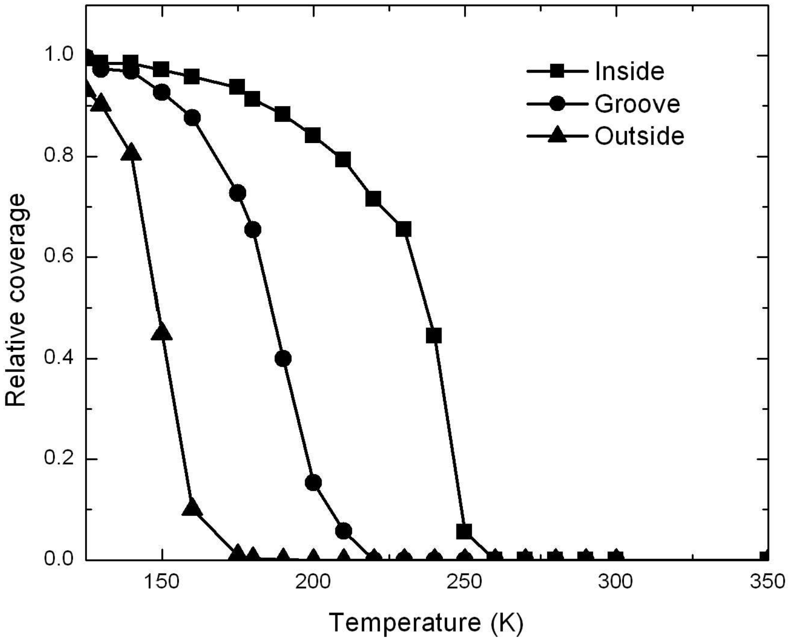

Figure 44: Simulated TPD-like spectra (pseudodesorption rates) computed from molecular modeling for n-pentane.

normalized by the initial number of molecules on each of the sites. From Figure 44 we see that n-pentane molecules on the exterior sites desorb more readily than molecules on the groove and interior sites. This is true for all temperatures. Moreover, n-pentane is completely depleted on the external sites at the lowest temperature (∼175 K), the groove site is depleted at the next lowest temperature (∼220 K) and the internal sites are depleted at the highest temperature (∼270 K). These temperature trends are in qualitative agreement with the TPD data and corroborate that peak A corresponds to the internal sites, peak B to the groove sites, and peak C to the external sites of the nanotube bundles. Derivatives of the curves in Figure 44 would lead to TPD-like plots from the simulations. However, statistical noise in the data do not justify taking the derivatives.

The choice of the step number of 5000 is arbitrary. We have also examined the simulations at 1500 and 10000 steps. The lines shift to the right at 1500 steps and to the left at 10000 steps. However, both cases have the same general shape as seen in Figure 44 and have the same trends for the three sites.

Figure 45 demonstrates the n-pentane TPD spectra that result from 5 exposures near the onset temperature of the A peak and 5 exposures near the onset temperature of the B peak. The difference between two consecutive dosing temperatures within each set of five TPD spectra is 5 K. It can be seen that as the dosing temperature decreases, the A peak initially grows but the rate of growth slows down with each exposure and eventually a shoulder of the B peak starts to develops on the low temperature side of A. We take the area of the TPD trace No.3, where the rate of growth of A is suddenly slowed down and no B shoulder is visible, to be the area of the A peak. This method of removing the overlapping TPD intensity should correctly identify the initial coverage when the peak in question is saturated. The main error in such an estimate comes from the inability to exactly identify the dosing temperature when the peak being saturated stops growing.

A similar analysis can be conducted for site B. For n-pentane TPD spectra in Figure 45, spectrum No. 8 is then the sum of features A and B. The area of B can thus be found by subtraction.

In only the case of iso-octane, peak A splits into several broad features and starts to overlap more significantly with feature B. Due to this fact the area of the A peak could

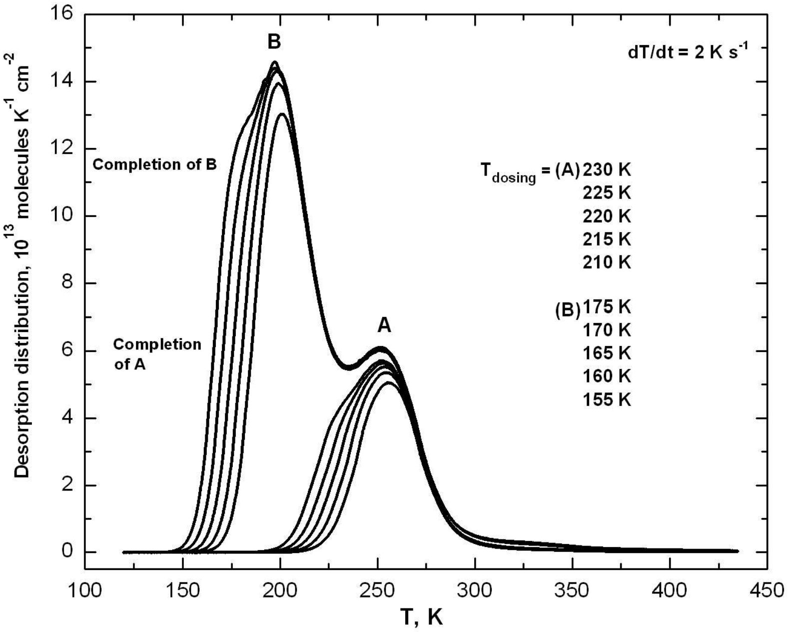

Figure 45: Finding the capacity of adsorption sites A and B by varying the dosing temperature in the TPD experiments. n-Pentane is given as an example of the procedure that was also used for other alkanes in the study.

not be determined with the varying dosing temperature method. Figure 46 shows the TPD spectrum of iso-octane on SWNTs at a dosing temperature where it was found by the method described above that the peaks A and B are both saturated.

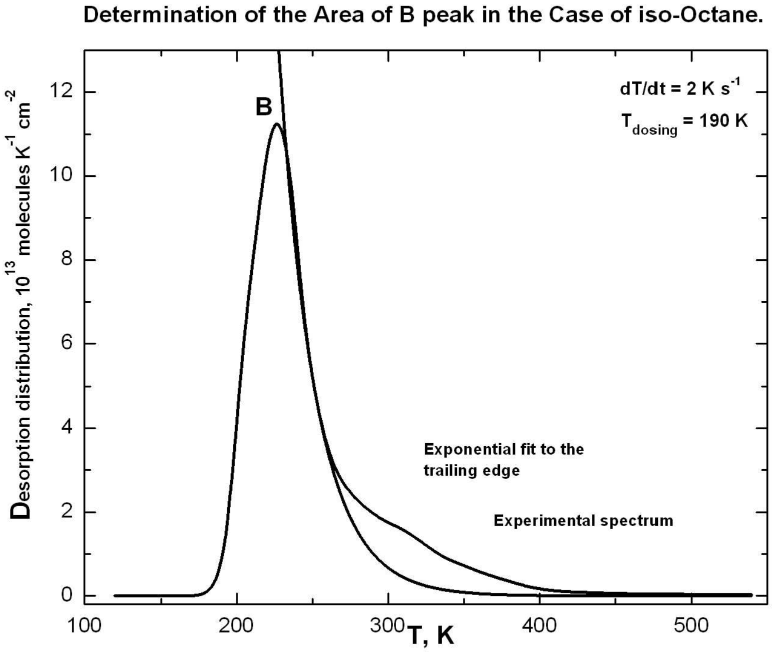

Figure 46: Finding the area of peka B in the case of iso-octane. Extensive overlap of A and B can be seen. The trailing edge of B was fitted to a decaying exponential and all TPD intensity above the fit was assumed to belong to feature A.

We estimated the area of A and B for iso-octane by fitting a decaying exponential to the trailing edge of the B peak where the overlap with A is expected to be small. It appears likely that the area of B found this way contains a contribution from A, meaning that the area of B is overestimated and the area of A is underestimated. The resulting relative error in the case of B is not particularly large because of the large total value of B, but should be quite significant in the case of A. For this reason we do not include the area of A for iso-octane in our further analysis.

Figure 47 summarizes the capacities of site B toward linear alkanes and iso-octane. For convenience it is represented not as a capacity plot but rather as an inverse capacity, representing the relative space occupied by a molecule on site B. The space occupied in the B site by an n-pentane molecule is taken to be 1. The error bars in Figure 47 represent the relative the values that correspond to choosing two neighboring spectra in plots analogous to those in Figure 45. It is likely that the errors are less than those given by the error bars.

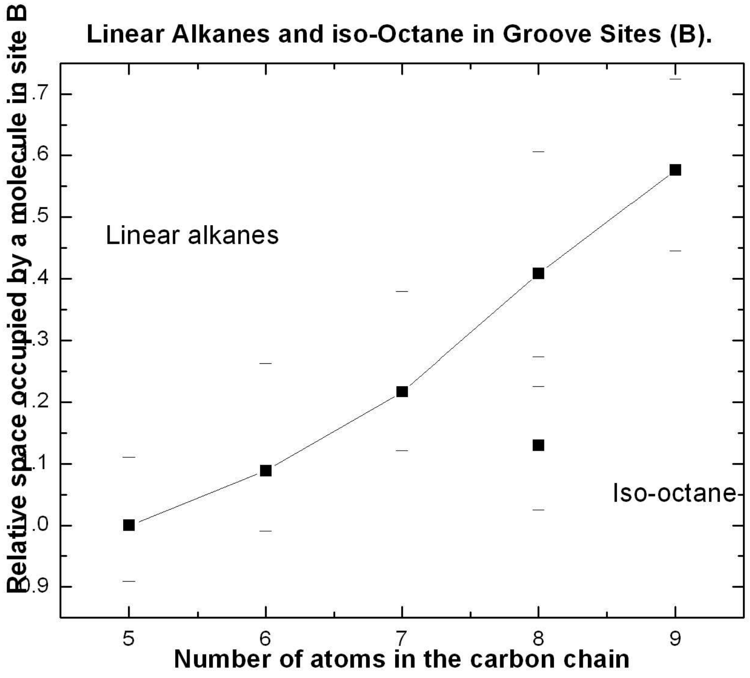

Figure 47: Relative amounts of space occupied in the groove sites, B, by five linear alkanes and a branched iso-octane.

It is evident that an approximately linear relationship is observed for n-alkanes from C_5-C_9, while the iso-octane point clearly does not follow the trend expected for a C_8 molecule. An iso-octane molecule occupies approximately as much space on site B as a hexane molecule, in accordance with its shorter carbon skeleton.

The linearity of the plot shown in figure 47 and the lack of fit of iso-octane at the C_8 position can be logically explained if site B is a one-dimensional adsorption site, where the length of the molecule determines the site's capacity toward the molecule. A natural choice for such a one dimensional site is the groove site between individual nanotubes in the bundle.

An iso-octane molecule is significantly shorter than an octane molecule due to three branchings along the chain. Its main carbon chain is 5 atoms long, and this causes it to occupy less space in the groove site than a normal octane molecule. Ideally it should occupy as much space as an n-pentane molecule, but it should be expected that the bulky end groups of iso-alkane will somewhat increase its effective length.

We also performed simulations to investigate relationship between the capacities of the groove and interior sites of the nanotube bundle and the number of carbon atoms of the alkanes. These simulations are the first type of simulation, which we mentioned in the theoretical section. During the simulations, we count the number of segments on the interior sites and groove sites of the nanotube bundle. The number of molecules is calculated by taking the number of segments divided by the number of carbon atoms of the alkane molecule. The reciprocal of number of molecules is related to the capacities of these bundle sites. The relationship between the relative capacities of the groove site and number of carbon atoms of an alkane is shown in figure 48.

The triangle point in the figure 48 is iso-octane. The calculation for number of molecules of iso-octane is different from other normal alkane. Although iso-octane has eight carbon atoms, we divide the number of segments by five instead of eight. This is because iso-octane is a branched molecule, which has a five-carbon backbone chain. With our definition of groove sites, the branched parts of an iso-octane molecule are not counted as in groove sites, if the molecule lies along the groove sites. Because the branch parts are too far from the groove sites while the backbone part lies along the groove sites. Therefore, we believe five is a more proper value to use as a number of effective chain length. Figure 49 shows the adsorption of both n-octane and iso-octane on the groove site. We can clearly see that an iso-octane molecule does occupy less space along the groove site than an n-octane molecule.

We can have two conclusions from Figure 48. The first is that the capacity of groove sites has an inverse linear relationship with carbon number for n-alkanes. This is easy to understand since larger molecules have larger molar volume. The second is the deviation from the linear relationship of iso-octane. The space occupied by an iso-octane is less than

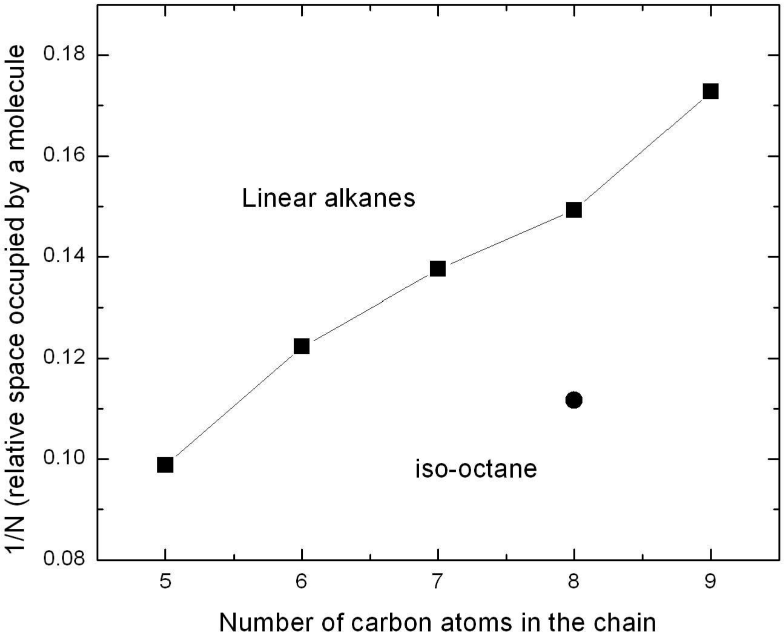

Figure 48: Relative space occupied in the groove sites for alkanes.

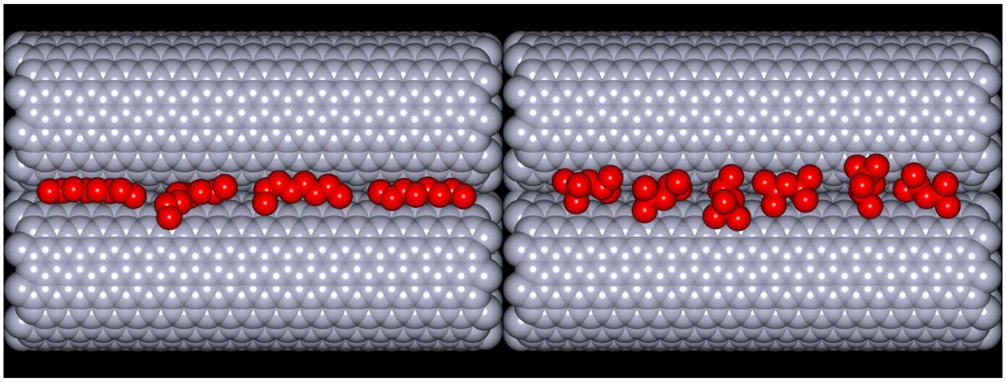

Figure 49: Simulation snapshots of n-octane and 2,2,4-trimethylpentane adsorbed on the groove site.

that of an n-octane molecule and close to an n-hexane. However, the deviation is expected, because the length of iso-octane's main chain is five instead of eight and the groove site packing is a pseudo-one-dimensional configuration, as we can see from figure 49. These two findings are also consistent with the experiment results.

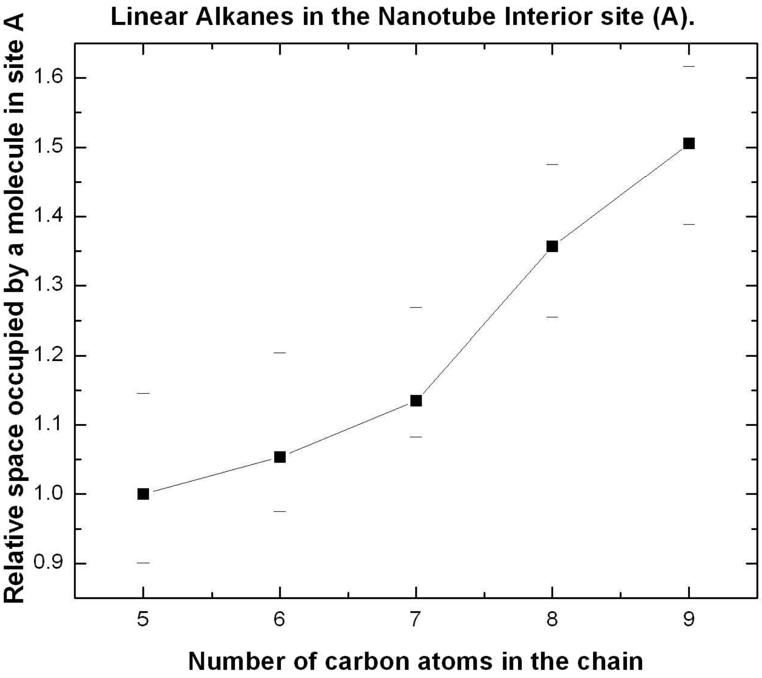

Figure 50: Relative occupation of space by alkane molecules in the interior of the nanotubes.

A similar plot can be made for the occupancy of the A, as shown in Figure 50. We assign peak A as the desorption from the interior of the nanotube for the two following reasons. Firstly, the simulations confirm that the nanotube interior must have a higher binding energy compared to the groove sites. And secondly, our previous experiments with coadsorption of N_2 and n-nonane as well as CCl_4 and n-nonane formed the basis for assigning this adsorption site as the nanotube interior. Simulations were also performed to find the relationship between the relative capacities of the interior site and number of carbon atoms of an alkane, shown in figure 51.

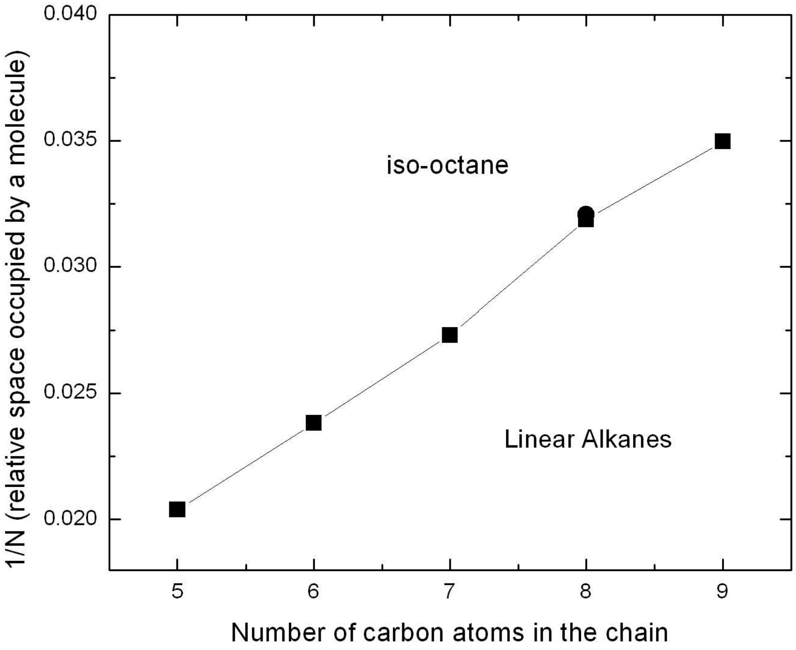

Figure 51: Relative space occupied in the interior sites for alkanes.

The triangle point in the figure 48 is iso-octane. Similar to Figure 48, we also found the inverse linear relationship between the capacity of the interior site and the number of carbon atoms. In addition, iso-octane also lies on the same line and overlaps with *n*-octane, which is different from the case of groove site. This is because the interior sites of the nanotubes are three-dimensional. The effects of the backbone chain length are much smaller in a three-dimensional packing. Each segment in a molecule occupies almost the same space. Therefore an *n*-octane molecule and an iso-octane molecule occupy roughly the same amount of space inside a nanotube.

8.5 CONCLUSION

We were able to make the following conclusions as a result of this investigation:

1. Three distinct adsorption sites are observed on single wall carbon nanotubes by alkane adsorption.
2. On the basis of molecular simulations and earlier displacement experiments, the highest binding energy adsorption site (site A) corresponds to adsorption inside nanotubes.
3. The second highest binding energy site (site B) corresponds to groove sites between adjacent nanotubes in bundles.
4. In the grooves the adsorbed molecules are packed in a one-dimensional manner. The length of the molecule determines the capacity of the groove site toward it.
5. Simulations found different desorption rates for the interior, groove and exterior sites of a nanotube bundle.
6. Simulations found the linear relationship between the space occupied by a linear molecule and its carbon atom number, both on groove and interior site.
7. Iso-octane behaves differently from other *n*-alkane in the relative occupied space. Simulations found the reason is that the effective chain length of the iso-octane is not equal to its carbon atom number.

9.0 N-HEPTANE DIFFUSION ON CARBON NANOTUBES

9.1 INTRODUCTION

This chapter is taken from a paper in preparation, "Inter- and Intra-tube Self-diffusion in n-Heptane Adsorbed on Carbon Nanotubes".[115] The experimental work was done by Dr. Petro Kondratyuk. The Monte Carlo simulations were done by Dr. Jinchen Liu. The author did all of the molecular dynamics simulations.

From a practical standpoint, the transport properties of adsorbed molecules play an important role in determining the applicability of single wall carbon nanotubes (SWNTs) as adsorbents, as they control the rates of molecular uptake and release. While a number of studies have focused on molecular transport along the nanotube channels,[116, 117, 118, 119, 120, 121] few[122] have addressed the diffusion dynamics of the molecules in the bulk of the nanotube samples and none investigated the self-diffusion of the adsorbates in the SWNT bulk. On the other hand, self-diffusion in such well-studied media as zeolites has received a significant amount of attention.[123, 124, 125, 126, 127, 128, 129, 130, 131, 132, 133]

Here we study experimentally the self-diffusion of n-heptane through a bulk SWNT sample. We compare the results to a molecular dynamics (MD) simulation of n-heptane diffusion inside an individual nanotube under the conditions of full n-heptane loading. Heptane was chosen due to the earlier findings that normal alkanes allow the different adsorption sites to be resolved by temperature programmed desorption (TPD).[84] The temperature in the experiment was chosen such that only the interior adsorption sites could be populated while other types of sites remained unoccupied.[84]

Several techniques have been used to determine the self-diffusion coefficients of adsorbed molecules in microporous solids, among them field-gradient NMR,[123, 126, 127, 129, 132] inelastic neutron scattering[133] and the use of isotopically labeled molecules.[130, 131] The latter is employed here. It is based on the displacement of the adsorbed molecules by isotopically labeled but otherwise identical molecules. The slower the diffusion, the more slowly will the displacement occur because of the accumulation the labeled molecules in the outer layers of the microporous solid.

The SWNTs are a nanostructured material, and consequently, at the nanoscale the propagation of molecules does not obey the normal Gaussian law. This effect is well known for zeolites.[123, 124, 125] In particular, a molecule confined inside a zeolite cavity may experience rapid diffusion within the confining boundaries while hopping between different cavities may be very rare. The case of *n*-heptane on SWNTs is highly analogous. Under our experimental conditions the molecules were adsorbed only inside nanotubes. Thus two transport regimes were present, inside individual nanotubes and between different nanotubes. The experimentally measured diffusion coefficient corresponds to long-range transport and, consequently, diffusion between different nanotubes. This diffusion was found to be vastly slower than the diffusion inside individual nanotubes seen in the MD simulation.

Various groups have simulated the diffusion of molecules adsorbed in SWNTs.[116, 119, 134, 135, 136, 137, 138, 139, 140] Previous simulation studies have shown that transport of small molecules can be much more rapid inside SWNTs than in other nanoporous materials.[134, 141, 142, 143] The transport of alkanes inside SWNTs has also been noted to be rapid.[137, 138, 140]

9.2 EXPERIMENTAL

9.2.1 System and Materials

The experiments were performed in a stainless steel ultrahigh vacuum (UHV) system with a base pressure of 2×10^{-10} Torr after bakeout. The system is pumped by a 150 L/s turbomolecular pump and a 360 L/s ion pump.

The SWNTs were produced by R. Smalley and coauthors by pulsed laser vaporization of graphite impregnated with a Ni-Co catalyst.[100, 101] Removal of catalyst particles and graphitic impurities was accomplished by treating the nanotube material in an aqueous solution of H_2SO_4 and H_2O_2.[102] Such treatment is known to cause the cutting and opening of the SWNTs making the interior sites available for adsorption. The average diameter and length of the nanotubes in the sample was 13.6 Å and 320 nm respectively.

The nanotubes were deposited in air onto a gold support plate measuring 10×14 mm from a 12 mg/L suspension in dimethyl formamide. The solvent was allowed to evaporate, leaving a nanotube deposit of $\sim$36 μg. On the basis of the approximate density of compressed SWNTs of 1 g/mL,[144] we calculate that the thickness of the deposit was $\sim$0.25 μm.

The support plate was attached to the sample holder via two tungsten wires. By passing current through the wires the sample could be heated up to 1100 K. The wires also provided thermal contact with a liquid-nitrogen filled cold finger, which allowed cooling to 89 K. Temperature was monitored with a type K thermocouple attached to the gold plate.

Dosing of *n*-heptane and *n*-heptane-d_1 was accomplished with two calibrated pinhole conductance dosers.[105, 106] More details on the experimental setup are available elsewhere.[145] *n*-Heptane was purchased from commercial sources and purified by two freeze-pump-thaw cycles. *n*-Heptane-d_1 was synthesized from 1-iodoheptane and $LiAlD_4$ and had a measured purity of 99%. Freeze-pump-thaw purification was also performed.

9.2.2 Experimental procedures

The displacement experiment involved first exposing the sample to a large amount of *n*-heptane at 275 K. This exposure was large enough to completely saturate all available interior sites. We earlier showed that other types of sites remain unoccupied at this temperature.[84]

Following the exposure to *n*-heptane the sample was immediately rotated to a second doser producing a required flux of *n*-heptane-d_1. As there are no unoccupied sites remaining on the surface that could be filled at this temperature, an *n*-heptane-d_1 molecule could only adsorb on the surface if it displaced an *n*-heptane molecule. The gradual displacement of *n*-heptane was then allowed to occur for a required period of time after which the sample was rotated away from the *n*-heptane-d_1 doser. and its temperature was immediately dropped to avoid any desorption from the surface.

The two molecular dosers were operating continuously during the experiments in order to minimize the delay between exposures to n-heptane and n-heptane-d$_1$. However when the sample was not directly in front of the doser, it only intercepted a small fraction of the incoming flux (~3%) due to the very fast pumping of n-heptane by the cold parts of the sample holder at 77 K.

After the exposure to n-heptane and n-heptane-d$_1$ the sample was positioned in front of a 3 mm diameter aperture of a shielded quadrupole mass spectrometer (QMS). The temperature was then linearly increased at a rate of 2 K s^{-1} and signal of the QMS caused by the desorbing molecules was recorded simultaneously at m/e = 100 (almost exclusively due to n-heptane) and 101 (mostly n-heptane-d$_1$, some contribution from n-heptane if it is present in the desorbing flux). QMS shied was biased to -100 V to prevent the electrons from the QMS ionization chamber from impacting the sample.

A linear transformation of the TPD spectra at these two masses produces the TPD spectra of desorbing n-heptane and n-heptane-d$_1$. The relevant ratios of intensities that determine such transformation were found to be $I_D^{101}/I_D^{100} = 50.8$ (not infinite due to a small percentage of n-heptane in n-heptane-d$_1$) and $I_H^{100}/I_H^{101} = 12.7$, where H and D subscripts denote intensities for n-heptane and n-heptane-d$_1$ respectively.

Integration of the TPD spectra for n-heptane and n-heptane-d$_1$ gives the absolute amount of each molecule present on the surface at the time of the TPD measurement. These values were used for further analysis.

It was found that because both n-heptane and n-heptane-d$_1$ dosers were on during exposure to either gas, the sample saw some small amount of exposure to the molecules from the doser in front of which it was *not* positioned. For instance, in one of the experiments it was found the sample was exposed to 96.6% of n-heptane and 3.4% of n-heptane-d$_1$ ("H mixture") when it was positioned in front of the n-heptane doser, and 94.7% of n-heptane-d$_1$ and 5.3% of n-heptane ("D mixture") when in front of the n-heptane-d$_1$ doser. Thus it is not the displacement of n-heptane by n-heptane-d$_1$ that occurs in this experiment, but rather the displacement of "H mixture" by "D mixture". Because of the linearity of the diffusion equations, the displacement kinetics of both processes are identical. All that needs to be done to correct for the non-100% composition is to convert the amounts of n-heptane and *n*-heptane-d_1 into the amounts of the appropriate "H" and "D" mixtures. Such correction was always made for the displacement data presented here and the results are given for simplicity as the displacement of *n*-heptane by *n*-heptane-d_1.

During the displacement experiments, a drift in the sensitivity of the QMS was seen over the course of hours and days. In order to correct for this slow drift, the sum of the amounts of *n*-heptane and *n*-heptane-d_1 was normalized to 2070×10^{12} molecules cm^{-2}, the capacity of the sample from a calibrated measurement. The changes in the QMS detector sensitivity were the dominant source of noise in these measurements.

The interpretation of the results in terms of self-diffusion is based on the premise that the system cannot distinguish between the two molecules, in other words, all the thermodynamic properties for the adsorption of *n*-heptane and *n*-heptane must be identical. We tested this hypothesis by TPD and could not observe any measurable differences in the desorption behavior of the two molecules.

All the measurements presented here were performed using a semiautomatic system described earlier.[145] Short delays between the dosing operations and the TPD spectra acquisition helped ensure that the sample is exposed to the background flux of the adsorbates as little as possible.

Before each series of experiments the nanotube sample was annealed at 1073 K for 10 minutes to decompose the traces of oxygen functionalities that might be present on the nanotubes. Such functionalities are known to block entry into the interior of the nanotubes.[93]

9.2.3 Simulation Methods

We have used molecular dynamics (MD) to study the diffusion and mobility of *n*-heptane molecules in both the bulk and adsorbed phases. The intra-molecular degrees of freedom were integrated using the multiple-time-step reversible reference system propagation algorithm.[110] The value of the long time step was 5 fs. Each long time step consisted of five inner (short) time steps. We used the transferable potentials for phase equilibria (TraPPE)[113] united atom model for *n*-heptane molecules, in which the CH_3 and CH_2 groups are defined as single united atom segments. The total potential is a sum over four types of potentials, namely: non-bonded, bond stretching, bond bending, and dihedral torsion. Equations 8.1 to 8.2 give the functional form for each type of potential. Standard Lorentz-Berthlot combining rules were applied to calculate the cross terms, σ_{ij} and ε_{ij} using Equations 8.5 and 8.6. Potentials parameters used in the equations are shown in Tables 6 and 7.

Equilibrium molecular dynamics (EMD)[146, 147] was used to calculate the n-heptane diffusion coefficients for both bulk and nanotube confined n-heptane molecules. We used the Nosé-Hoover thermostat[148] to correctly sample the canonical (constant temperature) ensemble. The bulk n-heptane phase consisted of 100 heptane molecules at a density of 0.7 g/ml. The nanotube system used to compute the self-diffusion coefficient of n-heptane within a SWNT consisted of a single (10, 10) nanotube, 295.14 **Å** (120 unit cells) long. The nanotube contained 93 heptane molecules; this loading corresponds to a bulk phase pressure of 1.5×10^{-3} Torr. The density of heptane inside the SWNTs is not well defined, because it depends on how one calculates the volume of the nanotube. If we just take the nanotube radius and length to calculate the volume (πr^{2}l) of the nanotube, the density we get is 0.36 g/ml, which is rather low for a liquid like phase. However, if we include the volume of the carbon atoms on the nanotube (through their van der Waals radius) and calculate the nanotube volume as the accessible volume (π(r-σ/2)^{2}l), the density of the heptane increases to 0.65 g/ml, which is close to the bulk liquid density. The system was periodic in the z-direction (along the nanotube axis). The self-diffusivity measures the mobility of a single tagged molecule moving through the system. The self-diffusion coefficient can be calculated from molecular simulations by using the Einstein relation.[149]

$$D_s(c) = \lim_{t\to\infty} \frac{1}{2dNt} \left\langle \sum_{i=1}^{N} \left|\vec{r}_i(t) - \vec{r}_i(0)\right|^2 \right\rangle \quad , \tag{9.1}$$

where c is the concentration of the molecules, d is the dimensionality of the system, N is the number of the molecules, t is the simulation time, and $\vec{r}_i$ is the vector of the center of mass of the ith molecule. For bulk phase systems, $2d= 6$. For molecules adsorbed inside a nanotube, diffusion occurs only in one dimension (along the nanotube axis) in the limit of long time, so $2d= 2$. In addition, we consider only the displacement along the axis of the nanotube so that $\vec{r}_i$ is replaced by z_i in eq 9.1.

We have used non-equilibrium molecular dynamics to model the kinetics of n-heptane entering the nanotube from an initial state adsorbed on the external surface of the nanotube bundle. This mimics the initial experimental process of dosing the nanotube bundle with alkanes at a fixed temperature. We assume that molecules initially adsorb on the external surface of the nanotube bundle and then diffuse to the interior. We also assume that evaporation from the surface of the nanotube bundle occurs in competition to entry into the nanotube interior. We have monitored the evaporation and entry rates of n-heptane molecules on the surface of a simple nanotube bundle. The nanotube bundle consisted of two (10, 10) SWNTs, each with a length of 49.19 Å (20 unit cells). A schematic of the bundle is shown in Figure 42. The two nanotubes were placed parallel to each other with a gap between the walls of the adjacent tubes of 3.2 Å. This is the smallest possible "bundle" and was chosen for computational efficiency, while still retaining the essential features of a bundle, having groove, internal, and external surface sites. We assume that adsorption in interstitial sites[111] to be negligible and hence our model bundle does not include an interstice. A series of simulations were performed for this nanotube bundle system with different initial n-heptane coverages. The number of n-heptane molecules evaporating from the bundle and entering the nanotube internal sites were recorded during the simulations. A united atom segment is defined as being inside a nanotube if its (x,y) coordinates lie within the radius of either of the nanotubes (the area inside the solid circles representing the nanotubes in Figure 42) and the z coordinate lies in the range covered by the extent of the nanotubes. Segments are identified as being in the groove site if they lie within a cylinder of radius 2.90 Å centered in the nanotube groove sites (dashed circles in Figure 42). The center of the groove site cylinders are located a distance of 9.68 Å from the center of the nanotubes, on a vector directed 30^o above and below the plane containing the nanotubes (see Figure 42). A segment is identified as adsorbed on the exterior surface sites of the nanotubes if it lies within an annular region defined by the radii 6.78 and 11.88 Å from the nanotube centers, and if the segment is not within the groove sites. The outside adsorption sites are schematically shown as the gray shaded region in Figure 42. All other segments that do not lie within one of these three regions are identified as being in the multi-layer or the gas phase. A segment is identified as in the gas phase site if all of its segments are at least ∼15 Å away from either of the two nanotube center axes; this value was chosen to allow for the possibility of two adsorbed layers of alkanes on the external surface of the nanotube. Evaporation is defined as all the segments of a n-heptane molecule leaving from either nanotube internal, groove, or exterior surface sites into gas phase. We count molecules as having entered the nanotube when at least five segments of a n-heptane molecule moves into the range of nanotube internal sites.

Nanotubes in our simulations are atom explicit and are held rigid. The Lennard-Jones parameters used for the carbon atoms in the nanotube were taken to be those for graphite (σ = 3.4 Å, ε = 28.0 K).[112] The MD simulations described above were carried out with fixed number of molecules in the simulation cell. The pressure of n-heptane in the bulk phase in equilibrium with the n-heptane adsorbed on the nanotubes is unknown in the MD simulations. We have therefore carried out a series of grand canonical Monte Carlo (GCMC) simulations[149] to find the equilibrium loading of n-heptane on the external and internal sites of a model SWNT bundle as a function of the gas phase pressure. We used the Towhee simulation package,[150, 114] which is an implementation of the continuum configurational bias method,[151] in our calculations. The chemical potential, rather than the pressure, is specified in GCMC simulations. We therefore performed additional bulk phase simulations to relate the chemical potentials to the bulk phase pressures.

Simulations for adsorption of n-heptane on the external surface of a nanotube bundle used two parallel SWNTs, separated by 3.4 Å. Each nanotube had a length of 49.19 Å (20 unit cells). The bundle was placed in the center of a cubic simulation cell, 100 Å on a side. Molecules were not allowed to adsorb in the interior of the SWNTs in this case. Adsorption inside a SWNT was modeled by using an array of SWNTs and allowing adsorption only inside the nanotubes. A total of $6{\times}10^6$ configurations were used, with each configuration consisting of an attempted move, where a move is one of the following: insertion, deletion, translation, rotation, or molecule regrowth. The type of move was chosen with equal probability.

9.3 RESULTS AND DISCUSSION

9.3.1 Efficient adsorption into internal sites

We have reported earlier that linear alkanes afford an unexpected resolution of adsorption sites on SWNTs.[84] Figure 52 contains TPD spectra of n-heptane showing peaks for internal sites, groove sites on the outside of the bundles, and exterior sites according to our previous assignment.

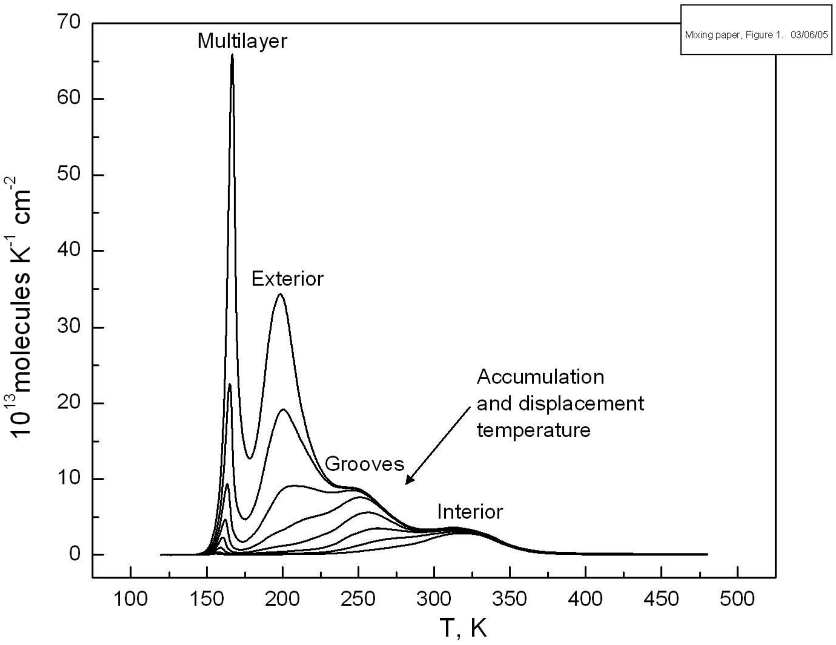

Figure 52: n-Heptane TPD spectra showing resolved peaks for interior, groove and exterior SWNT adsorption sites. The temperature used in the displacement experiment only allows the interior sites to be populated.

The sites identified as interior have the highest adsorption energy. For the self-diffusion experiments described here we chose the temperature such that only the interior nanotube sites could be populated.

The first step in measuring the diffusion coefficient is filling the nanotube interior with the unlabeled molecule, n-heptane. The approach to equilibrium surface coverage versus the exposure to n-heptane is illustrated in Figure 53. The curve saturates at exposure of approx. 5000×10^{12} molecules cm^{-2}. The saturation exposure used in further experiments was chosen to be slightly higher, 5800×10^{12} molecules cm^{-2}, to guarantee that all interior sites were filled.

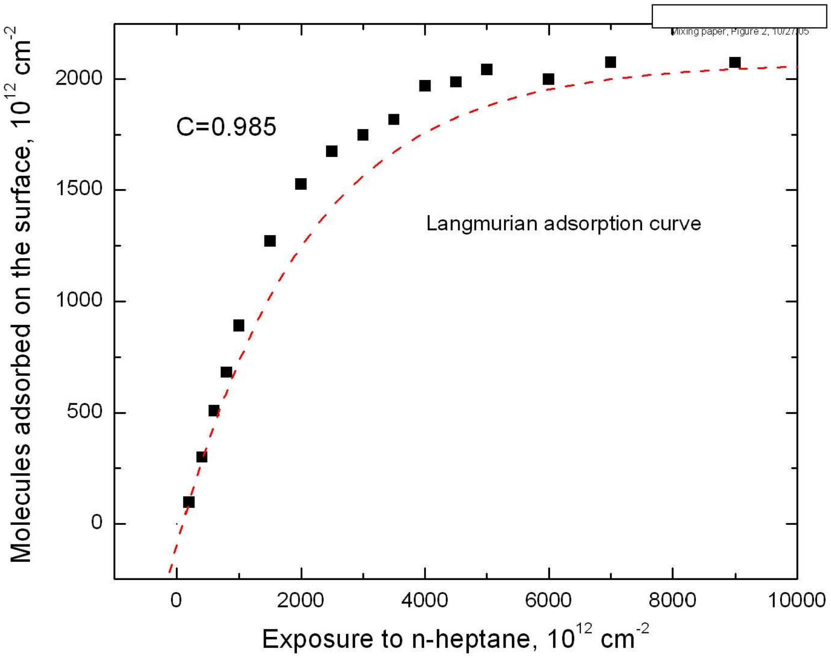

Figure 53: Approach to equilibrium surface coverage with increasing exposure to n-heptane at 275 K. The initial sticking coefficient is very close to unity. The solid line is the linear fit to the initial data points, the dashed line is the Langmuir-type approach to saturation.

The initial sticking coefficient, C, is very close to 1 as measured by the initial slope of the saturation curve. This value of the sticking coefficient is relative to the sticking coefficient at 110 K, which was assumed to be exactly unity. Such an assumption was needed to set the scale on the y-axis in Figure 53 in a calibration experiment where a known exposure of n-heptane was dosed onto the nanotubes at 110 K. This calibration experiment eliminates the unknown sensitivity of the mass spectrometer toward the *n*-heptane. There is sufficient evidence that below the multilayer desorption temperature the sticking coefficients of alkanes are essentially unity.[152]

The unity sticking coefficient seen here can be rationalized in the following way. Even though the groove sites cannot retain *n*-heptane at 275 K over a long period of time (see Figure 52), the residence time of *n*-heptane there is still more than sufficient to allow the molecules to migrate and find the more strongly-binding internal sites. We estimate this residence time at 0.4 s from the groove site peak temperature (252 K) assuming the first-order desorption model and a preexponential factor of 10^{12} Hz. Thus the incoming *n*-heptane molecules first adsorb in the grove sites before migrating to the interior sites that are inaccessible directly from the gas phase. Pre-adsorption migration stage in the grooves helps explain both the unity sticking coefficient and the fact that the adsorption proceeds faster than dictated by the Langmurian localized adsorption kinetics (solid line in Figure 53), where probability of adsorption for the incoming molecule is (1-θ).

9.3.2 Self-diffusion through the 0.25 μm sample

Once the saturation coverage has been reached, further addition of *n*-heptane (or *n*-heptane-d_1) causes the displacement of previously adsorbed molecules. A typical result of an experiment where *n*-heptane is displaced with *n*-heptane-$d_1$is shown in Figure 54. If the diffusion were infinitely fast, the displacement would follow the perfectly stirred reactor (PSR) model and the concentration of *n*-heptane would decay exponentially with exposure to *n*-heptane-d_1. However, finite rate of diffusion causes the *n*-heptane-d_1 to accumulate in the outer layers of the sample and the displacement proceeds more slowly because more incoming *n*-heptane-d_1 molecules displace molecules of the same type, *n*-heptane-d_1.

Increasing the delivery rate of *n*-heptane-d_1 makes the displacement less efficient per unit exposure as less time is available for the concentrations to equilibrate throughout the sample. Figure 55 provides experimental results that illustrate this point. Here, a more convenient semilogarithmic format is adopted. The y axis is the natural logarithm of the fraction of the total capacity occupied by *n*-heptane. The x axis is the exposure to *n*-heptane-d_1 in units of

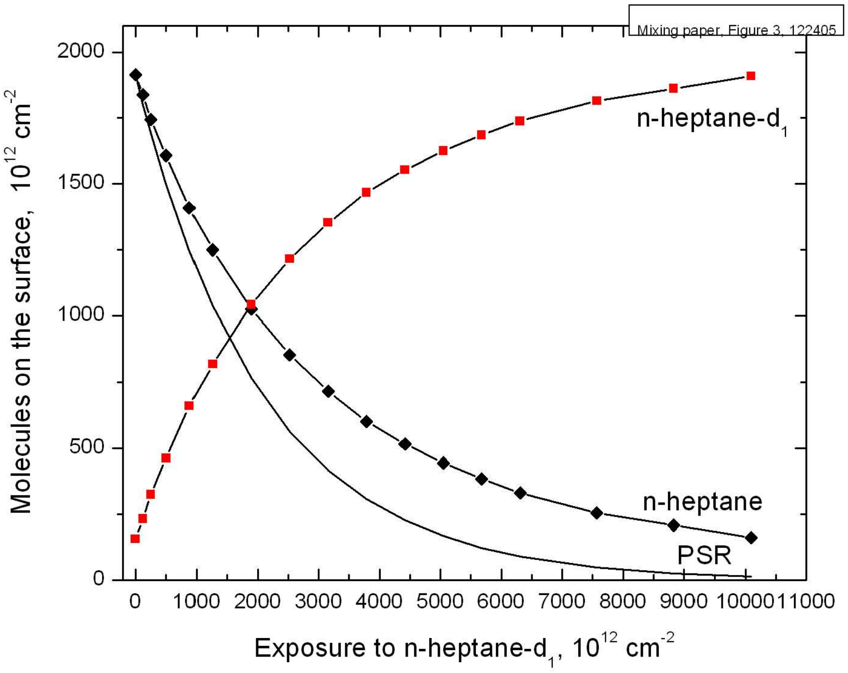

Figure 54: Displacement of n-heptane with n-heptane-d$_1$. Finite rate of diffusion causes the deviation from the first-order exponential decay dictated by the perfectly stirred reactor model (PSR).

total capacity (1 c.u. $= 2070\times10^{12}$ molecules cm^{-2}). On such a plot, the PSR model results in a line with a slope of -1 passing through the origin. This slope corresponds to the highest rate of displacement. Less efficient mixing causes the positive deviation of the slope from the PSR model.

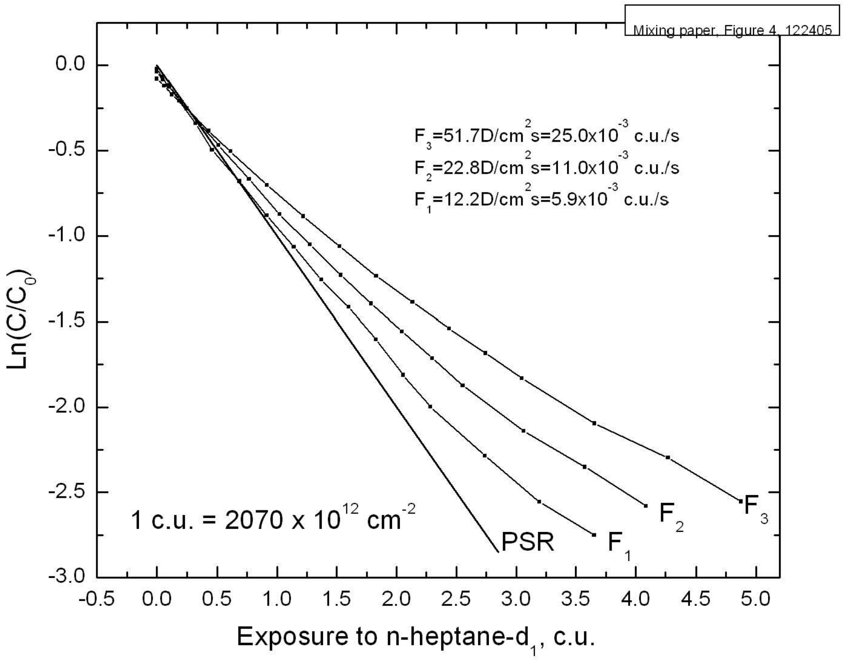

Figure 55: Displacement of n-heptane with n-heptane-d$_1$ at three different dosing rates, F$_i$. Faster dosing rates result in less efficient displacement. The line labeled PSR corresponds to perfectly stirred reactor model (F =0). The initial slopes, used to calculate the diffusion coefficient through the SWNT bulk, were found to be -1.0, -0.83, -0.70 for n-heptane-d$_1$ fluxes F$_1$, F$_2$, F$_3$ respectively.

We will show later that slight non-linearity noticeable at higher exposures in Figure 55 is likely caused by the inhomogeneities in the thickness of the SWNT deposit. We will use the initial linear regions of the curves to determine the self-diffusion coefficient under these conditions.

A straightforward physical model of the displacement process can be constructed in the following way. We will consider the SWNT deposit to have a uniform thickness of 0.25 μm and the transport of the molecules inside the deposit be governed by Fick's law of diffusion. The incoming n-heptane-d$_1$ molecules displace the molecules in the outer layer of the deposit with a 100% efficiency. The displaced molecules will be a mix of n-heptane and n-heptane-d$_1$ in the same fractional ratio as in the outer layer of the nanotube deposit. The 100% displacement efficiency assumption is justified by the experimental observation that during the very early stages of displacement at low n-heptane-d$_1$ fluxes only n-heptane molecules leave the surface. In other words, initially all n-heptane-d$_1$ remains in the nanotube deposit. This results in the initial slope of F$_1$ curve in Figure 55 that is very close to -1. Physically, this means that the lifetime of the incoming molecules on the surface is large enough for them to mix perfectly with the molecules in the outer layer. The other consequence of long initial residence time on the surface is the unity sticking coefficient, as mentioned before (Figure 53).

In order to follow displacement kinetics in a system corresponding to such a model, a differential equation for diffusion with two appropriate boundary conditions must be solved. The boundary condition for the outer layer is that n-heptane flux through the boundary is proportional the concentration of n-heptane. The other boundary condition stipulates that there is no flux of n-heptane through the surface of the nanotube deposit adjacent to the gold plate. An analytical solution for this particular problem exists,[153] however, it has a drawback of being non-algebraic. For this reason we used a fairly straightforward finite differences approach, as described in [154].

There are three parameters in this model: diffusion coefficient D, deposit thickness L, and the fraction of molecules replaced in the outer layer in unit time, α. The dimensionless ratio $D/(\alpha L^2)$ fully defines the displacement kinetics. Several displacement curves produced by the model are shown in Figure 56 using the same coordinates as on the experimental plot in Figure 55. The displacement curves in Figure 56 are nonlinear at low exposures. They become linear after exposures greater than approx. 1 c.u. Decreasing $D/(\alpha L^2)$ leads to lower negative values of slope.

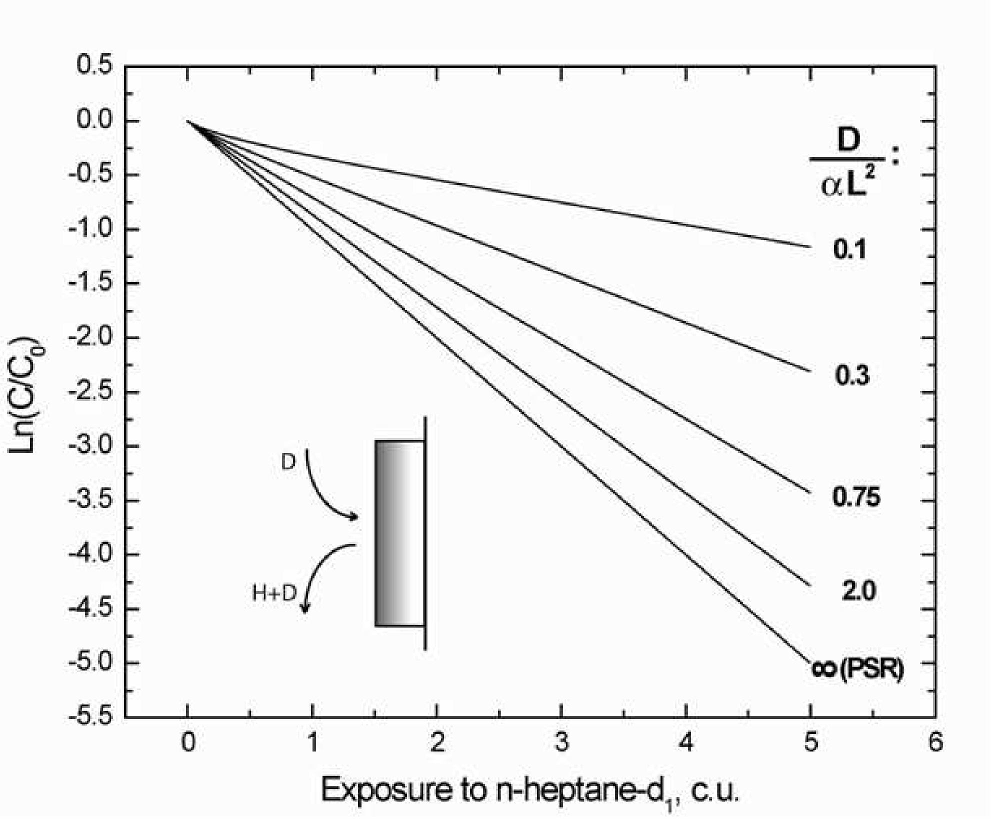

Figure 56: Coupled diffusion-displacement model. Displacement of *n*-heptane (denoted by H in the schematic) by *n*-heptane-d$_1$ (denoted by D). The dimensionless ratio $D/(\alpha L^2)$ (defined in the text) controls the kinetics of the process.

The model allowed us to determine the diffusion coefficient. Knowing L (0.25 μm) and α (F_i's from Figure 55 expressed in c.u.), we solve for the value of D such that the slope of the displacement curve given by the model matches the initial slope of the experimental displacement curves. Two experimental curves from Figure 55 were employed in this analysis, F_2 and F_3. The value of D=1.2×10^{-11} cm^2/s gave a good agreement with initial slopes of both experimental curves. This value compares to the bulk-phase value of 2.4×10^{-5} cm^2/s at 275 K.[155] We did not use the α=F_1 curve in the analysis because of the insensitivity of slope to the value of D at high $D/(\alpha L^2)$.

This value of diffusion coefficient is about 8 orders of magnitude lower than that obtained for n-heptane inside a filled nanotube found from MD simulations, 8.2×10^{-4} cm^2/s (see below). This indicates that the diffusion inside nanotubes is not the rate-limiting step in n-heptane mixing throughout the nanotube sample. As the n-heptane in the sample is partitioned into separate populations inside open nanotubes, it is logical to conclude that the slow diffusion observed in the experiment is caused by slow exchange of n-heptane between different nanotubes.

The non-linearity at higher exposures in the experimental data can be explained by thickness inhomogeneities in the nanotube deposit. Thicker areas have a lower $D/(\alpha L^2)$ and thus are more slowly depleted of n-heptane, starting to dominate when the amount of remaining n-heptane becomes low. In the determination of the self-diffusion coefficient we used the slope at low exposures from the experimental curves where it is fairly constant.

9.3.3 Adsorption of n-heptane on a model SWNT bundle

We have computed adsorption isotherms for n-heptane adsorbing on the external and internal surfaces of a model SWNT bundle in order to estimate the external bulk phase pressure that corresponds to different loadings. The computed isotherms are plotted in Figure 57. The solid circles represent adsorption on the external surface of the nanotubes; this would occur if the internal sites were blocked or if diffusion into the nanotube interior was kinetically limited. The graphic insets in Figure 57 are snapshots from the simulations, showing a typical coverage of n-heptane on the SWNT bundle. Considering only external adsorption, molecules first adsorb in the groove site and the density is seen to increase smoothly with increasing pressure. There is no evidence for a layering transition as might be expected on graphite.[156, 157] The first plateau-like region from about 10^{-2} to 10^{-1} Torr corresponds roughly to groove site filling. The next rise in the isotherm is indicative of adsorption taking place on the external surface of the nanotubes. This is followed by a steep rise in coverage that marks the beginning of the multilayer.

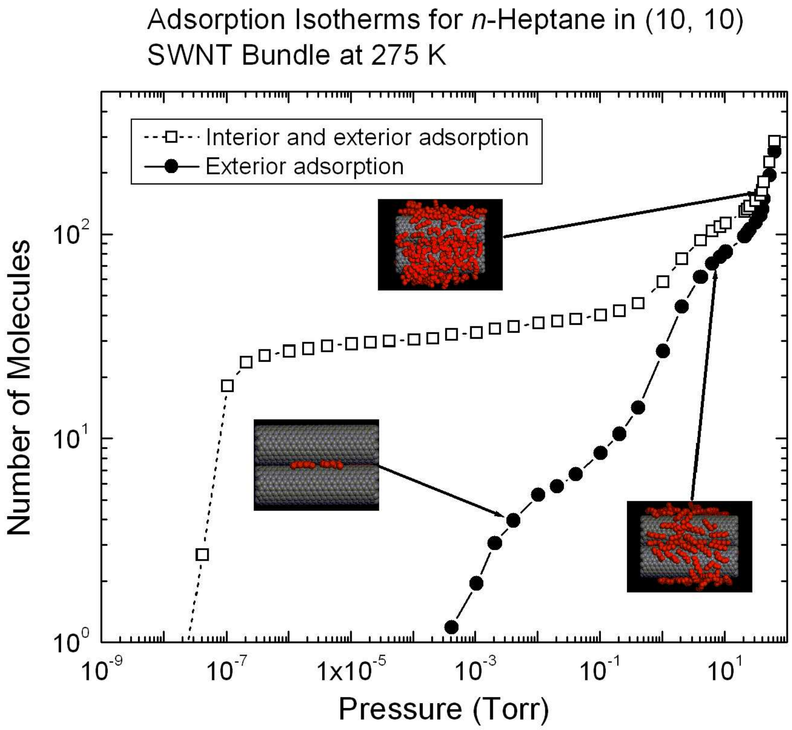

Figure 57: Adsorption of n-heptane at 275 K on a model SWNT bundle containing two nanotubes. The filled circles are for adsorption only on the external surface of the nanotubes and the open squares indicate adsorption both on the internal and external sites. Representative snapshots from the simulations are shown as insets.

The simulations indicate that at the experimental pressures (10^{-9} Torr) the interior sites can only be populated in a quasi-equilibrium fashion. However, one has to remember that during the dosing of the adsorbates the sample is exposed to far higher local pressures which permit the filling of the nanotube interior.

9.3.4 Self-diffusion inside individual SWNTs from MD simulations

We have calculated the self-diffusion coefficient for bulk liquid *n*-heptane from EMD simulations at 275 and 298 K. The results from our calculations are given in Table 8. The experimental value of the liquid self-diffusivity at 298 K is also reported in Table 8. The simulation and the experimental values at 298 K are in excellent agreement, giving us confidence that the potential models used in the simulations for *n*-heptane are physically reasonable. The liquid self-diffusivity at 275 K calculated from our simulations is physically reasonable, being slightly smaller than the value at 298 K. We have estimated an experimental value for the self-diffusivity at 275 K from interpolation of existing experimental data.[155] Our simulation result is in reasonable agreement with the interpolated value, given the errors involved in the interpolation process.

Table 8: Calculated and experimental[155] self-diffusion coefficients for bulk liquid *n*-heptane.

Temperature (K)	Self-diffusion coefficient ($D_s \times 10^5$ cm^2/s)	
	Simulations	Experiments
275	2.7 (0.1)*	2.4**
298	2.9 (0.3)*	3.1

*The numbers in the parenthesis are the estimated standard deviations, i.e., 2.7(0.1) means 2.7±0.1. **interpolation value from experimental data.

The self-diffusion coefficient for *n*-heptane inside a (10, 10) SWNT at liquid-like loadings has been computed from EMD simulations. The loading used in the simulations corresponds to a pressure of about 1.5×10^{-3} Torr, as indicated in Figure 57. The calculated value is $8.2\pm1.0\times10^{-4}$ cm^2/s, which is about a factor of 28 larger than D_s for bulk liquid *n*-heptane at the same temperature. The fast diffusion of *n*-heptane in SWNTs is consistent with results from simulations of other molecules[137, 138, 140] and can be attributed in part to the smooth nature of the surface of SWNT internal channels. In addition, the *n*-heptane molecules are more ordered inside a nanotube due to the confinement than in bulk phase. We note that the self-diffusivity of molecules in nanotubes has been shown to dramatically decrease with increasing loading in going from very dilute to liquid-like loadings.[119, 134]

Previous simulations have demonstrated that the self-diffusivity of simple molecules in SWNTs in the limit of dilute loadings is dramatically affected by nanotube flexibility.[116, 139] This may also be the case for alkanes. However, self-diffusivities of small molecules at high, liquid-like loadings in flexible and rigid nanotubes are virtually identical, owing to the fact that self-diffusion becomes dominated by adsorbate-adsorbate collisions at high loading.[116, 119, 134, 139, 143]

The very large value of D_s for n-heptane in SWNTs indicates that mixing of n-heptane-d$_1$ with n-heptane inside the nanotubes cannot be the rate limiting step. Indeed, the diffusion is so fast that it cannot be measured by the experimental methods used here. We therefore are led to look for other processes that may be rate-limiting in the mixing of n-heptane-d$_1$ with n-heptane.

9.3.5 Kinetics of entry and evaporation

We expect that the entry of molecules into the nanotube interior will be much slower than diffusion within the nanotube, because of the presence of an energy barrier to entry.[88] The energy barrier is largely due to reduced coordination as a molecule leaves the groove site and begins to enter the nanotube interior site. It is extremely difficult to study the precise kinetics of n-heptane entry into the nanotubes because of our lack of knowledge about the geometry and chemistry of entry ports. Most of the interior sites of nanotubes within the sample must be blocked, based on the observation that the area under the TPD peak assigned to interior sites is smaller than that assigned to the groove or exterior sites in Figure 53. The fraction of nanotubes that are available for interior adsorption may have entry ports at the ends or in the side-walls of the nanotubes. These entry ports may have carbon atoms terminated with hydrogen, with some other species, or may have dangling bonds. We have chosen to use a very simple model to investigate the kinetics of alkane entry into the nanotubes. We have monitored n-heptane trajectories on a two-nanotube bundle, schematically shown in Figure 53, as a method for qualitatively examining the kinetics of entry. We performed two types of simulations under three different loading conditions. In the first case we simulated nanotubes that were initially empty (no internal site adsorption) with n-heptane initially only on the external surface of the bundle. The second case involved simulating nanotubes that were filled (saturated) with *n*-heptane. The external loading conditions for both types of simulations were classified as “low” meaning four *n*-heptane molecules, “medium”, with 72 molecules (roughly one monolayer), and “high”, with 146 molecules (partially filled second layer) on the external surface. In each case MD simulations were performed at 275 K for a total of 10 ns of simulation time. Statistics were collected on the number of molecules entering the internal sites from the external surface, the number of molecules leaving the internal sites, and the number of molecules desorbing from the surface of the nanotube into the gas phase. Molecules which desorb to the gas phase were observed to re-adsorb very rapidly, since the simulation cell was rather small, being only 100 Å on a side, making it possible to rapidly equilibrate the adsorbed and vapor phases.

1. Initially empty nanotubes

   The data collected for simulations on initially empty nanotubes are shown in Table 9. The molecules in the low coverage simulation essentially remained in the groove sites during the simulation. No molecules entered the internal sites and no molecules desorbed to the gas phase. The medium coverage case, corresponding to nearly a complete monolayer, had many desorption events, but few molecules were able to enter the SWNT internal sites within the 10 ns time. The internal sites require about 30 molecules to be saturated. Some of the molecules are partially inside the nanotubes. The large number of desorption events is an artifact of the definition of desorption. The change in the internal site loading as a function of time is plotted in Figure 58. We see that molecules enter one-by-one for the medium coverage case and that the first molecule does not enter the nanotube until after 2 ns.

   At high loadings we observe a much higher rate of molecules entering and exiting the nanotube interior sites than would be expected from simple scaling with the number of molecules on the external sites. The ratio of molecules in the high and low coverage cases is 146/72=2.03, while the ratio of molecules entering the nanotubes in the high and low coverage cases is 92.7/3.9=23.8. However, this number includes molecules that exit the nanotube and then re-enter. Even excluding this number the net rate of molecules entering at high coverage appears to be larger than can be expected in terms of an increase

Table 9: Statistics for n-heptane on a model SWNT bundle that is initially empty. The simulations were run for 10 ns at 275 K.

Number of molecules	Low coverage	Medium coverage	High coverage
Entering internal sites	0	3.9	92.7
Leaving internal sites	0	0	57.7
Desorbing to the gas phase	0	65.3	2870.8

in coverage, 35.4/3.9=9.1 We caution, however, that the statistics are very poor, but there is some evidence that entry into the nanotube is accelerated by cooperative effects and is not simply proportional to coverage. When the coverage is high it is possible to have many molecules near the mouth of the nanotube, which increases the average coordination and reduces the energy penalty for molecules entering or leaving the nanotube.

We note that the apparent net rate of molecules entering the nanotube, seen as the slope of the lines in Figure 58, decreases at about 7 ns for the high coverage case, because the nanotube becomes filled at that point. This is manifested by the plateau, a nearly zero rate of increase, from about 7 to 10 ns. The rate of evaporation to the gas phase is about a factor of 48.4 higher for the high coverage case compared with the medium coverage case. This is a result of the second layer molecules being much more weakly bound than the groove site and first layer molecules.

The externally bound molecules observed in our simulations are analogous to intrinsic precursor state molecules, which have been observed in single crystal experiments. We note that the low evaporation rate observed for the low coverage case is consistent with the experimental observation of a sticking coefficient near unity at low coverage, as seen in Figure 54.

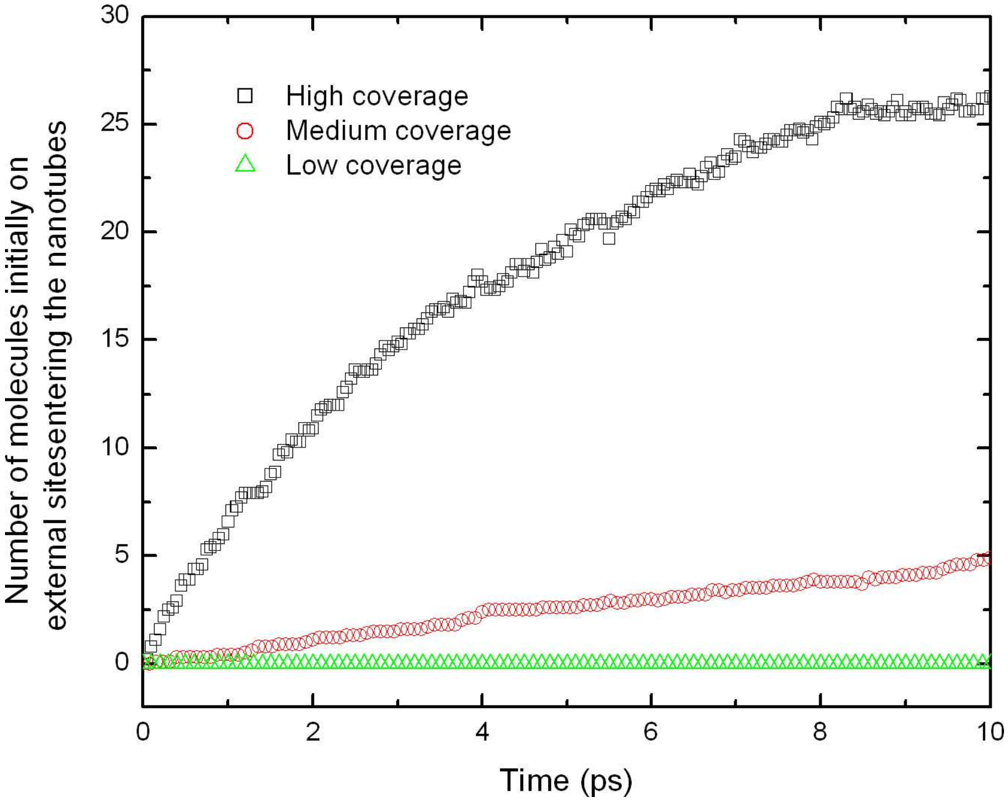

Figure 58: The net number of molecules entering the nanotube internal sites as a function of simulation time for three different loadings at 275 K.

2. Initially filled nanotubes

   The experimental data presented in Figures 55 and 56 pertain to the exchange of molecules from the external to the internal sites when the internal sites are initially filled. We have therefore collected statistics on the number of molecules that enter the nanotubes that were initially on the external surface, as well as the total number of molecules entering and leaving the nanotubes. The data from these simulations are presented in Table 10.

Table 10: Statistics for *n*-heptane on a model SWNT bundle that is initially full. The simulations were run for 10 ns at 275 K.

Number of molecules	Low coverage	Medium coverage	High coverage
Entering internal sites	0	24.6	282.3
Initially on the external sites that enter internal sites	0	4.9	26.3
Leaving from internal sites	0	21.2	276.4
Leaving from outside surface to gas phase	0	39.1	4296.8

At low coverage, none of the molecules that were initially adsorbed on the external surface of the nanotube enter the nanotubes over the 10 ns simulation run, as shown in Figure 59. At a medium coverage of the external sites a total of 24.6 molecules enter the internal sites. These are largely due to molecules that were initially inside the nanotube exiting and reentering the internal sites. However, at medium coverage a total of about five molecules initially on the external sites enter the internal sites, as can be see from Figure 59 and Table 10. Assuming that the rate does not change in time gives a rate of exchange of 0.5 molecules/ns. There is a net increase of 3.4 molecules from the internal sites over the entire simulation.

At high coverage more than 70% of the molecules initially inside the nanotubes are replaced by the molecules that were initially on the external sites within the 10 ns simulation. We see from Figure 59 that the rate of exchange slows at about 7 ns, similar to

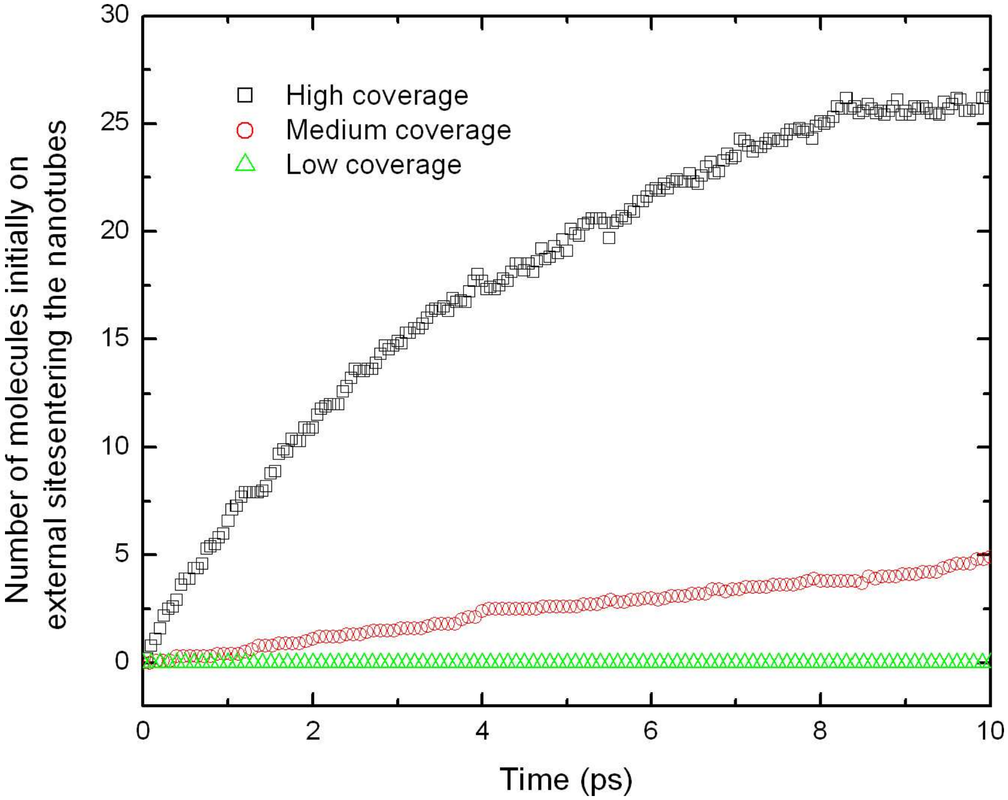

Figure 59: Number of *n*-heptane molecules that were initially on the external bundle site that enter the nanotube interior sites over a 10 ns simulation at 275 K. The nanotubes were initially filled with *n*-heptane.

the slowing in the rate of entry seen for the high coverage case in Figure 58. However, the slowing in this case is due to the fact that most of the n-heptane molecules inside the nanotubes have already been exchanged with those on the outside, so that it is most likely that a molecule exiting the nanotube will be one that was originally on the external surface, and hence does not contribute to the exchange rate. Estimating the exchange rate based on the first 7 ns of the simulation we obtain a rate of 3.4 molecules/ns, a factor of 6.8 larger than the medium coverage case. [Note we should just use the initial slope, before a significant fraction of molecules have been exchanged] The exchange rate is significantly larger than can be accounted for by the increase in external coverage (factor of 2.03), again indicating the existence of cooperative effects. We therefore cannot reliably estimate the exchange rate at low coverage based on the measured rate at high or medium coverages. Nevertheless, we can extrapolate the medium coverage rate to low coverage to get an order of magnitude guess by assuming first order kinetics, which yields a rate of 0.03 molecules/ns.

9.4 SUMMARY

At 275 K heptane molecules adsorbed on SWNTs form isolated islands inside open nanotubes. Experimentally measured long-range self-diffusion coefficient for n-heptane was found to be $D_s = 1.2\times10^{-11}$ cm^2/s in the 0.25 μm thick nanotube sample. Molecular dynamics simulations show that self-diffusion of n-heptane inside individual nanotubes (intratube diffusion) is about 8 orders of magnitude faster (D_s=8.2×10^{-4} cm^2/s). This indicates that the experimentally observed slow diffusion is rate-limited by the exchange of n-heptane between different nanotubes (intertube diffusion). The diffusion inside individual nanotubes is also faster than the bulk diffusion at the same temperature (D_s=2.4×10^{-5} cm^2/s), which is likely the result of molecular ordering inside nanotubes due to confinement.

Molecular simulations of a simple model system indicate that entry of n-heptane into the nanotubes from the external surface is a slow process compared with diffusion. Moreover, there is evidence of cooperative effects as the exchange rate increases more rapidly than can be accounted for by first-order kinetics.

10.0 SPECTROSCOPIC STUDIES OF WATER CONFINED IN CARBON NANOTUBES

10.1 INTRODUCTION

This chapter is largely based on one of our publications, "Unusual Hydrogen Bonding in Water-filled Carbon Nanotubes".[158] The experimental work was done by Dr. Oleg Byl. The Monte Carlo adsorption simulations were done by Dr. Jinchen Liu. The VASP calcualtions were done by Dr. Wai-Leung Yim. The author did the molecular dynamics simulations.

Confined matter on the nanometer scale differs significantly from bulk matter.[12] Widespread interest exists in the structure of confined water[159, 160, 161, 162, 163, 164, 165, 166, 167, 168] in its degree of hydrogen bonding,[164, 169, 170, 171, 172, 173] and in proton transfer through "water wires".[174, 175] The special properties of confined water can influence molecular transport inside membrane pores.[176, 177]

Confinement of water can be reached by limiting the size of water agglomerates in 1, 2 or 3 dimensions. In an infinite ice crystal each water molecule complying with the "bulk ice rule"[159] is tetrahedrally coordinated, simultaneously donating and accepting two hydrogen atoms forming a hydrogen-bonded network. However this arrangement is disrupted in agglomerates of crystalline water of finite sizes leading to a variety of shapes for small water clusters with different types of OH groups ranging from bulk-like to essentially free OH groups. This diversity can be readily detected by means of vibrational spectroscopy that provides one of the most insightful means for OH characterization.[178]

A number of experimental vibrational spectroscopy studies of water clusters with sizes ranging from few molecule agglomerates,[179, 180, 181] to hundred and thousand molecule clusters,[182] to macroscopic crystals[183, 184, 185] show that four major types of OH stretching modes can be detected for water structures with reduced dimensionality. These modes originate from the OH groups that belong to the following water species (spectral regions given in parenthesis): "free OH" groups dangling from the surface (3690-3720 cm^{-1}); double H-atom donor-single O-atom acceptor ($\sim$3450 – 3550 cm^{-1}); water molecules in a distorted tetragonal coordination ($\sim$3400 – 3450 cm^{-1}); and single donor-double acceptor (3050 – 3200 cm^{-1}). The position of the OH stretching mode points to the degree of involvement of the OH group into the hydrogen-bond network. Studies of the ice surface show that water molecules tend to rearrange into surface ring structures to reduce the number of "free OH" groups.[183, 184, 185]

In accord with experimental studies, theoretical calculations on water clusters indicate that water agglomerates can be stabilized by minimization of the number of free OH groups.[179, 186, 187, 188, 189] This occurs by formation of rings composed of hydrogen bonded H_2O molecules. Thus, a water cluster may have several rings of different sizes that can be irregularly oriented with respect to each other. Some computations show that the structures with water rings stacked on top of each other are one of the most stable. However experimental verification of this can be complicated by the larger number of possible cluster shapes with an increasing number of water molecules in the cluster.

Single wall carbon nanotubes have been shown to be a useful material for investigation of confinement effects.[11, 91, 190, 191, 92, 10] They possess a deep van der Waals adsorption potential well in the interior. Quasi-one-dimensional conditions can be realized in the nanotube, thanks to their macroscopic lengths and diameters of about one nanometer. The nanotube interior is an ideal medium for the study of the hydrogen bond network under extreme conditions, since a nanotube can provide a confining geometry without a strong interaction with H_2O molecules, which may influence the hydrogen bonding.

Molecular dynamics calculations indicate that water confined in nanotubes less than 2 nm in diameter forms n-gonal structures formed of stacked rings at temperatures below $\sim$280 K and pressures above 50 MPa.[160, 165, 192, 193, 194] Each ring consists of n H_2O molecules (n = 4-6, depending on the nanotube diameter) with one OH group lying in the ring plane and the other oriented perpendicular to it. In this case, each water molecule (except those in the edge rings) in these phases is four coordinated, i.e., each satisfies the "bulk ice rule".

At higher temperatures two water phases have been predicted for nanotubes with diameters larger than 1.26 nm, namely the wall phase and the axial phase. The axial phase disappears upon cooling, causing a discontinuous liquid-solid phase transition.[163]

These predictions have been verified experimentally by X-ray diffraction,[167, 168] NMR[195] and neutron diffraction[163] studies. The most recent X-ray diffraction study of nanotube samples, with different average diameters, confirmed the dependence of number of water molecules in a ring on the nanotube diameter.[168] The NMR study has shown that a liquid-to-solid transition for water confined in nanotubes proceeds in two steps: the axial phase freezes first, followed by solidification of the wall phase. A vibrational spectrum of water confined in carbon nanotubes has been studied by means of inelastic neutron scattering.[163] It was shown that the OH stretching mode of the confined water shifts to higher frequencies relative to the bulk ice. This shift has been attributed to weakening of the hydrogen bonds due to formation of n-gonal H_2O structures inside nanotubes.

The strength of hydrogen bonds in n-gonal water structures (for n=5, 6) confined in the nanotube interior has been studied by *ab initio* methods.[194] Theoretical predictions indicate that in the pentagonal water structure the axial (inter-ring) hydrogen bond should be weaker than the in-plane (intra-ring) hydrogen bond. This prediction is based on density functional theory calculations of the effective charges on the atoms and on calculated charge densities. The non-equivalency of two hydrogen bonds should lead to two different vibrational features and can be detected by means of IR spectroscopy.

To-date there has not been any direct experimental confirmation of the predicted weaker hydrogen bonds for water confined in single wall carbon nanotubes. In this work we report the first observation of a distinct sharp vibrational mode at 3507 cm^{-1} that is unambiguously associated with a distorted hydrogen bond for water inside nanotubes. The location of the water molecules is determined by studying the effect of blocking the nanotube interior with n-nonane causing the 3507 cm^{-1} band to be absent when water is adsorbed on the nanotubes. Our calculations are the first to directly link the structure of the water inside the nanotubes to the specific vibrational feature observed at 3507 cm^{-1}, predicted from both *ab initio* and classical simulations. We therefore demonstrate that vibrational spectroscopy, coupled with detailed molecular modeling, can be used as a sensitive probe of changes in hydrogen bonding due to confinement. This methodology may prove useful for investigating water in other highly confined environments.

10.2 EXPERIMENTAL

The nanotubes were obtained from Prof. Smalley's group and were used in our previous studies.[91, 190, 196, 84, 104, 103] Nanotubes were deposited directly onto a tungsten grid, which was inserted into a vacuum-IR cell.[91, 197] Opening of the nanotubes by ozonation was carried out in two 5 min cycles with 17.2/18.1 Torr and 17.3/18.2 Torr initial/final O_3 pressures respectively.[91, 190, 94, 198] The nanotubes were then annealed at 873 K for 30 min to remove the functionalities formed during the ozonation procedure. The resulting opening of the nanotubes was tested by CF_4 adsorption before and after the etching.[91]

The experiment involving H_2O diffusion into the nanotube interior was carried out as follows: 1. Water vapor was condensed to form amorphous ice on the outer geometric surface of the nanotubes at 123 K. Diffusion of water into the interior of the nanotubes is severely kinetically restricted at this temperature; 2. After the deposition and condensation, the sample was heated to 183 K and immediately quenched back to 123 K at a rate (in both directions) of 1 K/s; 3. Consecutive annealing and cooling cycles led to gradual removal into vacuum of both condensed ice and water adsorbed inside the nanotubes. A series of spectra for five heating/cooling cycles are shown in Figure 63; it is observed that a monotonic increase occurs in the ratio of the singular OH absorbance at 3507 cm^{-1} to the integrated associated OH absorbance at lower frequencies as the coverage of water decreases.

Liquid He was used to decrease the sample temperatures for testing H_2O diffusion inside nanotubes at very low coverages. The sample temperature was set within the range of 30-45 K and a small amount of H_2O was dosed. Then the sample was heated to 153 K and cooled back to the initial temperature with a 1 K/s rate in both directions. Infrared spectra were measured before and after the heating. Figure 64 clearly shows the absence of the 3507 cm^{-1} mode before annealing, followed by its appearance as H_2O mobility occurs upon increasing the temperature.

To probe the internally bound water we utilized adsorbed n-nonane to block interior sites in the SWNTs. Figure 65 shows pairs of IR spectra of water condensed on SWNTs with and without n-nonane blocking of the interior sites. N-nonane was condensed on the nanotubes at 123 K and then the sample was heated to 283 K for 15 minutes before cooling back to 123 K. Other experiments.[103] have shown that this results in n-nonane occupancy of the interior nanotube sites. Water was then condensed on the sample at 123 K, following by heating to 183 K and cooling to 123 K for IR measurements. Control water adsorption experiments without prior n-nonane adsorption were carried out. Figure 65 shows results for the 4^{th}, 5^{th} and 6^{th} annealing cycles for experiments with and without n-nonane blocking of the interior nanotube sites. It is clear that the 3507 cm^{-1} mode is only observed in the absence of blocking of the internal SWNT sites.

10.3 COPUTATIONAL METHODS

10.3.1 Potential models

1. Molecular models for water

   We used the rigid SPC/E[199] and flexible SPC/E[200] water models for MC and MD simulations, respectively. The flexibility was introduced by the intra-molecular potential proposed by Toukan and Rahman.[201] The Hamiltonian we used for the flexible SPC/E water model was adapted from Praprotnik et al.[200] and is given by

$$\begin{aligned} H = &\sum_i \frac{p_i^2}{2m_i} + \sum_k \sum_{l=1}^{2} D_e \left[1 - \exp(-\alpha \Delta r_{l_k})\right]^2 + \tfrac{1}{2}\sum_k k_\theta \Delta r_{3_k}^2 \\ &+ \sum_k k_{r\theta} \Delta r_{3_k} (\Delta r_{1_k} + \Delta r_{2_k}) + \sum_k k_{rr} \Delta r_{1_k} \Delta r_{2_k} \\ &+ \sum_{i>j} \left\{ \frac{q_i q_j}{4\pi e_0 r_{ij}} + 4\varepsilon_{ij} \left[\left(\frac{\sigma_{ij}}{r_{ij}}\right)^{12} - \left(\frac{\sigma_{ij}}{r_{ij}}\right)^{6} \right] \right\}. \end{aligned} \tag{10.1}$$

   The first summation is over all atoms, m_i and p_i are the mass and momentum of the ith atom, respectively. The indices k and l run over all molecules, and all sites on a molecule, respectively. $\Delta r_{1_k}$and $\Delta r_{2_k}$are the changes in the O–H bond lengths relative to the equilibrium bond length, $\Delta r_{3_k}$is the stretch in the H–H distance of the kth molecule,

D_e is the depth of the Morse potential, $\alpha = \left(\sqrt{k_r}/2D_e\right)$, k_r, k_θ, $k_{r\theta}$ and k_{rr} are the intramolecular force constants, q_i is the charge on the ith atom, r_{ij} is the distance between the ith and jth atoms on different molecules, and ε_{ij} and σ_{ij} are the the Lennard-Jones potential parameters. Values for these parameters can be found in reference [200]. We note that there is an error in the sign of the Morse potential given in reference [200].

The fluid-fluid interaction potentials were truncated at 1.42 nm ($4.5\sigma_{ff}$). We have not included long-range electrostatic corrections; a simulation in a much longer nanotube with a fluid-fluid cutoff of 3.0 nm gave essentially identical results. We ran several test calculations using the reaction field method for accounting for electrostatic long-range interactions, but these simulations, with a range of different dielectric constants, gave results that were very similar to simulations with no long-range corrections. We have also compared our calculated IR spectra for bulk water with published simulations that utilized the Ewald technique for long-range electrostatics. Our results are described below.

2. Carbon nanotube model

   We used a structureless carbon nanotube in our simulations. The length of the nanotube was set to 3.06 nm in the z direction and periodic boundary conditions were applied in that direction. The radii for the (8, 8) and (10, 10) nanotubes are 0.542 and 0.678 nm, respectively. Water-nanotube interactions were modeled by an integrated potential.[11] Both oxygen and hydrogen atoms interact with the tube. The parameters given by Martí and Gordillo[202] were used in our simulations.

10.3.2 Simulation details

1. Monte Carlo simulations For simulation of water confined in a nanotube, we first used the GCMC simulation technique[149] to get the adsorption isotherms in the nanotubes at a temperature of 298 K. The isotherms are shown in Figure 60. For the length of the nanotube we used, we obtained 44, 55 and 77 molecules for the (8, 8) and (10, 10) SWNTs at pressure close to saturation, respectively. For the simulation of bulk amorphous ice, a cubic box with the box length of 2.917 nm containing 780 molecules was used. Then we performed parallel tempering Monte Carlo simulations[203] in the NVT ensemble over the

temperature range from 123 K to 298 K (318 K for (10, 10) nanotube). Parallel tempering was required to equilibrate the system at low temperatures because of the existence of very many deep local minima in the potential energy landscape. We used an orientational bias technique[203] for both GCMC and parallel tempering MC simulations to improve the sampling of the molecular orientations. Total run length of 1×10^8 configurations were used for GCMC simulations with half of which for equilibration. For the parallel tempering Monte Carlo simulations, we used run length of 4×10^8 configurations, half of which were used to relax the system. A configuration consisted of an attempt to make either a translation or rotation of a molecule for NVT simulation and additional creation and deletion for GCMC simulation. These moves were chosen with equal probability. The replica swap between adjacent replicas was made every 1000 (2000) configurations for confined (bulk) water simulations.

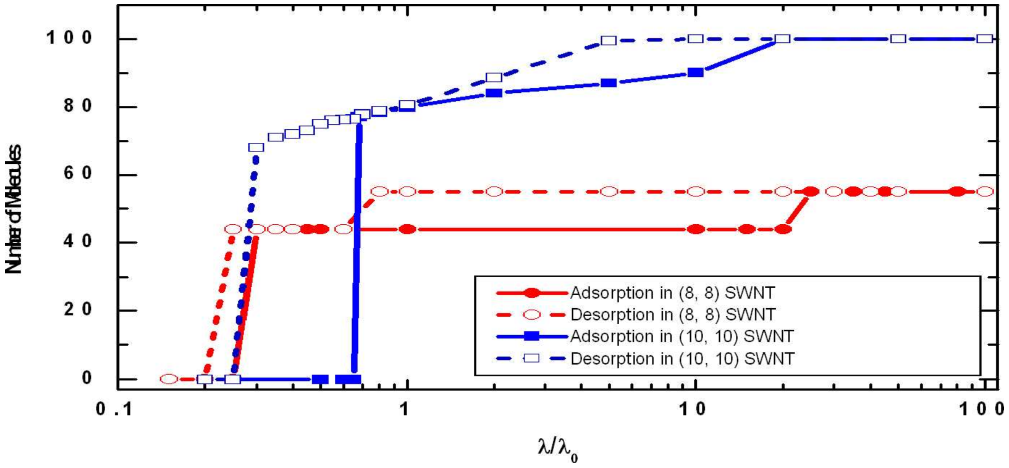

Figure 60: Adsorption isotherms for water confined in (8, 8) and (10, 10) SWNT at 298 K. λ_0 is the saturation activity at 298 K for SPC/E model. λ/λ_0 is the relative activity.

2. Molecular dynamics simulations We used the final configurations from the MC simulations as initial positions in the NVT MD calculations. Calculations were performed for bulk amorphous ice and water in nanotubes at 123 K. The bulk ice simulation was equilibrated for 20 ps, followed by 100 ps for data collection. Nanotube simulations were equilibrated for 400 ps followed by 200 ps for data taking. We used the Verlet leap-frog integrator with a 0.1 fs time step. This small integration time step is chosen to ensure correct accounting

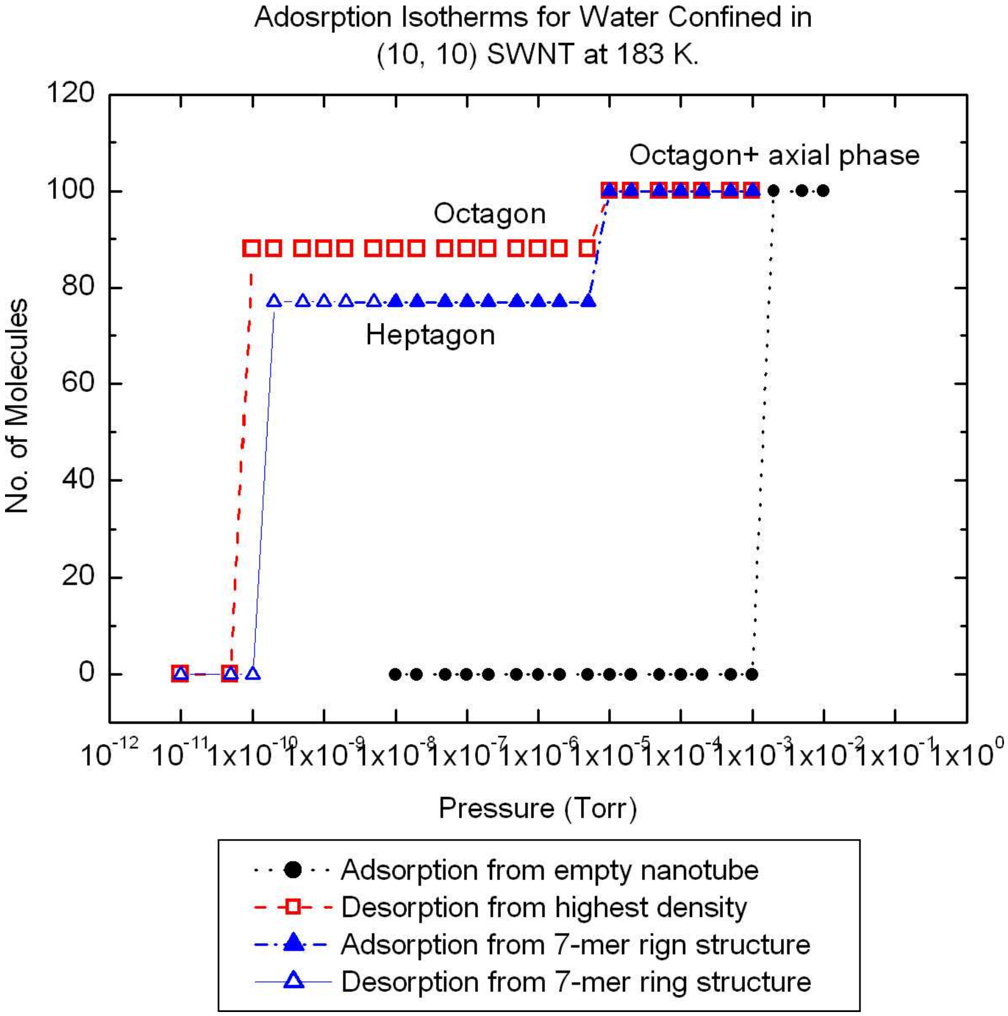

Figure 61: adsorption isotherms at 183 K for water confined in (10, 10) SWNT.

for the strong intra-molecular interactions. We used the Berendsen's thermostat[204] with a coupling constant of 0.1 ps. The IR spectra were calculated from the velocity auto-correlation functions.[205] We used only the hydrogen atom velocity auto-correlation function to calculate the IR spectra for computational efficiency, as this has been shown to give good results.[205] The spectra were computed from Equation (10.2) as described by Martí et al.,[205]

$$I(\omega) = \pi^{-1}\omega^{-2}\int_{0}^{\infty}\left\langle \dot{M}(t)\cdot\dot{M}(0)\right\rangle \cos\omega t dt, \tag{10.2}$$

where $\dot{M}(t)$ is the dipole moment velocity. The collective time correlation function of the dipole moment velocity is given by

$$\left\langle \dot{M}(t)\cdot\dot{M}(0)\right\rangle = q^2 Z^c_{\mathrm{HH}}(t) - 4q^2 Z^c_{\mathrm{OH}}(t) + 4q^2 Z^c_{\mathrm{OO}}(t), \tag{10.3}$$

where q is the charge on a hydrogen atom and Z^c_{XY} is the collective velocity correlation function between atoms X and Y. Martí et al.[205] have shown that Equation (10.3) can be approximated by

$$\left\langle \dot{M}(t)\cdot\dot{M}(0)\right\rangle \approx q^2 Z_{\mathrm{HH}}(t) = \left\langle V_{\mathrm{H}}(t)\cdot V_{\mathrm{H}}(0)\right\rangle, \tag{10.4}$$

where V_H is given by

$$V_{\mathrm{H}}(t) = \sum_{i=1}^{2N} v_{\mathrm{H}_i}(t) \tag{10.5}$$

and v_{H_i} is the velocity of the ith hydrogen atom and N is the total number of water molecules.

We have tested the effect of long-range electrostatic corrections on the calculated IR spectra by comparing our results using a simple truncation with spectra published by Martí et al. who used the Ewald method to account for long-range electrostatics.[205] We performed a simulation for bulk water at 298 K and density of 1 g/cm^3 using the SPC model, which was used by Martí et al. in their calculations.[205] The simulation cell is a cubic box with length equal to 2.86 nm, containing 780 water molecules. We used Verlet leapfrog integrator with a 0.5 fs time step. The system was equilibrated for 200 ps followed by 400 ps for data collection, as these values were the same as those used

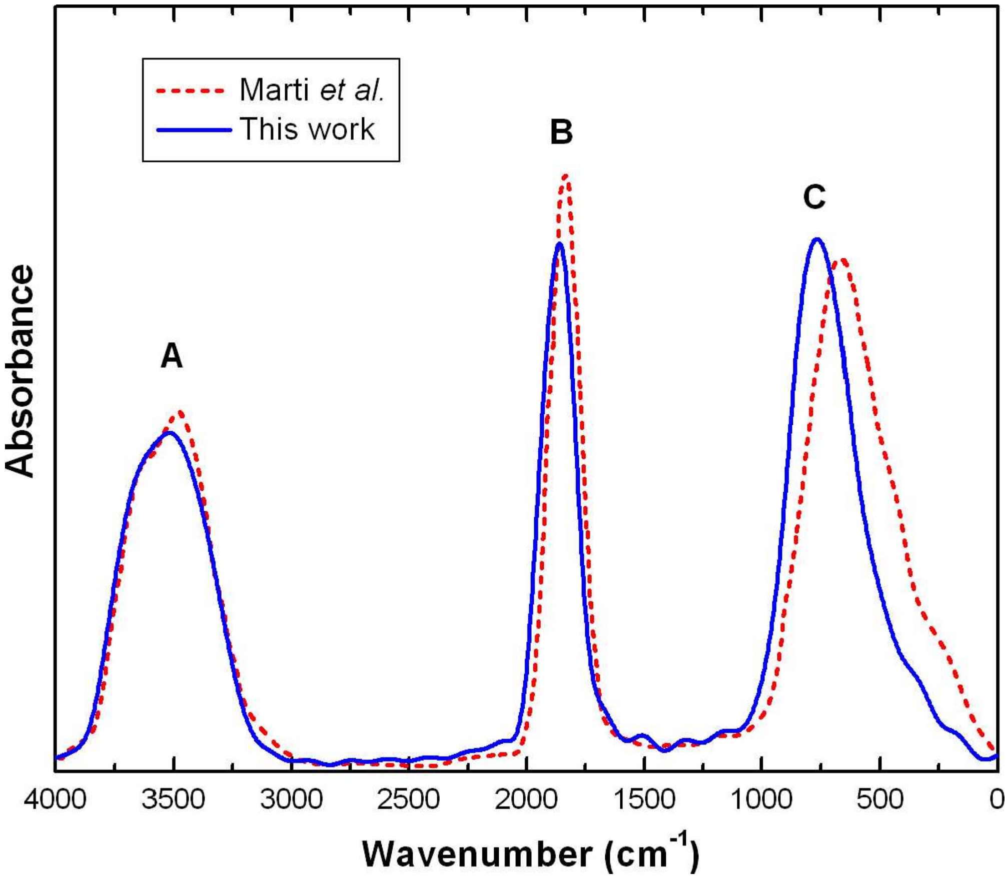

Figure 62: The computed IR spectra for bulk water at ambient conditions. Solid blue line was computed without any long-range electrostatic corrections. The dashed red line was computed using the Ewald summation technique.

by Martí et al.[205] Our results are plotted in Figure 62, along with data from Martí et al.[205]

The two spectra plotted in Figure 62 are very similar, especially for modes A and B. Mode A is due to the O-H stretching motions and mode B is due to bond bending. These two modes are apparently not affected by long-range electrostatic corrections. Mode C from our calculations has a peak about 80 cm^{-1} higher in frequency than that computed by Martí *et al.* Mode C corresponds to librational motions, which are apparently more sensitive to the long-range electrostatic interactions. The excellent correspondence for modes A and B between calculations with no long-range electrostatic corrections and the published data using the Ewald technique verify that the O-H stretching modes are insensitive to long-range electrostatics for the large cutoff values we have used.

3. Quantum mechanical calculations We have used the Vienna Ab Initio Simulation Package (VASP)[206, 207, 208, 209] to compute DFT optimized structures and vibrational frequencies for gas phase water, water in ring structures, and water inside a SWNT. We have used the PBE generalized gradient exchange-correlation functional[210] for all calculations. VASP is an implementation of periodic planewave DFT. We used projector augmented wave (PAW) pseudopotentials in our calculations with an energy cutoff 400 eV and an augmentation charge cutoff of 645 eV. Geometry optimizations were performed with the conjugate gradient algorithm as implemented within VASP. The energy convergence thresholds for the electronic structure self-consistent field calculations and the geometry optimizations were both set to 1×10^{-4} eV. Vibrational frequencies were computed from numerical differentiation of the forces, with displacements set to 0.02 Å. The gas phase H_2O antisymmetric ν_3 and symmetric ν_1 frequencies computed from VASP were 3830 cm^{-1} and 3702 cm^{-1}, respectively. The gas-phase calculations were carried out by placing a single H_2O molecule in a box 20 Å on a side. Only the Γ point was sampled in k-space. The 5- and 7-membered ring structures were placed in hexagonal supercells containing a single water ring. The 5-membered ring box size was 20 Å × 20 Å × 2.9 Å and the 7-membered ring box size was 22 Å × 22 Å × 2.9 Å. A Monkhorst-Pack[211] k-point grid of 1×1×6 was used for both ring structures.

Calculations of a single H_2O molecule inside a (8,8) and a (10,10) SWNT have been performed within VASP. Four SWNT unit cells were used for both calculations. The box sizes were 14.2 Å × 14.2 Å × 9.9 Å and 16.8 Å × 16.8 Å × 9.9 Å for the (8,8) and (10,10) SWNTs, respectively. The k-point grid was 1×1×3. Stretching frequencies were 3814 cm^{-1} and 3697 cm^{-1} for H_2O in the (8,8) SWNT and 3815 cm^{-1} and 3686 cm^{-1} for H_2O in the (10,10) SWNT.

Infrared intensities and vibrational frequencies for 5- and 7-membered water rings were computed with the PWscf package.[212] Ultrasoft pseudopotentials and the PBE functional were used. The hexagonal supercell dimensions for the PWscf calculations were virtually the same as for the VASP calculations and the k-point grid was 1×1×6. The planewave energy cutoff for the PWscf calculations was 408 eV.

10.4 RESULTS AND DISCUSSION

10.4.1 Experimental Results

Figure 63, spectrum (a) shows the infrared spectrum in the OH stretching region following condensation of H_2O at 123 K on the outer geometric surface of the nanotubes. The 3693 cm^{-1} mode corresponds to the "free OH" groups dangling at the surface of the amorphous ice. These groups disappear upon annealing due to surface reconstruction. Spectra (b) through (f) show the consecutive changes that occur as programmed heating to 183 K, followed by quenching to 123 K, occurs (both at 1 K/s rate). The annealing enhances water mobility resulting in H_2O diffusion into the nanotube interior as well as water desorption into vacuum, decreasing the overall amount of condensed water. The development of a high frequency isolated OH vibrational mode at 3507 cm^{-1} was observed in addition to associated OH features in the 3000 cm^{-1} – 3450 cm^{-1} region.

Figure 64 shows the IR spectra for water condensed at medium and very low H_2O coverages on SWNTs measured before and after the first annealing cycle. In both cases we observe the appearance of a relatively sharp 3507 cm^{-1} mode after annealing. The change of the spectra in the 3000 cm^{-1} to 3600 cm^{-1} range, measured for the medium H_2O coverage (Figure 64A), indicates that water, initially condensed in an amorphous phase on the outer

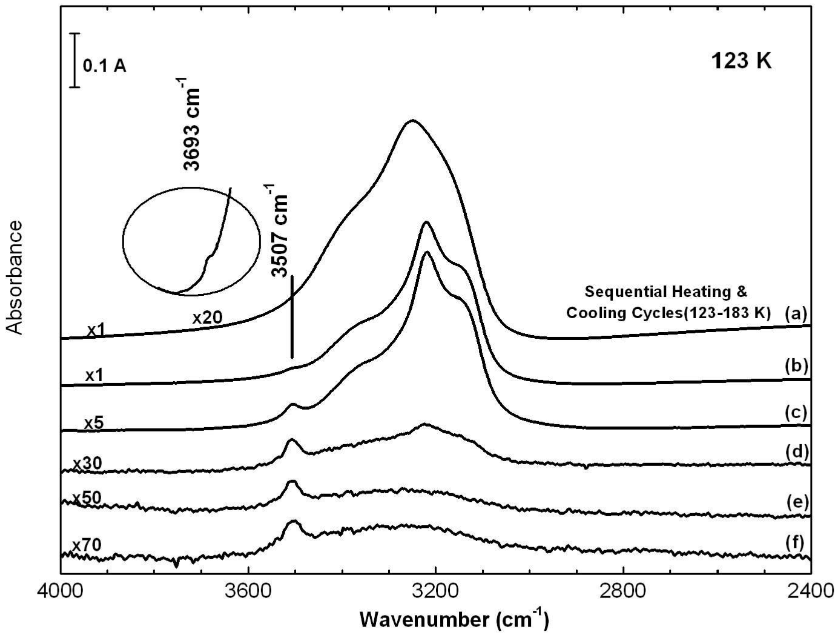

Figure 63: Changes in the IR spectra of H_2O condensed on single walled carbon nanotubes on heating in vacuum.

surface of the SWNTs, crystallizes upon annealing. Figure 64B shows that the 3507 cm^{-1} mode is not present in the spectra of condensed water before annealing. This indicates that the 3507 cm^{-1} mode originates from a structure that appears only at temperatures when water molecules possess higher surface mobility and can diffuse in the nanotube interior.

The assignment of the 3507 cm^{-1} mode to internally-bound H_2O is based on the effect of n-nonane blocking of the nanotube interior when it is adsorbed below 283 K. At this temperature n-nonane is trapped in the nanotube and prevents water from diffusing into the nanotube interior.[103] Figure 65 demonstrates that n-nonane blocking almost completely eliminates the mode at 3507 cm^{-1}. This clearly shows that the 3507 cm^{-1} mode originates form the water phase confined inside nanotubes. D_2O was employed to verify the observation of the singular OH stretching mode; an analogous mode was observed at 2595 cm^{-1}.

The vibrational spectroscopy of condensed water indicates that the higher the degree of involvement of a water molecule into the hydrogen bond network, the lower the frequency of the OH-stretching modes.[213, 214] In the gas phase spectrum, unbound H_2O molecules exhibit antisymmetric ν_3 and symmetric ν_1 stretching modes at 3756 cm^{-1} and 3657 cm^{-1}, respectively.[213] A high frequency 'free OH' stretching mode at 3693 cm^{-1} was observed by us (Figure 63) for dangling hydrogen atoms on the surface of ice nanocrystals at low temperatures, and has been reported by others.[215] This mode disappears as the ice nanocrystals are annealed above 140 K due to reconstruction on the ice surface that is accompanied by the formation of strained surface hydrogen bonds.[183] The OH modes of water molecules are red-shifted when the molecule is entrapped in a matrix and does not participate in H-bonding at all or participates only as a proton acceptor to form a hydrogen bond.[181, 213] For a proton donor water molecule, the stretching frequency of the OH bond involved in the H-bond network is much more strongly red-shifted relative to the group not involved in the H-bond.[181, 213]

One might imagine that the 3507 cm^{-1} mode observed inside nanotubes is caused by OH groups not directly hydrogen bonded but highly red-shifted by the confining environment. This would require a large red-shift of between 150 cm^{-1} and 250 cm^{-1} from the 'free-OH' stretching frequency. It is known that confined molecules inside SWNTs exhibit small red-shifts,[91, 190, 196] interaction of the benzene π electron cloud with the OH group of a water

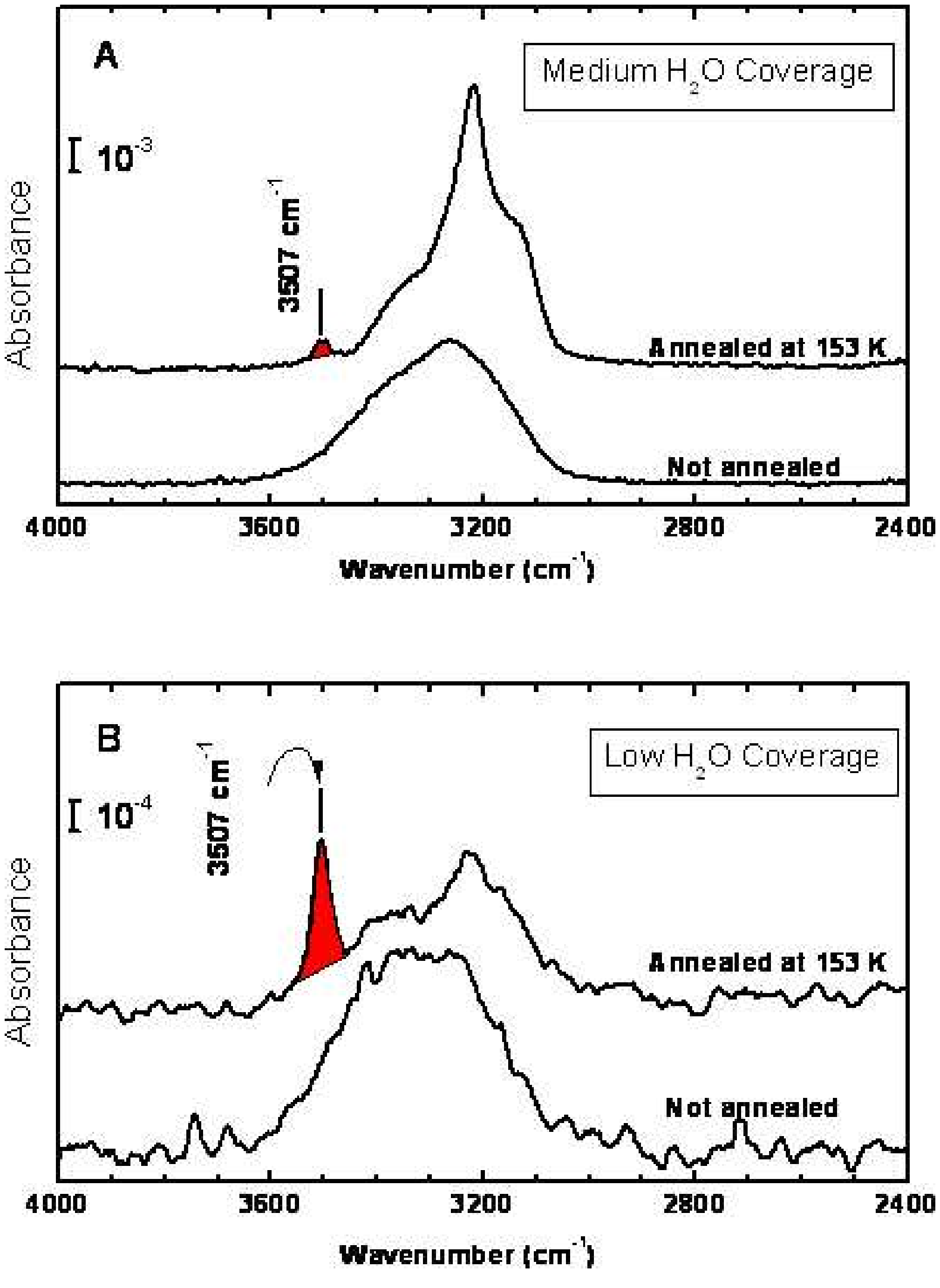

Figure 64: Appearance of the 3507 cm^{-1} OH stretching mode following diffusion of H_2O into the nanotube interior at medium (A) and low (B) coverages.

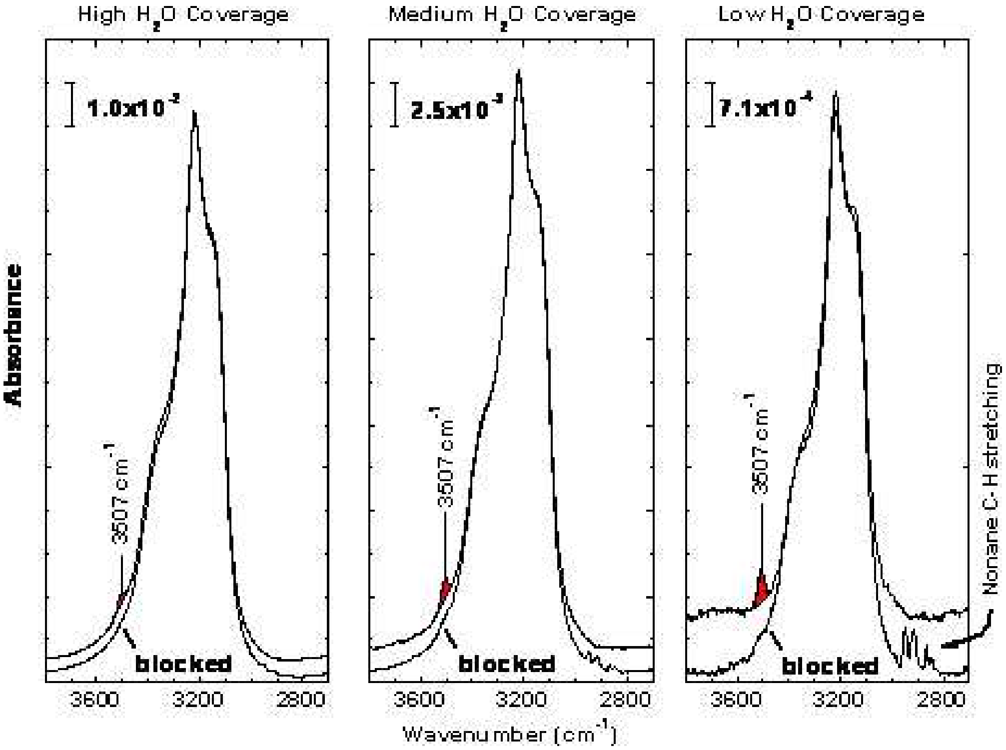

Figure 65: Changes in the IR spectra of H_2O condensed on single walled carbon nanotubes on heating in vacuum.

molecule in a cluster produces a red-shifted mode in the 3636-3657 cm^{-1} range.[181] We have computed the red-shift for a single H_2O inside a (10,10) SWNT using the VASP[206, 207, 208, 209] *ab initio* density functional theory (DFT) package. The maximum calculated shift is 30 cm^{-1}. We therefore conclude that only hydrogen bonding could cause the red-shift of the free OH frequency down to 3507 cm^{-1}, thereby excluding interactions of OH groups with the nanotube interior as being the cause of the 3507 cm^{-1} mode.

10.4.2 Theoretical Results

We have performed classical molecular simulations for water confined in SWNTs. We have also carried out quantum mechanical DFT calculations for water in ring structures in vacuum and inside a SWNT.

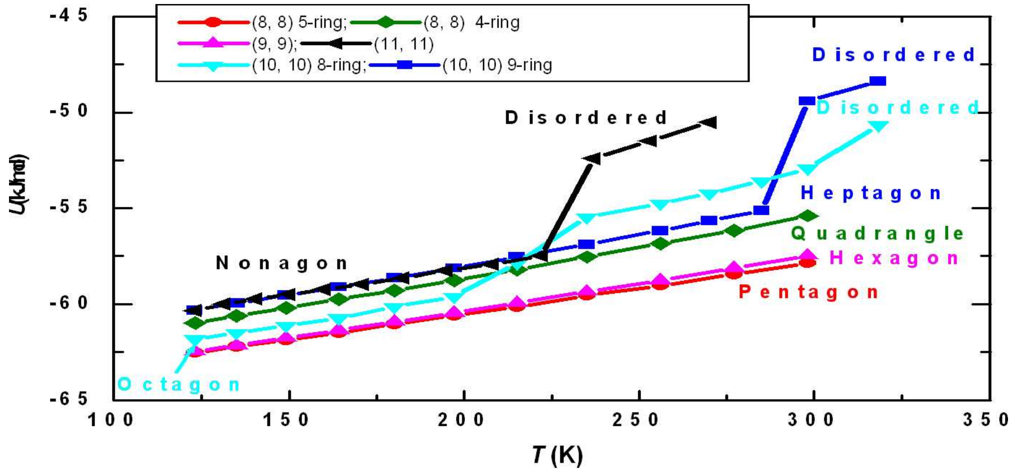

Figure 66: Average energy for water confined in (8, 8), (9, 9), (10, 10), and (11, 11) SWNTs at temperatures ranging from 123 to 318 K from parallel tempering NVT Monte Carlo simulations.

Classical molecular simulations were used to identify structural, energetic, and vibrational properties of water in SWNTs and in the bulk phase at low temperatures. Grand canonical Monte Carlo (GCMC) simulations[149] (Figure 60) were used to efficiently fill nanotubes with water at room temperature. We then performed parallel tempering Monte Carlo simulations[203] in the NVT ensemble over the temperature range from 123 K to 298

K (270 K and 318 K for (10, 10) and (11, 11) nanotubes, respectively) to identify equilibrium structures at low temperatures. The average energies for water confined in (8, 8), (9, 9), (10, 10), and (11, 11) SWNTs are shown in Figure 66. At low temperatures water forms stacked ring structures in all of the nanotubes considered. See, for example, the water structure in a (10,10) nanotube shown in Figure 67. The number of water molecules in a ring depends primarily on the diameter of the nanotube. However, the (8,8) and (10,10) nanotubes can support different polymorphs. Five- and four-membered rings are observed in the (8,8) nanotube, while the (10,10) nanotube can have both eight- and seven-membered rings, as shown in Figure 66. Order-to-disorder structural transitions, indicated by rapid rises in the potential energy with temperature (Figure 66), occur for water confined in (10,10) and (11,11) SWNTs; the water remains well-ordered in the smaller diameter nanotubes, even at 298 K. The nanotubes were filled at room temperature for computational efficiency. We have carried out an adsorption isotherm at 183 K for the (10,10) SWNT to verify that the same structure is ultimately obtained through GCMC simulations as was found from the parallel tempering simulations (see Figure 61). The same stacked ring structures were obtained in the 183 K GCMC simulations, but at a dramatically higher computational cost, as approach to equilibrium is very slow at that temperature.

The GCMC simulations at both high and low temperatures and those of Striolo et al.[216] indicate that partial filling of the nanotubes with water is not likely (see Figures 60 and 61). The isotherms indicate an abrupt transition from an empty nanotube to a filled nanotube, consisting of either stacked rings or amorphous water. The 183 K isotherm indicates that both seven- and eight-membered rings could be observed over the range of water vapor pressures likely to be encountered in the experiments. The number of free OH groups for water adsorbed in the nanotubes is not expected to be significant, given the complete filling observed for all nanotubes studied in this work.

The stacked ring structures observed in the nanotubes at low temperatures result in fully hydrogen bonded water networks. A snapshot of H_2O in a (10,10) nanotube at 123 K is shown in Figure 67. Figure 67A is an end-on view of the water in the nanotube, clearly showing the heptagon ring structure. The ring structures produce intra- and inter-ring hydrogen bonds. The stacked ring structure can be seen in Figure 67B. The oxygen atoms in H_2O are shown

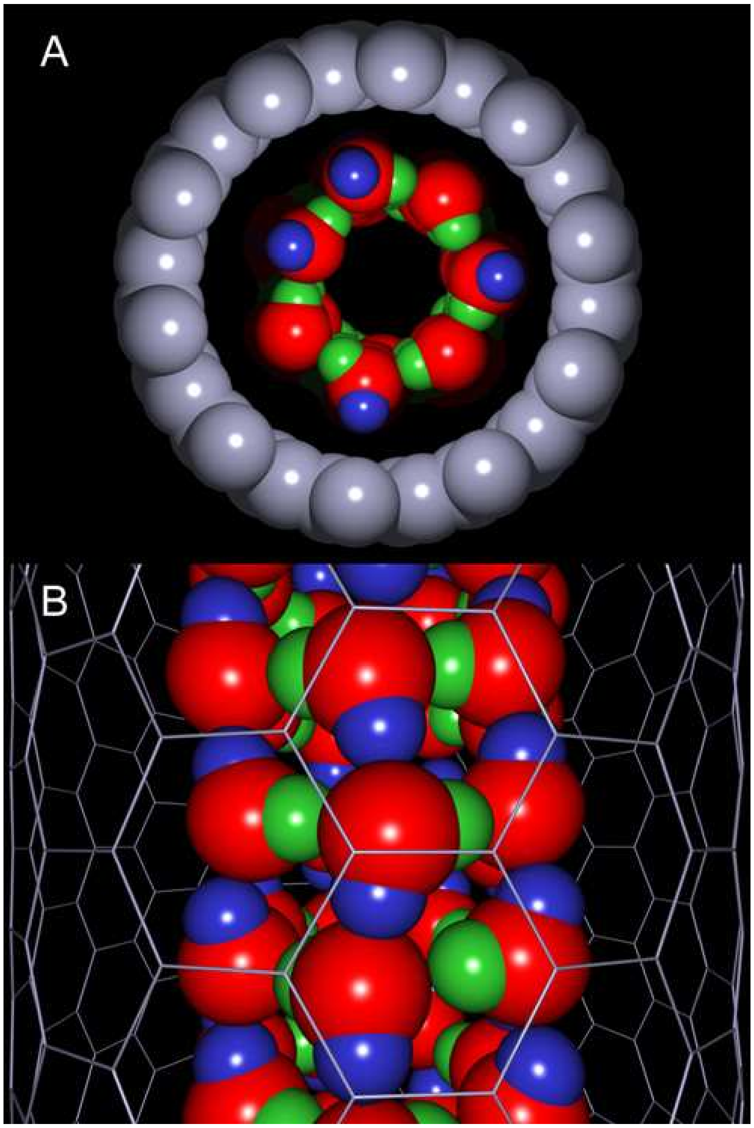

Figure 67: Snapshot from a molecular simulation of water adsorbed inside a (10, 10) SWNT at 123 K forming heptagon rings. (A) End view. (B) Side view. Red spheres represent oxygen atoms, blue spheres are hydrogens that are hydrogen bonded to adjacent rings (inter-ring), and green spheres are hydrogens involved in intra-ring hydrogen bonds. The lines in (B) represent the carbon-carbon bonds of the SWNT.

in red, the hydrogens participating in intra-ring hydrogen bonds are shown in green, and the inter-ring hydrogen bonded hydrogens are blue.

The intra-ring hydrogen bonds are bulk-like while most of the inter-ring hydrogen bonds are relatively weak, having a distorted geometry that gives rise to a distinct OH stretching mode. This is illustrated in Figure 68A, using the results of H_2O confined in a (10, 10) SWNT as an example; the distribution of hydrogen bond angles, measured as the O-OH angle, θ, are reported for bulk amorphous ice and heptagonal ring structured H_2O inside a (10,10) SWNT, both at 123 K. The probability density for amorphous ice (black line) has a single maximum at $\theta \approx 6^\circ$, whereas H_2O inside a (10,10) nanotube (red line) has a distribution of hydrogen bond angles that exhibits a maximum at $\theta \approx 5^\circ$ and a shoulder at higher angles. We have analyzed the inter- and intra-ring hydrogen bonds separately and found that the intra-ring hydrogen bond angles (dotted green line) are similar to those of bulk amorphous ice. However, the inter-ring hydrogen bond angles (blue dashed line) are very different from the bulk. The probability density $P(\theta)$ for inter-ring hydrogen bond angles has a Gaussian shape, with a maximum at about 17°. The unusually large hydrogen bond angles are caused by H_2O confinement in the nanotube.

We have analyzed the distribution of oxygen-oxygen distances, r_{OO}, as a surrogate for the hydrogen bond distances, for bulk and confined H_2O at 123 K. The probability densities, $P(r_{\mathrm{OO}})$, for bulk amorphous ice and for H_2O inside a (10,10) SWNT are plotted in Figure 68B and are seen to be very similar.

We have calculated IR spectra for bulk amorphous ice and water in different nanotubes from classical molecular dynamics (MD) simulations with a flexible water potential.[200] The results of our calculations are plotted in Figure 69.

The spectrum of bulk amorphous ice is much broader than the spectra for water inside nanotubes; the bulk modes are also shifted to lower frequencies. We note that the intensities calculated from classical MD do not capture the enhancement due to hydrogen bonding; however, the frequency distribution is expected to be qualitatively accurate. All of the calculated spectra for water in nanotubes are qualitatively similar and exhibit two distinct modes; the low-frequency and the high-frequency modes are due to intra-ring and inter-ring OH stretching, respectively, as will be demonstrated below. We deduce that the sharp IR

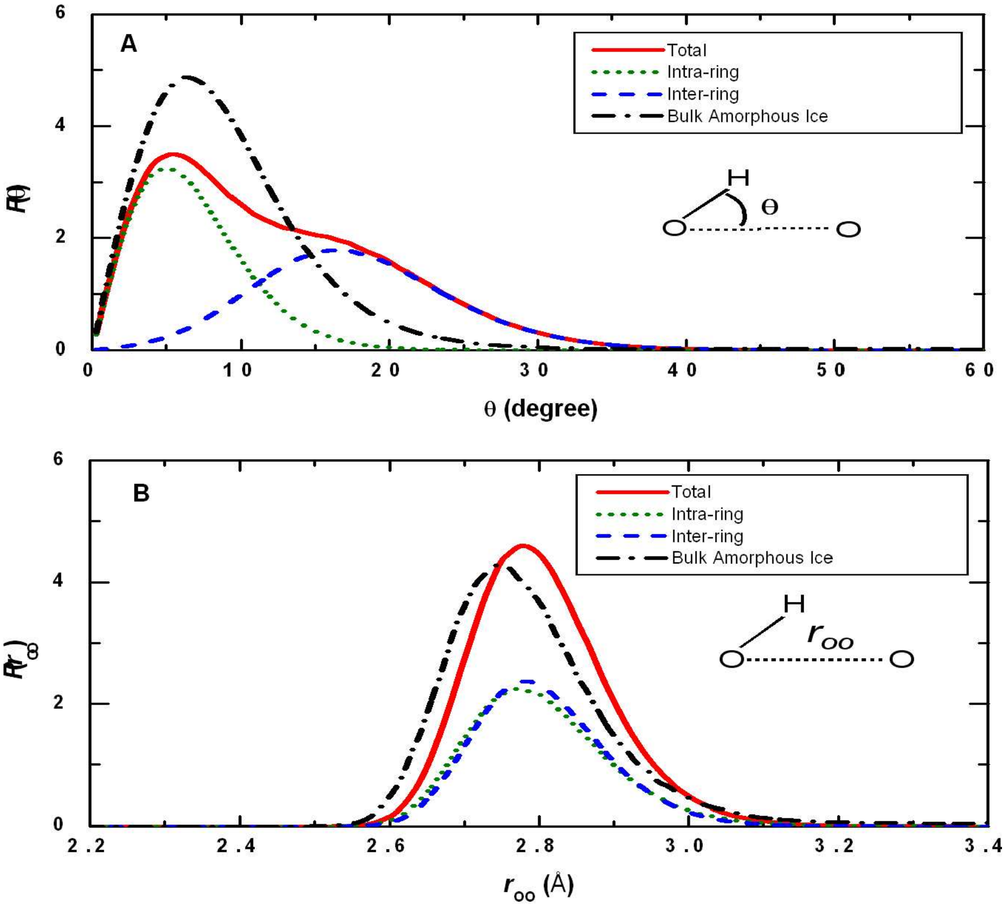

Figure 68: Characteristics of hydrogen bonding in amorphous ice and H_2O forming heptagonal rings inside a (10,10) SWNT computed from molecular simulations. (A) Hydrogen bond angle (O-OH) distribution computed from Monte Carlo simulation for bulk amorphous ice (dash-dot black line) and for H_2O in a (10,10) SWNT (solid red line). The intra-ring hydrogen bond angles are plotted as the dotted green line, the inter-ring hydrogen bond angles are represented by the dashed blue line, and the red line is the sum of the green and blue lines. The inset shows the definition of the O-OH angle θ. (B) Oxygen-oxygen distance, r_{OO}, distribution computed from Monte Carlo simulation for bulk amorphous ice (dash-dot black line) and for H_2O in a (10,10) SWNT (solid red line). The intra-ring O-O distances are plotted as the dotted green line, the inter-ring O-O distances are represented by the dashed blue line, and the red line is the sum of the green and blue lines. The inset shows the definition of the O-O distance r_{OO}.

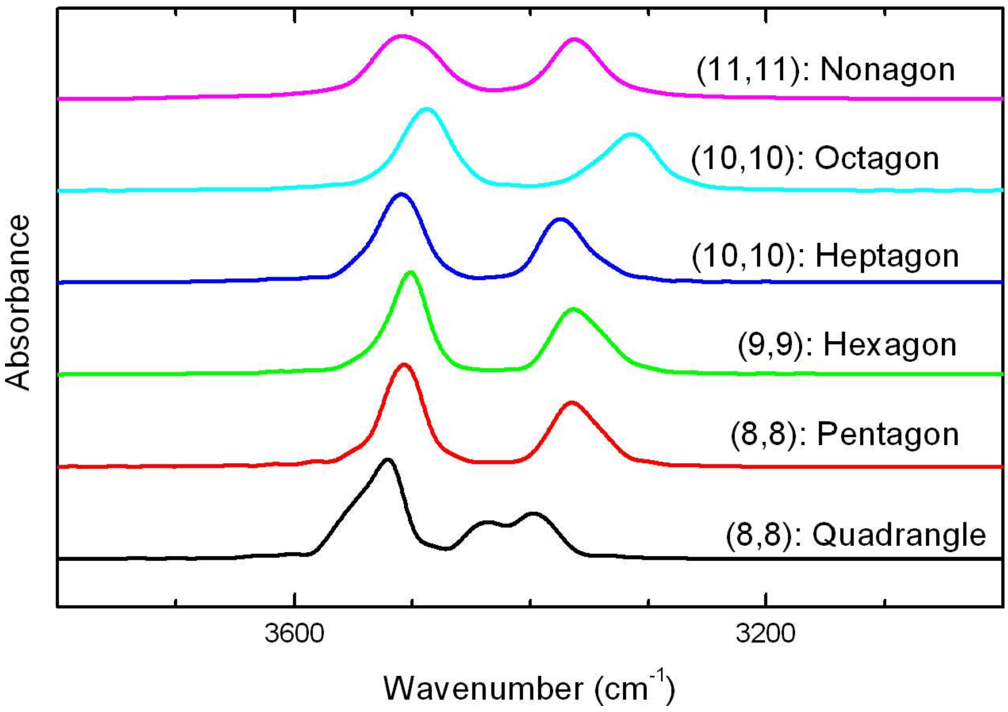

Figure 69: IR spectra for confined water in (8, 8), (9, 9), (10, 10), and (11, 11) SWNTs.

mode at 3507 cm^{-1} for H_2O inside the nanotubes, seen in Figures 63, 64, and 65 is generated by the unusual inter-ring hydrogen bonds. This assignment is verified by classical MD simulations and quantum mechanical DFT calculations. Flexible water potentials have been used previously to compute IR spectra of bulk and confined water from MD simulations.[173]

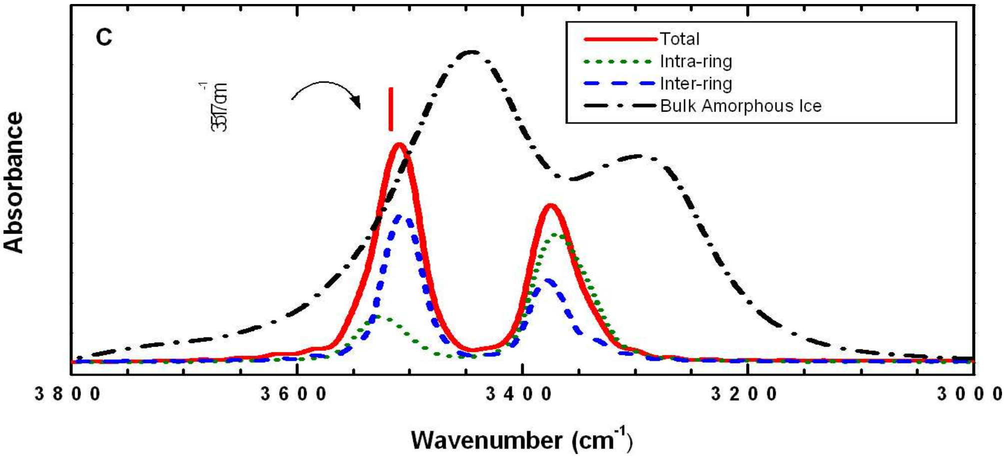

Figure 70: Vibrational spectra computed from molecular dynamics with a flexible water potential. The IR spectra for bulk amorphous ice is plotted as the dash-dot black line and the solid red line is for heptagon-water rings in a (10,10) SWNT. Note the presence of a 3517 cm^{-1} mode in good agreement with the experimentally observed 3507 cm^{-1} mode frequency. The IR spectrum computed for intra-ring OH stretching is plotted as the dotted green line and the inter-ring spectrum is the dashed blue line. Note that sum of the green and blue lines is not equal to the total spectrum (red line) because of cross correlations.

We have computed the IR spectrum for intra-ring OH and for inter-ring OH stretching separately. The results are presented in Figure 70. The dash-dotted black line is the spectrum of amorphous ice at 123 K and is in qualitative agreement with the spectrum for the non-annealed case in Figure 64. The solid red line in Figure 70 is the total IR spectrum for H_2O inside a (10,10) SWNT at 123 K. Two distinct modes are observed, one with a frequency of about 3370 cm^{-1}, which lies in the range of bulk hydrogen-bonded OH groups. The other mode is at about 3517 cm^{-1}, which corresponds closely with the experimentally observed mode at 3507 cm^{-1}. The mode at 3517 cm^{-1} is almost entirely due to inter-ring OH stretching (dashed blue line). Similar results are observed for water adsorbed in a (8, 8), (9, 9), and

(11, 11) SWNT and in different sizes of rings, both for the IR spectra (see Figure 69) and the bond angle distributions.

We have also computed vibrational frequencies and intensities for water in stacked rings from *ab initio* periodic DFT methods. We have used both the VASP[206, 207, 208, 209] and PWscf[212] packages. The DFT calculations confirm the features observed in the classical simulations. The IR spectrum for water in a stacked 5-member ring structure, as in the (8,8) SWNT, is plotted in Figure 71. The spectrum has been Lorentz broadened with a parameter of 5 cm^{-1}. The low frequency mode at 3174 cm^{-1} is due to intra-ring hydrogen bonding while the higher frequency mode at 3555 cm^{-1} is from OH groups involved in weaker inter-ring hydrogen bonds. These two modes are in agreement with the modes observed from classical MD simulations in Figures 69 and 70. Note that the DFT calculations are not expected to give frequencies that agree quantitatively with experiments. However, DFT can capture the enhancement of intensity for the stronger hydrogen bonded species (intra-ring modes), which the MD simulations cannot. The intensity of the lower frequency mode is about twice that of the higher frequency mode. This intensity enhancement is expected to be qualitatively, but not quantitatively correct.

The low-frequency modes in the experimental spectra for water inside nanotubes are very broad (see Figures 63, 64, and 65), while our simulated spectra have relatively sharp low-frequency peaks (Figures 69, 70, and 71). Much of the experimental broadening can be attributed to amorphous ice on the external surface of the sample. However, the low frequency mode in the spectra at low coverage (Figure 63) are also very broad. Furthermore, the intensity of these modes appears to be attenuated. There are two reasons for the apparent discrepancy between simulations and experiments. (1) The low-frequency (intra-ring) modes are inhomogeneously broadened because of the distribution of nanotube diameters in the experimental sample.[102] Both classical (see Figure 69) and quantum simulations confirm that the low-frequency modes are sensitive to the nanotube diameter while the high-frequency inter-ring modes are relatively insensitive to the diameter of the nanotube. (2) The nanotube bundles are predominantly aligned with their axes parallel to the plane of the tungsten grid and therefore perpendicular to the IR beam. This geometric arrangement constrains virtually all of the inter-ring O-H bonds to be perpendicular to the incident IR beam, while a substantial fraction of the intra-ring O-H bonds must be aligned nearly parallel to the IR beam. The geometry of the nanotube sample would therefore attenuate the low-frequency intra-ring mode because any bonds aligned nearly parallel to the IR beam would not add any intensity to the spectrum.

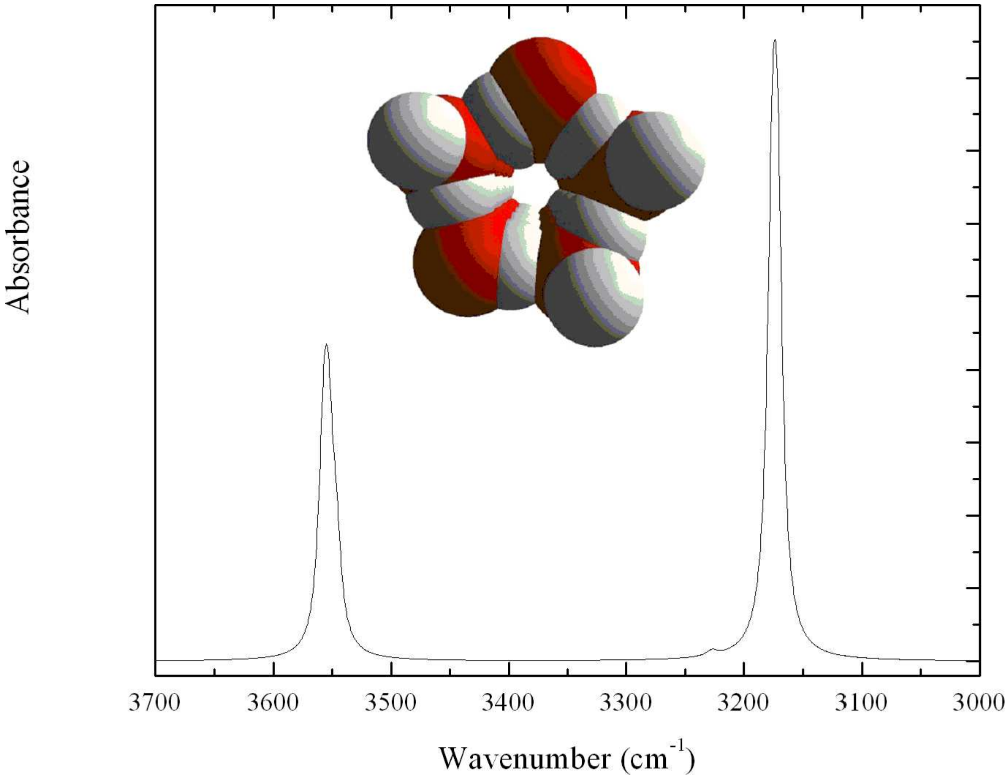

Figure 71: IR spectrum for a pentagonal ring ice structure computed from the PWscf package.[212] The feature at 3555 cm^{-1} is due to inter-ring O-H stretching while the mode at 3174 cm^{-1} is due to intra-ring O-H stretching.

10.5 SUMMARY

We have found that H_2O molecules confined inside of SWNTs form ring structures that involve hydrogen bonds of two types. Hydrogen bonds within the ring structure exhibit frequencies like those found in bulk H_2O and O-OH angles near 5 °. Hydrogen bonds formed between neighboring rings exhibit an unusual stretching frequency at 3507 cm^{-1} and are associated with larger O-OH angles near 17 $^\circ$. The strained angles and unusual IR mode are a direct result of the confinement-induced stacked ring structures, which would not be stable in the bulk. It is possible that water in other confined environments will exhibit similar distinct stretching frequencies, showing that IR spectroscopy, coupled with atomistic modeling, is proving to be a powerful tool for probing the structure and energetics of confined water.

11.0 FUTURE WORK

The new statistical simulation scheme and program that we developed seem to be promising for the simple spherical system. More functions are needed to be implemented into the program, such as dealing with complex molecules (polymer), electrostatic interaction calculations, parallel programming, etc. The goal of the program is direct simulation for CO_2-polymer phase behavior.

To obtain accurate thermodynamic properties of a system, very accurate inter-atomic interaction parameters are needed. *Ab initio* calculations have the ability to give highly accurate interaction energies for simple molecule system. The results from ab initio calculations can be used to develope the accurate potentials for statistical mechanical simulations. In addition, it will be interesting to know how important the accuracy is. Sample calculations can be performed with different set of potentials to investigate the effects of potentials on the phase behavior results.

Electrostatic interactions are very important for polar systems. There are different methods available to compute charges for model potentials in *ab initio* calculations. They are needed to be compared to find out which one gives the best results.

Molecular modeling guided CO_2-soluble polymer (or other interesting compounds) design is the ultimate goal of our simulation work for CO_2 and related molecules. We expect that the simulations can aid the experiments on screening the suitable molecules from hundreds and thousands of candidate molecules. Successful simulations will greatly reduce the time and expense of experimental work.

Experimental work has shown carbon nanotubes could be a promising materials for membranes. Hence, we need theoretical study for carbon nanotube diffusion characteristics to understand the diffusion mechanism. It will be interesting to learn how temperature, nanotube radius, nanotube chirality, molecular size, and hydrogen bond affect the diffusion in nanotube channels.

BIBLIOGRAPHY

[1] C. A. Eckert, B. L. Knutson, and P. G. Debenedetti. Supercritical fluids as solvents for chemical and materials processing. *Nature*, 373:313–318, 1996.

[2] J.M. DeSimone, Zihibin Guan, and C.S.Elsbernd. Synthesis of fluoropolymers in supercritical carbon dioxide. *Science*, 257:945–947, 1992.

[3] K. Harrison, J. Goveas, K. P. Johnston, and E. A. O'Rear. Water-in-carbon dioxide microemulsions with a fluorocarbon-hydrocarbon hybrid surfactant. *Langmuir*, 10:3536–3541, 1994.

[4] E. G. Ghenciu, A. J. Russell, E. J. Beckman, L. Steele, and N. T. Becker. Solubilization of subtilisin in CO_2 using fluoroether-functional amphiphiles. *Biotech. Bioeng.*, 58:572–580, 1998.

[5] K. P. Johnston and et al. Water in carbon dioxide microemulsions: An environment for hydrophiles including proteins. *Science*, 271:624–626, 1996.

[6] Traian Sarbu, Thomas J. Styranec, and Eric J. Beckman. Non-fluorous polymers with very high solubility in supercritical CO_2 down to low pressures. *Nature*, 405:165–168, 2000.

[7] Traian Sarbu, Thomas J. Styranec, and Eric J. Beckman. Design and synthesis of low cost, sustainable CO_2-philes. *Ind. Eng. Chem. Res.*, 39:4678–4683, 2000.

[8] F. Rindfleisch, T. P. DiNoia, and M. A. McHugh. Solubility of polymers and copolymers in supercritical CO_2. *J. Phys. Chem.*, 100:15581–15587, 1996.

[9] Z. Shen, M. A. McHugh, J. Xu, J. Belardi, S. Kilic, A. Mesiano, S. Bane, C. Karnikas, E. J. Beckman, and R. M. Enick. CO_2-solubility of oligomers and polymers that contain the carbonyl group. *Polymer*, 44:1491, 2003.

[10] V. V. Simonyan, J. K. Johnson, A. Kuznetsova, and J. T. Yates Jr. Molecular simulation of xenon adsorption on single-walled carbon nanotubes. *Journal of Chemical Physics*, 114:4180–4185, 2001.

[11] G. Stan and M. W. Cole. Low coverage adsorption in cylindrical pores. *Surface Science*, 395:280–291, 1998.

[12] L. D. Gelb, K. E. Gubbins, R. Radhakrishnan, and M. Sliwinska-Bartkowiak. Phase separation in confined systems. *Reports on Progress in Physics*, 62:1573–1659, 1999.

[13] S. Kilic, S. Michalik, Y. Wang, K. J. Johnson, R. M. Enick, and E. J. Beckman. Effect of grafted lewis base groups on the phase behavior of model poly(dimethyl siloxanes) in CO_2. *Ind. Eng. Chem. Res.*, 42:6415–6424, 2003.

[14] K. A. Consani and R. D. Smith. Observations on the solubility of surfactants and related molecules in carbon dioxide at 50 °C. *J. Supercrit. Fluids*, 3:51, 1990.

[15] C. F. Kirby and M. A. McHugh. Phase behavior of polymers in supercritical fluid solvents. *Chem. Rev.*, 99:565, 1999.

[16] J. F. Kauffman. Quadrupolar solvent effects on solvation and reactivity of solutes dissolved in supercritical CO_2. *J. Phys. Chem. A*, 105:3433, 2001.

[17] K. E. O'Shea, K. M. Kirmse, M. A. Fox, and K. P. Johnston. Plar and hydrogen-bonding interactions in supercritical fluids: Effects on the tautomeric equilibrium of 4-(phenylazo)-1-naphthol. *J. Phys. Chem.*, 95:7863, 1991.

[18] K. P. Johnston and R. M. Lemert. *Encyclopedia of Chemical Processing and Design.* J. J. McKetta and Ed. Dekker, New York, 1996.

[19] A. Francis. Ternary systems of liuid carbon dioxide. *J. Phys. Chem.*, 58:1099, 1954.

[20] J. A. Hyatt. Liquid and supercritical carbon dioxide as organic solvents. *J. Org. Chem.*, 49:5097, 1984.

[21] J. P. Heller, D. K. Dandge, R. J. Card, and L. G. Donaruma. Direct thickeners for mobility control of carbon dioxide floods. *Soc. Pet. Eng. J.*, 25:679, 1985.

[22] T. Hoefling, D. Stofesky, M. Reid, E. J. Beckman, and R. M. Enick. The incorporation of a fluorinated ether functionality into a polymer or surfactant to enhance carbon dioxide solubility. *J. Supercrit. Fluids*, 5:237, 1992.

[23] T. A. Hoefling, D. A. Newman, R. M. Enick, and E. J. Beckman. Effect of structure on the cloud-point curves of silicone-based amphiphiles in supercritical carbon dioxide. *J. Supercrit. Fluids*, 6:165, 1993.

[24] Richard D. Smith Geary G. Yee, John L. Fulton. Fourier transform infrared spectroscopy of molecular interactions of heptafluoro-1-butanol or 1-butanol in supercritical carbon dioxide and supercritical ethane. *J. Phys. Chem.*, 96:6172–6181, 1992.

[25] A. Dardin, J. M. DeSimone, and E. T. Samulski. Fluorocarbons dissolved in supercritical carbon dioxide. nmr evidence for specific solute-solvent interactions. *J. Phys. Chem. B*, 102:1775–1780, 1998.

[26] A. Cece, S. H. Jureller, J. L. Kerschner, and K. F. Moschner. Molecular modeling approach for contrasting the interaction of ethane and hexafluoroethane with carbon dioxide. *J. Phys. Chem.*, 100:7435–7439, 1996.

[27] Y. K. Han and H. Y. Jeong. Comment on "molecular modeling approach for contrasting the interaction of ethane and hexafluoroethane with carbon dioxide". *J. Phys. Chem. A.*, 101:5604–5604, 1997.

[28] P. Diep, K. D. Jordan, J. K. Johnson, and E. J. Beckman. CO_2-fluorocarbon and CO_2-hydrocarbon interactions from first-principles calculations. *J. Phys. Chem. A*, 102(12):2231–2236, 1998.

[29] P. T. Raveendran and S. L. Wallen. Exploring CO_2-philicity: Effects of stepwise fluorination. *J. Phys. Chem. B*, 107:1473–1477, 2003.

[30] J.R. Fried and N. Hu. The molecular basis of CO_2 interaction with polymers containing fluorinated groups: Computational chemistry of model compounds and molecular simulation of poly[bis(2,2,2-trifluoroethoxy)phosphazene]. *Polymer*, 44:4363–4372, 2003.

[31] Perfluorooctanoic acid (pfoa) and fluorinated telomers. http://www.epa.gov/oppt/pfoa/, 2006.

[32] S. G. Kazarian, M. F. Vincent, F. V. Bright, C. L. Lioota, and C. A. Eckert. Specific intermolecular interaction of carbon dioxide with polymers. *J. Am. Chem. Soc.*, 118:1729, 1996.

[33] Michael R. Nelson and Raymond F. Borkman. *Ab initio* calculation on CO_2 binding to carbonyl groups. *J. Phys. Chem. A*, 102:7860–7863, 1998.

[34] Poovathinthodiyil Raveendran and Scott L. Wallen. Cooperative C-H$\cdots$O hydrogen bonding in CO_2-lewis base complexes: Implications for solvation in supercritical CO_2. *J. Am. Chem. Soc.*, 124:12590–12599, 2002.

[35] Poovathinthodiyil Raveendran and Scott L. Wallen. Sugar acetates as novel, renewable CO_2-philes. *J. Am. Chem. Soc.*, 124:7274–7275, 2002.

[36] J. C. Meredith, K. P. Johnston, J. M. Seminario, S. G. Kazarian, and C. A. Eckert. Quantitative equilibrium constants between CO_2 and lewis bases from ftir spectroscopy. *J. Phys. Chem.*, 100:10837–10848, 1996.

[37] G. Luna-Barcenas, S. Mawson, S. Takishima, J. M. DeSimone, I. C. Sanchez, and K. P. Johnston. Phase behavior of poly(1,1-dihydroperfluorooctylacrylate) in supercritical carbon dioxide. *Fluid Phase Equilibria*, 146:325–337, 1998.

[38] M. Lora, F. Rindfleisch, and M. A. McHugh. Influence of the alkyl tail on the solubility of poly(alkyl acrylates) in ethylene and CO_2 at high pressures: Experiments and modeling. *Journal of Applied Polymer Science*, 73:1979–1991, 1999.

[39] M. Lora and M. A. McHugh. Phase behavior and modeling of the poly(methyl methacrylate)-CO_2-methyl methacrylate system. *Fluid Phase Equilibria*, 157:285–297, 1999.

[40] S. T. Cui, H. D. Cochran, and P. T. Cummings. Vapor-liquid phase coexistence of alkane carbon dioxide and perfluoroalkane carbon dioxide mixtures. *J. of Phys. Chem. B*, 103:4485–4491, 1999.

[41] Axel Gross and Matthias Scheffler. *Ab Initio* quantum and molecular dynamics of the dissociative adsorption of hydrogen on pd(100). *Phys. Rev. B*, 57:2493–2506, 1998.

[42] R. Car and M. Parrinello. Unified approach for molecular dynamics and denisty-functional theory. *Phys. Rev. Lett.*, 55:2471–2474, 1985.

[43] Paul A. Madden Dahlia K. Remler. Molecular dynamics without effective potentials via the car-parrinello approach. *Molecular Physics*, 70:921–966, 1990.

[44] T. A. Wesołowski. Comment on "anisotropic intermolecular interactions in van der waals and hydrogen-bonded complexes: what can we get from density functional calculations?" [j. chem. phys. 111, 7727(1999)]. *J. Chem. Phys.*, 113:1666–1667, 2000.

[45] X. Wu, M. C. Vargas, S. Nayak, V. Lotrich, and G. Scoles. Towards extending the applicability of density functional theory to weakly bound systems. *J. Chem. Phys.*, 115:8748–8757, 2001.

[46] A. J. Misquitta and K. Szalewicz. Intermolecular forces from asymptotically corrected density functional description of monomers. *Chem. Phys. Lett.*, 357:301–306, 2002.

[47] T. A. Wesołowski, P. Y. Morgantini, and J. Weber. Intermolecular interaction energies from the total energy bifunctional: A case study of carbazole complexes. *J. Chem. Phys.*, 116:6411–6421, 2002.

[48] A. Milet, T. Korona, R. Moszynski, and E. Kochanski. Anisotropic intermolecular interactions in van der waals and hydrogen-bonded complexes: what can we get from density functional calculations? *J. Chem. Phys.*, 111:7727–7735, 1999.

[49] M. Kamiya, T. Tsuneda, and K. Hirao. A density functional study of van der waals interactions. *J. Chem. Phys.*, 117:6010–6015, 2002.

[50] T. van Mourik and R. J. Gdanitz. A critical note on density functional theory studies on rare-gas dimers. *J. Chem. Phys.*, 116:9620–9623, 2002.

[51] W. Kohn, Y. Meir, and D. E. Makarov. van der waals energies in density functional theory. *Phys. Rev. Lett.*, 80:4153–4156, 1998.

[52] Seiji Tsuzuki, Tadafumi Uchimaru, Kazunari Matsumura, Masuhiro Mikami, and Kazutoshi Tanabe. Effects of the higher electron correlation correction on the calculated intermolecular interaction energies of benzene and naphthalene dimers: com-

parison between MP2 and CCSD(T) calculations. *Chemical Physics Letters*, 319:547, 2000.

[53] Pavel Hobza, Heinrich L. Selzle, and Edward W. Schlag. Potential energy surface for the benzene dimer. results of *ab Initio* CCSD(T) calculations show two nearly isoenergetic structures: T-shaped and parallel-displaced. *J. Phys. Chem.*, 100:18790, 1996.

[54] D. E. Woon, K. A. Peterson, and T. H. Dunning. Benchmark calculations with correlated molecular wave functions. ix. the weakly bound complexes, Ar-H_2 and Ar-HCl. *J. Chem. Phys.*, 109:2233–2241, 1998.

[55] A. K. Rappé and E. R. Bernstein. *Ab initio* calculation of nonbonded interactions: Are we there yet? *J. Phys. Chem. A*, 104:6117–6128, 2000.

[56] J. Marc Pedulla, Fernando Vila, and K. D. Jordan. Binding energy of the ring form of $(H_2O)_6$: Comparison of the predictions of conventional and localized-orbital MP2 calculations. *J. Chem. Phys.*, 105:11091, 1996.

[57] R. A. Christie and K. D. Jordan. Theoretical investigation of the $H_3O{+}(H_2O)_4$ cluster. *J. Phys. Chem.*, 105:7551, 2001.

[58] P. Hobza and Z. Havlas. Counterpoise-corrected potential energy surfaces of simple h-bonded systems. *Theoretical Chemistry Accounts*, 99:372, 1998.

[59] S. F. Boys and F. Bernardi. The calculation of small molecular interactions by the differences of separate total energies. Some procedures with reduced errors. *Mol. Phys.*, 19:553–566, 1970.

[60] M. J. Frisch, G. W. Trucks, H. B. Schlegel, G. E. Scuseria, M. A. Robb, J. R. Cheeseman, V. G. Zakrzewski, J. A. Montgomery Jr., R. E. Stratmann, J. C. Burant, S. Dapprich, J. M. Millam, A. D. Daniels, K. N. Kudin, M. C. Strain, O. Farkas, J. Tomasi, V. Barone, M. Cossi, R. Cammi, B. Mennucci, C. Pomelli, C. Adamo, S. Clifford, J. Ochterski, G. A. Petersson, P. Y. Ayala, Q. Cui, K. Morokuma, P. Salvador, J. J. Dannenberg, D. K. Malick, A. D. Rabuck, K. Raghavachari, J. B. Foresman, J. Cioslowski, J. V. Ortiz, A. G. Baboul, B. B. Stefanovand G. Liu, A. Liashenko, P. Piskorz, I. Komaromi, R. Gomperts, R. L. Martin, D. J. Fox, T. Keith, M. A. Al-Laham, C. Y. Peng, A. Nanayakkara, M. Challacombeand P. M. W. Gill, B. Johnson, W. Chen, M. W. Wong, Andres, C. Gonzalez, M. Head-Gordon, E. S. Replogle, and J. A. Pople. Gaussian 98, Revision A. 11, 2001.

[61] T. Helgaker, W. Klopper, H. Koch, and J. Noga. Basis-set convergence of correlated calculatins on water. *J. Chem. Phys.*, 106:9639, 1997.

[62] David Feller and K. D. Jordan. Estimating the strength of the water/single-layer graphite interaction. *J. Phys. Chem. A.*, 104:9971–9975, 2000.

[63] M. J. Frisch, G. W. Trucks, H. B. Schlegel, G. E. Scuseria, M. A. Robb, J. R. Cheeseman, J. A. Montgomery Jr., T. Vreven, K. N. Kudin, J. C. Burant, J. M. Millam, S. S. Iyengar, J. Tomasi, V. Barone, B. Mennucci, M. Cossi, G. Scalmani, N. Rega, G. A. Petersson, H. Nakatsuji, M. Hada, M. Ehara, K. Toyota, R. Fukuda, J. Hasegawa, M. Ishida, T. Nakajima, Y. Honda, O. Kitao, H. Nakai, M. Klene, X. Li, J. E. Knox, H. P. Hratchian, J. B. Cross, C. Adamo, J. Jaramillo, R. Gomperts, R. E. Stratmann, O. Yazyev, A. J. Austin, R. Cammi, C. Pomelli, J. W. Ochterski, P. Y. Ayala, K. Morokuma, G. A. Voth, P. Salvador, J. J. Dannenberg, V. G. Zakrzewski, S. Dapprich, A. D. Daniels, M. C. Strain, O. Farkas, D. K. Malick, A. D. Rabuck, K. Raghavachari, J. B. Foresman, J. V. Ortiz, Q. Cui, A. G. Baboul, S. Clifford, J. Cioslowski, B. B. Stefanov, G. Liu, A. Liashenko, P. Piskorz, I. Komaromi, R. L. Martin, D. J. Fox, T. Keith, M. A. Al-Laham, C. Y. Peng, A. Nanayakkara, M. Challacombe, P. M. W. Gill, B. Johnson, W. Chen, M. W. Wong, C. Gonzalez, and J. A. Pople. Gaussian 03, Revision B. 01, 2003.

[64] Bilal Baradie, Molly S. Shoichet, Zhihua Shen, Mark McHugh, Lei Hong, Yang Wang, J. Karl Johnson, Eric J. Beckman, and Robert M. Enick. Synthesis and solubility of linear poly(tetrafluoroethylene-co-vinyl acetate) in dense CO_2: Experimental and molecular modeling results. *Macromolecules*, 37:7799–7807, 2004.

[65] Sevgi Kilic, Stephen Michalik, Yang Wang, J. Karl Johnson, Robert M. Enick, and Eric J. Beckman. CO_2-miscibility of the polymers possessing ether oxygen. *Macromolecules*, accepted, 2006.

[66] M. A. Blatchford, P. Raveendran, and S. L. Wallen. Spectroscopic studies of model carbonyl compounds in CO_2: Evidence for cooperative C-H$\cdots$O interactions. *J. Phys. Chem. A*, 107:10311–10323, 2003.

[67] P. Van Ginderen, W. A. Herrebout, and B. J. van der Veken. van der waals complex of dimethyl ether with carbon dioxide. *J. Phys. Chem. A*, 107:5391–5396, 2003.

[68] Y. Danten, T. Tassaing, and M. Besnard. Vibrational spectra of CO_2-electron donor-accepter complexes from *ab initio*. *J. Phys. Chem. A*, 106:11831–11840, 2002.

[69] D. W. van Krevelen. *Properties of Polymers*. Elsevier Science Publishers, Netherlands, 1990.

[70] C. Drohman and E. J. Beckman. Phase behavior of polymers containing ether groups in carbon dioxide. *J. Supercrit. Fluids*, 22:103, 2002.

[71] G. R. Desiraju. The C-H$\cdots$O hydrogen bond: Structural implications and supramolecular design. *Accounts of Chemical Research*, 29:441, 1996.

[72] Yang Wang, Lei Hong, Inchul Kim, Jacob Crosthwaite, Andy Hamilton, Mark Thies, Eric J. Beckman, Robert M. Enick, and J. Karl Johnson. Design and evaluation of non-fluorous CO_2-soluble polymers, 2006.

[73] X. Fan, V. K. Potluri, M. C. McLeod, Y. Wang, J. C. Liu, R. M. Enick, A. D. Hamilton, C. B. Roberts, J. K. Johnson, and E. J. Beckman. Oxygenated hydrocarbon ionic surfactants exhibit CO_2 solubility. *Journal of American Chemical Society*, 127:11754–11762, 2005.

[74] J. Eastoe, S. Gold, S. Rogers, P. Wyatt, D. C. Steytler, A. H. Gurgel, R. K. Heenan, X. Fan, E. J. Beckman, and R. M. Enick. Designed CO_2-philes stabilize water-in-carbon dioxide microemulsions. *Angewandte Chemie-international Edition*, 45:3675–3677, 2006.

[75] J. DeSimone. *U.S. Patent*, 5496901, 1996.

[76] J. DeSimone, Z. Guan, J. Combes, and Y. Menceloglu. *Macromolecules*, 26:2663, 1993.

[77] L. Hong. *Identification, design and synthesis of oxygenated hydrocarbon-based CO_2-soluble polymers for chemical and petroleum engineering applications.* University of Pittsburgh, 2006.

[78] S. Kilic. *Engineering of Polymers to Thicken Carbon Dioxide: A Systematic Approach.* University of Pittsburgh, 2003.

[79] T. H. Dunning Jr. *Journal of Chemistry Physics*, 90:1007, 1989.

[80] J. P. Foster and F. Weinhold. Natural hybrid orbitals. *Journal of American Chemical Society*, 102:7211–7218, 1980.

[81] Manfred Schlosser. Parametrization of substituents: Effects of fluorine and other heteroatoms on oh, nh, and ch acidities. *Angewandte Chemie-international Edition*, 37:1496–1613, 1998.

[82] V. K. Potluri, A. D. Hamilton, C. F. Karanikas, S. E. Bane, J. Xu, E. J. Beckman, and R. M. Enick. The high CO_2-solubility of per-acetylated alpha-, beta-, and gamma-cyclodextrin. *Fluid Phase Equilibria*, 211:211–217, 2003.

[83] M. L. O'Neill, Q. Cao, M. Fang, K. P. Johnston, S. P. Wilkinson, C. D. Smith, J. L. Kerschner, and S. H. Jureller. Solubility of homopolymers and copolymers in carbon dioxide. *Ind. Eng. Chem. Res.*, 37:3067–3079, 1998.

[84] P. Kondratyuk, Y. Wang, J. K. Johnston, and J. T. Yates Jr. Observation of a one-dimensional adsorption site on carbon nanotubes: Adsorption of alkanes of different molecular lengths. *Journal of Physical Chemistry B*, 109:20999–21005, 2005.

[85] X. Fan, E. C. Dickey, P. C. Eklund, K. A. Williams, L. Grigorian, R. Buczko, S. T. Pantelides, and S. J. Pennycook. *Physical Review Letters*, 84:4621–4624, 2000.

[86] Christopher Matranga, Liang Chen, Milton Smith, Edward Bittner, J. Karl Johnson, and Bradley Bockrath. Trapped CO_2 in carbon nanotube bundles. *J. Phys. Chem. B*, 107:12930–12941, 2003.

[87] S. Talapatra and A. D. Migone. Existence of novel quasi-one-dimensional phases of atoms adsorbed on the exterior surface of close-ended single wall nanotube bundles. *Phys. Rev. Lett.*, 87:206106, 2001.

[88] H. Ulbricht, G. Moos, and T. Hertel. *Phys. Rev. Lett.*, 90:095501, 2003.

[89] Z. J. Jakubek and B. Simard. *Langmuir*, 20:5940–5945, 2004.

[90] M. R. Babaa, N. Dupont-Pavlovsky, E. McRae, and K. Masenelli-Varlot. *Carbon*, 42:1549–1554, 2004.

[91] O. Byl, P. Kondratyuk, S. T. Forth, S. A. FitzGerald, L. Chen, J. K. Johnson, and J. T. Yates Jr. *J. Am. Chem. Soc.*, 125:5889–5896, 2003.

[92] A. Kuznetsova, J. T. Yates, Jr., J. Liu, and R. E. Smalley. Physical adsorption of xenon in open single walled carbon nanotubes: Observation of a quasi-one-dimensional confined Xe phase. *J. Chem. Phys.*, 112:9590–9598, 2000.

[93] A. Kuznetsova, D. B. Mawhinney, V. Naumenko, J. T. Yates, Jr., J. Liu, and R. E. Smalley. Enhancement of adsorption inside of single-walled nanotubes: opening the entry ports. *Chem. Phys. Lett.*, 321:292–296, 2000.

[94] A. Kuznetsova, J. T. Yates, Jr., V. V. Simonyan, J. K. Johnson, C. B. Huffman, and R. E. Smalley. Optimization of Xe adsorption kinetics in single walled carbon nanotubes. *J. Chem. Phys.*, 115:6691–6698, 2001.

[95] K. M. A. De Meyer, S. Chempath, J. F. M. Denayer, J. A. Martens, R. Q. Snurr, and G. V. Baron. *J. Phys. Chem. B*, 107:10760–10766, 2003.

[96] M. S. Sun, O. Talu, and D. B. Shah. *J. Phys. Chem. B*, 100:17276–17280, 1996.

[97] B. Millot, A. Methivier, and H. Jobic. *J. Phys. Chem. B*, 102:3210–3215, 1998.

[98] R. E. Richards and L. V. C. Rees. *Langmuir*, 3:335–340, 1987.

[99] W. Zhu, F. Kapteijn, B. van der Linden, and J. A. Moulijn. *Phys. Chem. Chem. Phys.*, 3:1755–1761, 2001.

[100] A. Thess, R. Lee, P. Nilolaev, H. Dai, P. Petit, J. Robert, C. Xu, Y. H. Lee, S. G. Kim, A. G. Rinzler, D. T. Colbert, G. E. Scuseria, D. Tománek, J. E. Fischer, and R. E. Smalley. *Science*, 273:483–487, 1996.

[101] T. Guo, P. Nikolaev, A. Thess, D. T. Colbert, and R. E. Smalley. *Chem. Phys. Lett.*, 243:49–54, 1995.

[102] A. G. Rinzler, J. Liu, H. Dai, P. Nikolaev, C. B. Huffman, F. J. Rodríguez-Macías, P. J. Boul, A. H. Lu, D. Heymann, D. T. Colbert, R. S. Lee, J. E. Fischer, A. M.

Rao, P. C. Eklund, and R. E. Smalley. Large-scale purification of single-wall carbon nanotubes: Process, product, and characterization. *Appl. Phys. A*, 67:29–37, 1998.

[103] P. Kondratyuk and J. T. Yates Jr. Desorption kinetic detection of different adsorption sites on opened carbon single walled nanotubes: The adsorption of n-nonane and CCl_4. *Chem. Phys. Lett.*, 410:324–329, 2005.

[104] P. Kondratyuk and J. T. Yates Jr. Nanotubes as molecular sponges: the adsorption of CCl_4. *Chem. Phys. Lett.*, 383:314–316, 2004.

[105] M. J. Bozack, L. Muehlhoff, J. N. Russell Jr., W. J. Choyke, and J. T. Yates Jr. *J. Vac. Sci. Technol. A*, 5:1–8, 1987.

[106] A. Winkler and J. T. Yates Jr. *J. Vac. Sci. Technol. A*, 6:2929–2932, 1988.

[107] S. Duane, A. D. Kennedy, B. J. Pendleton, and D. Roweth. *Phys. Lett. B*, 195:216–222, 1987.

[108] Y. Chen A. Brass, B. J. Pendleton and B. Robson. Hybrid monte carlo simulations theory and initial comparison with molecular dynamics. *Biopolymers*, 33:1307–1315, 1993.

[109] C. J. Stirling M. E. Clamp, P. G. Baker and A. Brass. Hybrid monte carlo: An effficient algorithm for condensed matter simulation. *Journal of Computational Chemistry*, 15:838–846, 1994.

[110] Darryl D. Humphreys, Richard A. Friesner, and Bruce J. Berne. A multiple-time-step molecular dynamics algorithm for macromolecules. *J. Phys. Chem.*, 98:6885–6892, 1994.

[111] W. Shi and J. K. Johnson. Gas adsorption on heterogeneous single-walled carbon nanotube bundles. *Phys. Rev. Lett.*, 91:015504, 2003.

[112] W. A. Steele. *Surf. Sci.*, 36:317–352, 1973.

[113] M. G. Martin and J. I. Siepmann. *J. Phys. Chem. B*, 102:2569–2577, 1998.

[114] M. G. Martin and J. I. Siepmann. *J. Phys. Chem. B*, 103:4508–4517, 1999.

[115] Petro Kondratyuk, Yang Wang, Jiuchen Liu, J. Karl Johnson, and John T. Yates Jr. Inter- and intra-tube self-diffusion in n-heptane adsorbed on carbon nanotubes, 2006.

[116] S. Jakobtorweihen, M. G. Verbeek, C. P. Lowe, F. J. Keil, and B. Smit. Understanding the loading dependence of self-diffusion in carbon nanotubes. *Phys. Rev. Lett.*, 95:044501, 2005.

[117] D. P. Cao and J. Z. Wu. Self-diffusion of methane in single-walled carbon nanotubes at sub- and supercritical conditions. *Langmuir*, 20:3759–3765, 2004.

[118] V. P. Sokhan, D. Nicholson, and N. Quirke. Phonon spectra in model carbon nanotubes. *J. Chem. Phys.*, 113:2007–2015, 2000.

[119] A. I. Skoulidas, D. M. Ackerman, J. Karl Johnson, and David S. Sholl. Rapid transport of gases in carbon nanotubes. *Phys. Rev. Lett.*, 89:185901, 2002.

[120] A. Marmier, H. Spohr, D. J. Cooke, S. Kerisit, J. P. Brodholt, P. B. Wilson, and S. C. Parker. Self diffusion of argon in flexible, single wall, carbon nanotubes. *Molecular Simulation*, 31:385–389, 2005.

[121] J. Martí and M. C. Gordillo. Time-dependent properties of liquid water isotopes adsorbed in carbon nanotubes. *Journal of Chemical Physics*, 114:10486–10492, 2001.

[122] H. Ulbricht, J. Kriebel, G. Moos, and T. Hertel. Desorption kinetics and interaction of Xe with single-wall carbon nanotube bundles. *Chemical Physics Letters*, 363:252–260, 2002.

[123] A. Gutsze, W. Masierak, B. Geil, D. Kruk, H. Pahlke, and F. Fujara. On the problem of field-gradient nmr measurements of intracrystalline diffusion in small crystallites - water in naa zeolites as an example. *Solid State Nuclear Magnetic Resonance*, 28:244–249, 2005.

[124] F. Leroy and B. Rousseau. Self-diffusion of n-alkanes in mfi type zeolite using molecular dynamics simulations with an anisotropic united atom (AUA) forcefield. *Molecular Simulation*, 30:617–620, 2004.

[125] D. E. Favre, D. J. Schaefer, S. M. Auerbach, and B. F. Chmelka. Direct measurement of intercage hopping in strongly adsorbing guest-zeolite systems. *Physical Review Letters*, 81:5852–5855, 1998.

[126] E. von Meerwall, R. Ozisik, W. L. Mattice, and P. M. Pfister. Self-diffusion of linear and cyclic alkanes, measured with pulsed-gradient spin-echo nuclear magnetic resonance. *Journal of Chemical Physics*, 118:3867–3873, 2003.

[127] O. Geier, S. Vasenkov, D. Freude, and J. Karger. Pfg nmr observation of an extremely strong dependence of the ammonia self-diffusivity on its loading in H-ZSM-5. *Journal of Catalysis*, 213:321–323, 2003.

[128] D. Schuring, A. P. J. Jansen, and R. A. van Santen. Concentration and chainlength dependence of the diffusivity of alkanes in zeolites studied with md simulations. *Journal of Physical Chemistry B*, 104:941–948, 2000.

[129] F. Stallmach, J. Karger, C. Krause, M. Jeschke, and U. Oberhagemann. Evidence of anisotropic self-diffusion of guest molecules in nanoporous materials of mcm-41 type. *Journal of the American Chemical Society*, 122:9237–9242, 2000.

[130] M. Goddard and D. M. Ruthven. *Zeolites*, 6:445, 1986.

[131] M. Goddard and D. M. Ruthven. *Zeolites*, 6:283, 1986.

[132] P. Lorentz, M. Bulow, and J. Karger. *Cooloids and Surfaces*, 11:353, 1984.

[133] H. Jobic, A. N. Fitch, and J. Combet. Diffusion of benzene in nax and nay zeolites studied by quasi-elastic neutron scattering. *Journal of Physical Chemistry B*, 104:8491–8497, 2000.

[134] David M. Ackerman, Anastasios I. Skoulidas, David S. Sholl, and J. Karl Johson. Diffusivities of ar and ne in carbon nanotubes. *Molec. Sim.*, 29:677–684, 2003.

[135] Haibin Chen and David S. Sholl. Rapid diffusion of CH_4/H_2 binary mixtures in carbon nanotubes. *J. Am. Chem. Soc.*, 126:7778–7779, 2004.

[136] Z. G. Mao and S. B. Sinnott. A computational study of molecular diffusion and dynamic flow through carbon nanotubes. *J. Phys. Chem. B*, 104:4618–4624, 2000.

[137] S. Supple and N. Quirke. Rapid imbibition of fluids by carbon nanotubes. *Phys. Rev. Lett.*, 90:214501, 2003.

[138] S. Supple and N. Quirke. Molecular dynamics of transient oil flows in nanopores i: Imbibition speeds for signle wall carbon nanotubes. *Journal of Chemical Physics*, 121:8571–8579, 2004.

[139] S. Jakobtorweihen, C. P. Lowe, F. J. Keil, and B. Smit. A novel algorithm to model the influence of host lattice flexibility in molecular dynamics simulations–loading dependence of self-diffusion in carbon nanotubes. *J. Chem. Phys.*, submitted, 2006.

[140] R. Krishna and J. M. van Baten. Describing binary mixture diffusion in carbon nanotubes with the maxwell-stefan equations. an investigation using molecular dynamics simulations. *Ind. Eng. Chem. Res.*, 45:2084–2093, 2006.

[141] Anastasios I. Skoulidas and David S. Sholl. Transport diffusivities of CH_4, CF_4, He, Ne, Ar, Xe, and SF_6 in silicalite from atomistic simulations. *J. Phys. Chem. B*, 106:5058–5067, 2002.

[142] A. I. Skoulidas, David S. Sholl, and J. Karl Johnson. Adsorption and diffusion of carbon dioxide and nitrogen through single-walled carbon nanotube membranes. *J. Chem. Phys.*, 124:054708, 2006.

[143] Haibin Chen, D. S. Sholl, and J. K. Johnson. Transport diffusion of gasses is rapid in flexible carbon nanotubes. *J. Phys. Chem. B*, in press, 2006.

[144] S. A. Chesnokov, V. A. Nalimova, A. G. Rinzler, R. E. Smalley, and J. E. Fischer. Mechanical energy storage in carbon nanotube springs. *Physical Review Letters*, 82:343–346, 1999.

[145] P. Kondratyuk and J. T. Yates Jr. *J. Vac. Sci. Technol. A*, 23:215–217, 2005.

[146] E. J. Maginn, A. T. Bell, and D. N. Theodorou. Transport diffusivity of methane in silicalite from equilibrium and non-equilibrium simulations. *Journal of Physical Chemistry*, 97:4173–4181, 1993.

[147] D. N. Theodorou, R. Q. Snurr, and A. T. Bell. *Molecular Dynamics and diffusion in microporous materials*, volume 7. Pergamon Press, New York, 1996. G. Alberti and T. Bein, Book title=Comprehensive Supramolecular Chemistry.

[148] Glenn J. Martyna, Mark E. Tuckerman, Douglas J. Tobias, and Michael L. Klein. Explicit reversible integrators for extended systems dynamics. *Molecular Physics*, 87:1117–1157, 1996.

[149] M. P. Allen and D. J. Tildesley. *Computer Simulation of Liquids.* Oxford University Press, New York, 1987.

[150] M. G. Martin. http://towhee.sourceforge.net/.

[151] J. I. Siepmann and D. Frenkel. Configurational bias monte carlo: a new sampling scheme for flexible chains. *Mol. Phys.*, 75:59–70, 1992.

[152] S. L. Tait, Z. Dohnalek, C. T. Campbell, and B. D. Kay. *n*-alkanes on mgo(100). i. coverage-dependent desorption kinetics of *n*-butane. *Journal of Chemical Physics*, 122:164707, 2005.

[153] J. Crank. *Mathematics of Diffusion.* University Press, Oxford, 1957.

[154] A. J. Bard and L. R. Faulkner. *Electrochemical Metods.* John Wiley & Sons, New York, 1980.

[155] Dean C. Douglass and David W. McCall. Diffusion in paraffin hydrocarbons. *Journal of Physical Chemistry*, 62:1102–1107, 1958.

[156] K. R. Paserba and A. J. Gellman. Effects of conformational isomerism on the desorption kinetics of *n*-alkanes from graphite. *Journal of Chemical Physics*, 115:6737–6751, 2001.

[157] K. R. Paserba and A. J. Gellman. Kinetics and energetics of oligomer desorption from surfaces. *Phys. Rev. Lett.*, 86:4338–4341, 2001.

[158] Oleg Byl, Jiuchen Liu, Yang Wang, Wai-Leung Yim, J. karl Johnson, and John T. Yates Jr. Unusual hydrogen bonding in water-filled carbon nanotubes. *J. Am. Chem. Soc.*, 128:12090–12097, 2006.

[159] Victoria Buch and J. Paul Devlin. *Water in confining geometries.* Springer, Berlin, New York, 2003.

[160] K. Koga, G. T. Gao, H. Tanaka, and X. C. Zeng. Formation of ordered ice nanotubes inside carbon nanotubes. *Nature*, 412:802–805, 2001.

[161] G. Hummer, J. C. Rasaiah, and J. P. Noworyta. Water conduction through the hydrophobic channel of a carbon nanotube. *Nature*, 414:188–190, 2001.

[162] W. H. Noon, K. D. Ausman, R. E. Smalley, and J. P. Ma. Helical ice-sheets inside carbon nanotubes in the physiological condition. *Chemical Physics Letters*, 355:445–448, 2002.

[163] A. I. Kolesnikov, J. M. Zanotti, C. K. Loong, P. Thiyagarajan, A. P. Moravsky, R. O. Loutfy, and C. J. Burnham. Anomalously soft dynamics of water in a nanotube: A revelation of nanoscale confinement. *Phys. Rev. Lett.*, 93:035503, 2004.

[164] R. J. Mashl, S. Joseph, N. R. Aluru, and E. Jakobsson. Anomalously immobilized water: A new water phase induced by confinement in nanotubes. *Nano Letters*, 3:589–592, 2003.

[165] H. Tanaka and K. Koga. *Water in confining geometries.* Berlin ; New York, Springer, 2003. Editor: Victoria Buch and J. Paul Devlin, series Title: Water in confining geometries. pages: 151-177.

[166] M. C. Bellissent-Funel. Status of experiments probing the dynamics of water in confinement. *European Physical Journal E*, 12:83–92, 2003.

[167] Y. Maniwa, H. Kataura, M. Abe, S. Suzuki, Y. Achiba, H. Kira, and K. Matsuda. Phase transition in confined water inside carbon nanotubes. *Journal of the Physical Society of Japan*, 71:2863–2866, 2002.

[168] Y. Maniwa, H. Kataura, M. Abe, A. Udaka, S. Suzuki, Y. Achiba, H. Kira, K. Matsuda, H. Kadowaki, and Y. Okabe. Ordered water inside carbon nanotubes: formation of pentagonal to octagonal ice-nanotubes. *Chemical Physics Letters*, 401:534–538, 2005.

[169] M. C. Gordillo and J. Martí. Hydrogen bond structure of liquid water confined in nanotubes. *Chemical Physics Letters*, 329:341–345, 2000.

[170] J. Wang, Y. Zhu, J. Zhou, and X. H. Lu. Diameter and helicity effects on static properties of water molecules confined in carbon nanotubes. *Physical Chemistry Chemical Physics*, 6:829–835, 2004.

[171] J. Martí and M. C. Gordillo. Microscopic dynamics of confined supercritical water. *Chemical Physics Letters*, 354:227–232, 2002.

[172] M. C. Gordillo and J. Martí. Hydrogen bonding in supercritical water confined in carbon nanotubes. *Chemical Physics Letters*, 341:250–254, 2001.

[173] J. Martí and M. C. Gordillo. Effects of confinement on the vibrational spectra of liquid water adsorbed in carbon nanotubes. *Physical Review B*, 63:165430, 2001.

[174] D. J. Mann and M. D. Halls. Water alignment and proton conduction inside carbon nanotubes. *Physical Review Letters*, 90:195503, 2003.

[175] C. Dellago, M. M. Naor, and G. Hummer. Proton transport through water-filled carbon nanotubes. *Physical Review Letters*, 91:105902, 2003.

[176] N. E. Levinger. Water in confinement. *Science*, 298:1722–1723, 2002.

[177] Hiroharu Yui, Yanli Guo, Kana Koyama, Tsuguo Sawada, George John, Bo Yang, Mitsutoshi Masuda, and Toshimi Shimizu. Local environment and property of water inside the hollow cylinder of a lipid nanotube. *Langmuir*, 21:721–727, 2005.

[178] G. C. Pimentel and A. L. McClellan. *The Hydrogen Bond.* San Francisco, 1960. ed: W. H. Freeman vol p 475 p.

[179] C. J. Gruenloh, J. R. Carney, C. A. Arrington, T. S. Zwier, S. Y. Fredericks, and K. D. Jordan. Infrared spectrum of a molecular ice cube: The S-4 and D-2d water octamers in benzene-(water)(8). *Science*, 276:1678–1681, 1997.

[180] R. N. Pribble and T. S. Zwier. Probing hydrogen-bonding in benzene-(water)(n) clusters using resonant ion-dip ir spectroscopy. *Faraday Discussions*, 97:229–241, 1994.

[181] R. N. Pribble and T. S. Zwier. Size-specific infrared-spectra of benzene-(H_2O)(n) clusters (n=1 through 7) - evidence for noncyclic (H_2O)(n) structures. *Science*, 265:75–79, 1994.

[182] P. Andersson, C. Steinbach, and U. Buck. Vibrational spectroscopy of large water clusters of known size. *European Physical Journal D*, 24:53–56, 2003.

[183] J. P. Devlin and V. Buch. Surface of ice as viewed from combined spectroscopic and computer modeling studies. *J. Phys. Chem.*, 99:16534–16548, 1995.

[184] B. Rowland, N. S. Kadagathur, J. P. Devlin, V. Buch, T. Feldman, and M. J. Wojcik. Infrared-spectra of ice surfaces and assignment of surface-localized modes from simulated spectra of cubic ice. *Journal of Chemical Physics*, 102:8328–8341, 1995.

[185] J. P. Devlin and V. Buch. Vibrational spectroscopy and modeling of the surface and subsurface of ice and of ice-adsorbate interactions. *Journal of Physical Chemistry B*, 101:6095–6098, 1997.

[186] C. Tsai and K. D. Jordan. Theoretical-study of small water clusters - low-energy fused cubic structures for (H_2O)n, n=8, 12, 16, and 20. *Journal of Physical Chemistry*, 97:5208–5210, 1993.

[187] H. M. Lee, S. B. Suh, and K. S. Kim. Structures, energies, and vibrational spectra of water undecamer and dodecamer: An *ab initio* study. *Journal of Chemical Physics*, 114:10749–10756, 2001.

[188] G. S. Fanourgakis, E. Apra, W. A. de Jong, and S. S. Xantheas. High-level *ab initio* calculations for the four low-lying families of minima of(H_2O)(20). ii. spectroscopic

signatures of the dodecahedron, fused cubes, face-sharing pentagonal prisms, and edge-sharing pentagonal prisms hydrogen bonding networks. *Journal of Chemical Physics*, 122:134304, 2005.

[189] A. Lagutschenkov, G. S. Fanourgakis, G. Niedner-Schatteburg, and S. S. Xantheas. The spectroscopic signature of the “all-surface” to “internally solvated” structural transition in water clusters in the n=17-21 size regime. *Journal of Chemical Physics*, 122:194310, 2005.

[190] O. Byl, P. Kondratyuk, and J. T. Yates Jr. Adsorption and dimerization of no inside single-walled carbon nanotubes - an infrared spectroscopic study. *J. Phys. Chem. B*, 107:4277–4279, 2003.

[191] W. L. Yim, O. Byl, J. T. Yates Jr., and J. K. Johnson. Dimensional effects on the lo-to splitting in cf4: First-principles and infrared absorption studies. *Journal of the American Chemical Society*, 127:3198–3206, 2005.

[192] K. Koga, R. D. Parra, H. Tanaka, and X. C. Zeng. Ice nanotube: What does the unit cell look like? *Journal of Chemical Physics 2000*, 113:5037–5040, 2000.

[193] K. Koga, G. T. Gao, H. Tanaka, and X. C. Zeng. How does water freeze inside carbon nanotubes? *Physica a-Statistical Mechanics and Its Applications*, 314:462–469, 2002.

[194] J. Bai, C. R. Su, R. D. Parra, X. C. Zeng, H. Tanaka, K. Koga, and J. M. Li. *Ab initio* studies of quasi-one-dimensional pentagon and hexagon ice nanotubes. *Journal of Chemical Physics*, 118:3913–3916, 2003.

[195] S. Ghosh, K. V. Ramanathan, and A. K. Sood. Water at nanoscale confined in single-walled carbon nanotubes studied by nmr. *Europhysics Letters*, 65:678–684, 2004.

[196] W. L. Yim, O. Byl, J. T. Yates Jr., and J. K. Johnson. Vibrational behavior of adsorbed co2 on single-walled carbon nanotubes. *Journal of Chemical Physics*, 120:5377–5386, 2004.

[197] P. Basu, T. H. Ballinger, and J. T. Yates Jr. Wide temperature range ir spectroscopy cell for studies of adsorption and desorption on high area solids. *Review of Scientific Instruments*, 59:1988, 1321-1327.

[198] D. B. Mawhinney, V. Naumenko, A. Kuznetsova, J. T. Yates, Jr., J. Liu, and R. E. Smalley. Infrared spectral evidence for the etching of carbon nanotubes: Ozone oxidation at 298 K. *J. Am. Chem. Soc.*, 122:2383–2384, 2000.

[199] H. J. C. Berendsen, J. R. Grigera, and T. P. Straatsma. The missing term in effective pair potentials. *J. Phys. Chem.*, 91:6269–6271, 1987.

[200] Matej Praprotnik, Dusanka Janezic, and Janez Mavri. Temperature dependence of water vibrational spectrum: A molecular dynamics simulation study. *Journal of Physical Chemistry A*, 108:11056–11062, 2004.

[201] Kahled Toukan and Aneesur Rahman. Molecular-dynamics study of atomic motions in water. *Physical Review B*, 31:2643–2648, 1985.

[202] J. Martí and M. C. Gordillo. Temperature effects on the static and dynamic properties of liquid water inside nanotubes. *Physical Review E*, 64:021504, 2001.

[203] D. Frenkel and B. Smit. *Understanding Molecular Simulation: from algorithms to applications. 2nd ed.* Academic Press, San Diego, 2002.

[204] H. J. C. Berendsen, J. P. M. Postma, W. F. van Gunsteren, A. DiNola, and J. R. Haak. Molecular dynamics with coupling to an external bath. *Journal of Chemical Physis*, 81:3684–3690, 1984.

[205] J. Martí, E. Guàrdia, and J. A. Padró. *J. Chem. Phys.*, 101:10883, 1994.

[206] G. Kresse and J. Furthmueller. Efficient iterative schemes for *ab initio* total-energy calculations using a plane-wave basis set. *Phys. Rev. B*, 54:11169–11186, 1996.

[207] G. Kresse and J. Furthmueller. Vasp menu. *Compu. Mat. Sci.*, 6:15, 1996.

[208] G. Kresse and J. Hafner. *Ab initio* molecular dynamics for liquid metals. *Phys. Rev. B*, 47:558–561, 1993.

[209] G. Kresse and J. Hafner. *Ab initio* molecular-dynamics simulation of the liquid-metal-amorphous-semiconductor transition in germanium. *Phys. Rev. B*, 49:14251–14269, 1994.

[210] J. P. Perdew, K. Burke, and M. Ernzerhof. *Phys. Rev. Lett.*, 77:3865, 1996.

[211] H. J. Monkhorst and J. D. Pack. *Phys. Rev. B*, 13:5188, 1976.

[212] S. Baroni, A. D. Corso, S. D. Gironcoli, and P. Giannozzi. http://www.pwscf.org.

[213] J. R. Scherer. *The vibrational spectroscopy of water. In Advances in Infrared and Raman Spectroscopy.* Heyden: London, New York, 1975. ed: R. J. H. Clark and R. E. Hester vol.5. page 149-216.

[214] K. Nauta and R. E. Miller. Formation of cyclic water hexamer in liquid helium: The smallest piece of ice. *Science*, 287:293–295, 2000.

[215] J. Hernandez, N. Uras, and J. P. Devlin. Molecular bending mode frequencies of the surface and interior of crystalline ice. *Journal of Chemical Physics*, 108:4525–4529, 1998.

[216] A. Striolo, A. A. Chialvo, K. E. Gubbins, and P. T. Cummings. Water in carbon nanotubes: Adsorption isotherms and thermodynamic properties from molecular simulation. *J. Chem. Phys.*, 122:234712, 2005.